Design of yaw rate controller for electric vehicle

Kolarić, Filip

Master's thesis / Diplomski rad

2023

Degree Grantor / Ustanova koja je dodijelila akademski / stručni stupanj: **University of Zagreb, Faculty of Mechanical Engineering and Naval Architecture / Sveučilište u Zagrebu, Fakultet strojarstva i brodogradnje**

Permanent link / Trajna poveznica: https://urn.nsk.hr/urn:nbn:hr:235:350350

Rights / Prava: In copyright/Zaštićeno autorskim pravom.

Download date / Datum preuzimanja: **2025-01-28**

UNIVERSITY OF ZAGREB
FACULTY OF MECHANICAL ENGINEERING AND NAVAL
ARCHITECTURE

MASTER'S THESIS

Filip Kolarić

Zagreb, 2023

UNIVERSITY OF ZAGREB
FACULTY OF MECHANICAL ENGINEERING AND NAVAL
ARCHITECTURE

MASTER'S THESIS

Mentor: Student:

Asst. Prof. Mario Hrgetić   Filip Kolarić

Zagreb, 2023

IZJAVA

Ja, Filip Kolarić, izjavljujem da sam ovaj rad izradio samostalno koristeći znanja i vještine stečene tijekom studija i koristeći navedenu stručnu literaturu.

STATEMENT

I, Filip Kolarić, declare that this thesis has been generated by me as a result of knowledge and skills gained during my university studies and using the specified scientific literature.

_____

Filip Kolarić

SVEUČILIŠTE U ZAGREBU
FAKULTET STROJARSTVA I BRODOGRADNJE
Središnje povjerenstvo za završne i diplomske ispite
Povjerenstvo za diplomske radove studija strojarstva za smjerove:
proizvodno inženjerstvo, računalno inženjerstvo, industrijsko inženjerstvo i menadžment,
inženjerstvo materijala te mehatronika i robotika

Sveučilište u Zagrebu Fakultet strojarstva i brodogradnje	
Datum:	Prilog:
Klasa: 602 – 04 / 23 – 6 / 1	
Ur. broj: 15 - 1703 - 23 -	

DIPLOMSKI ZADATAK

Student: **FILIP KOLARIĆ**   Mat. br.: 0035215468

Naslov rada na hrvatskom jeziku: **Projektiranje sustava upravljanja brzinom skretanja električnog vozila**

Naslov rada na engleskom jeziku: **Design of yaw rate controller for electric vehicle**

Opis zadatka:

Modern electric vehicles are equipped with a number of active vehicle dynamics control systems with the aim of increasing driving safety and comfort. The control of the yaw rate of electric vehicles with multiple electric motors and the development of optimal control strategies for different configurations of actuators have been the subject of intensive research in the last ten years. In the thesis it is necessary:

• to describe vehicle dynamics models and different configurations of actuators utilized by advanced active lateral dynamics control systems of electric vehicles
• to design a system for generating the optimal yaw rate reference for different driving scenarios and driving trajectory configurations
• to develop the electric vehicle yaw rate control system and carry out the controller tuning
• to design and test the torque allocation algorithm for individual actuators
• analyze the performance of the yaw rate control for different driving scenarios by using software tools for vehicle dynamics simulations (e.g. Matlab Simulink and AVL VSM).

In the work, it is necessary to indicate the literature used and any help received.
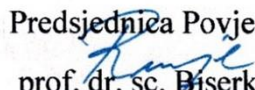
Zadatak zadan: Rok predaje rada: Predviđeni datum obrane:
17. studenog 2022.   19. siječnja 2023.   23. siječnja do 27. siječnja 2023.

Zadatak zadao: Predsjednica Povjerenstva:
doc. dr. sc. Mario Hrgetić   prof. dr. sc. Biserka Runje

CONTENT

LIST OF FIGURES

LIST OF TABLES

LIST OF SYMBOLS

Symbol	Unit	Description
$a_{y,max}$	m/s^2	Maximum lateral acceleration for the desired cornering response
A_0	N	Static driving resistance
A_{aero}	m^2	Vehicle projected frontal area
a_x	m/s^2	Longitudinal acceleration
a_y	m/s^2	Lateral acceleration
a_y^*	m/s^2	Lateral acceleration limit for the linear region of desired cornering response
B_0	N/(m/s)	Linear driving resistance
B_N	-	Daisy-chain allocation control vector/matrix
$C_{\delta_{w,ij}}$	-	Cosine function of the wheel angle
C_0	N/(m/s)^2	Quadratic driving resistance
C_d	-	Aerodynamic drag coefficient
C_i	-	Front and rear tire cornering stiffnesses
C_{li}	-	Front and rear aerodynamic lift coefficient
D	Nm (s^2/rad)^3	Derivative gain of PD^3 controller
e_{ω_z}	rad/s	Yaw rate error
$e_{\omega_z}^*$	rad/s	Scaled yaw rate error
$F_{x,drag}$	N	Longitudinal aerodynamic drag force
F_{x_0}	N	Longitudinal tire force (pure slip)
F_{y_0}	N	Lateral tire force (pure slip)
$F_{z,downforce}$	N	Aerodynamic downforce contribution to the vertical tire force
$F_{z,dyn}$	N	Dynamic contribution to the vertical tire force
$F_{z,ij}$	N	Vertical tire force
$F_{z,stat}$	N	Static vertical tire force
F_{res}	N	Coupled longitudinal resistive forces
F_x	N	Longitudinal tire force (combined slip)
F_{xx}	N	Total longitudinal tire force
F_y	N	Lateral tire force (combined slip)
F_{yy}	N	Total lateral tire force
g	m/s^2	Gravity constant ($g = 9{,}81$ m/s^2)
h_{CoG}	m	Height of the centre of gravity
h_{CoP}	m	Height of the centre of pressure
i	-	Subscript indicating vehicle axle ($i = F$ front, $i = R$ rear)
i_i	-	Front and rear axle gearbox gear ratio
I_{zz}	kgm^2	Moment of inertia about the vertical axis
j	-	Subscript indicating vehicle side ($j = L$ left, $j = R$ right)

K	-	Understeer gradient
l	m	Vehicle wheelbase
l_i	m	Distance from the front and rear axle to the CoG
m	kg	Total vehicle mass
$M_{z,des}$	Nm	Desired/reference yaw moment
$M_{z,diff}$	Nm	Difference between the current and previous stage upper/lower limits for positive/negative allocation stages
$M_{z,max}$	Nm	Maximum yaw moment produced by the maximum wheel torques
$M_{z,max-2RWD}$	Nm	Maximum yaw moment produced by the maximum wheel torques for a 2WD vehicle
$M_{z,max-pos,ij}$	Nm	Maximum yaw moment (potential) produced by the maximum positive wheel torque
$M_{z,max-reg,ij}$	Nm	Maximum yaw moment (potential) produced by the maximum negative wheel torque
$M_{z,t-front}$	Nm	Maximum yaw moment produced by the maximum wheel torques around the front track
$M_{z,t-rear}$	Nm	Maximum yaw moment produced by the maximum wheel torques around the rear track
$M_{z,wb-front}$	Nm	Maximum yaw moment produced by the maximum wheel torques around the front wheelbase
P	Nm $(s/rad)^3$	Proportional gain of PD^3 controller
p_X	m	Vehicle X position in respect to the global track reference frame
p_Y	m	Vehicle Y position in respect to the global track reference frame
R	m	Curve radius
R_e	m	Effective tire radius
s	m	Spatial coordinate
$S_{\delta_{w,ij}}$	-	Sine function of the wheel angle
$T_{m,TN}$	Nm	Maximum positive motor torque (electric motor curve)
$T_{m,TN-reg}$	Nm	Maximum negative motor torque (electric motor curve)
$T_{w,des,ij}$	Nm	Desired
$T_{w,lim-reg}$	Nm	Negative wheel torque limit
$T_{w,max,ij}$	Nm	Maximum positive wheel torque
$T_{w,max-fric}$	Nm	Maximum wheel friction torque
$T_{w,TN}$	Nm	Maximum positive wheel torque (electric motor curve)
$T_{w,TN-reg}$	Nm	Maximum negative wheel torque (electric motor curve)
u_N	Nm	Daisy-chain allocation actuator input ($= T_{w,des}$)
V	m/s	Vehicle speed
v	Nm	Daisy-chain allocation virtual input ($= M_{z,des}$)
$v_{x,ij}$	m/s	Wheel longitudinal speed
$v_{y,ij}$	m/s	Wheel lateral speed
v_x	m/s	Vehicle longitudinal speed

v_y	m/s	Vehicle lateral speed
w_i	m	Front and rear wheel track widths
α	-	Daisy-chain tuning parameter (conventional)
$\alpha_{i,const-neg}$	-	Negative constant daisy-chain tuning parameter
$\alpha_{i,const-pos}$	-	Positive constant daisy-chain tuning parameter
$\alpha_{i,LUT-neg}$	-	Negative daisy-chain tuning parameter from a LUT
$\alpha_{i,LUT-pos}$	-	Positive daisy-chain tuning parameter from a LUT
α_{i-neg}	-	Negative daisy-chain tuning parameter
α_{i-pos}	-	Positive daisy-chain tuning parameter
α_{ij}	rad	Tire slip angle
β	rad	Vehicle sideslip angle
β_{ij}	rad	Wheel sideslip angle
$\delta_{w,ij}$	rad	Wheel steer angle
δ_{din}	rad	Dynamic steering wheel angle
δ_{swa}	rad	Steering wheel angle
η_i	rad/(m/s^2)	Front and rear cornering coefficients
$\lambda_{i,const}$	-	Wheel friction torque scaling factor
$\lambda_{i,const-reg}$	-	Constant negative motor torque scaling factor
$\lambda_{i,reg}$	-	Negative motor torque scaling factor
λ_{i-neg}	-	Negative yaw moment potential ratio factor
λ_{i-pos}	-	Positive yaw moment potential ratio factor
λ_{err}	-	Yaw rate error scaling factor
λ_{ij}	-	Wheel torque distribution ratio for the last daisy-chain allocation stage
λ_{yaw}	rad/s	Yaw reference correction factor
μ	-	Tire-road friction coefficient
μ	-	Tire-road friction coefficient
ρ_{air}	kg/m^3	Air density ($\rho_{air} = 1{,}2$ kg/m^3)
$\sigma_{x,ij}$	-	Longitudinal tire slip ratio
$\sigma_{y,ij}$	-	Lateral tire slip ratio
σ_{ij}	-	Combined tire slip ratio
ψ	rad	Vehicle yaw angle
$\omega_{z,ref}$	rad/s	Reference yaw rate
ω_{ij}	rad/s	Wheel angular speed
ω_z	rad/s	Vehicle yaw rate
ω_δ	rad/s	Steering wheel angular speed

LIST OF ABBREVIATIONS

Abbreviation	Description
BEV	Battery electric vehicle
BL	Baseline
CoG	Centre of gravity
CoP	Centre of pressure
CRC	Constant radius cornering
DNF	Did not finish
DOF	Degree of freedom
DYC	Direct Yaw Moment Control
EV	Electric vehicle
IWM	In-wheel motor
LPV	Linear Parameter-Varying
LQG	Linear Quadratic Gaussian
LQR	Linear Quadratic Regulator
LUT	Lookup table
MF	Magic Formula
MPC	Model Predictive Control
NMPC	Nonlinear Model Predictive Control
ODE	Ordinary Differential Equations
PD^3	Cubic-error Proportional-Derivative
PID	Proportional-Integral-Derivative
SISO	Single-input-single-output
SL	Straight line
SMC	Sliding Mode Control
SS	Steady-state
TCS	Traction Control System
TV	Torque Vectoring

SAŽETAK

Moderna električna vozila obično su opremljena s više od jednog elektromotora. Mogućnost ugradnje i korištenja više od jednog elektromotora unosi još jedan stupanj slobode u pogledu upravljanja vozilom. Ova pojava većeg broja upravljačkih jedinica nego što ima stanja kojima treba upravljati (*over-actuation*), pruža znatne mogućnosti aktivnom upravljanju dinamike skretanja, ponajprije vektoriranju momenata – raspodjeli okretnog momenta kotača između više kotača. U posljednjih deset godina, upravljanje brzine skretanja električnih vozila s više elektromotora i razvoj optimalnih strategija upravljanja predmet su intenzivnih istraživanja s ciljem poboljšanja sigurnosti, performansi i cjelokupnog iskustva vožnje. Glavni cilj ovog diplomskog rada je predložiti i komentirati performanse jednog takvog sustava za upravljanje brzine skretanja. Prvo su pregledani trenutni najsuvremeniji generatori referentne brzine skretanja i predložena je metoda za generiranje referentne brzine skretanja uz pomoć AVL VSM™ koji je korišten za analizu stacionarnog i tranzijentnog ponašanja vozila. Zastim je predložen i vremenski optimalan referentni generator brzine skretanja također kao osnova za budući rad. Ovaj pristup koristi kinematički model vozila s nelinearnim modelom gume koji se koristi u ovom radu. Pregledom literature uspoređeno je nekoliko regulatora momenta skretanja, te je PD^3 regulator odabran kao obećavajuća i robusna opcija. Predložena *daisy-chain* raspodjela momenta je detaljno razrađena uz objašnjenje razloga odabira takvog dizajna. Sustav upravljanja brzine skretanja modeliran je u MathWorks MATLAB/Simulink® i izvodi se u ko-simulaciji s AVL VSM™. Naposlijetku se sustav upravljanja brzine skretanja analizira na nekoliko testnih manevara.

Ključne riječi: električno vozilo, *over-actuation*, upravljanje brzinom skretanja, generator reference, PD^3 regulator momenta skretanja, *daisy-chain* raspodjela momenata

SUMMARY

Modern electric vehicles are typically equipped with more than one electric motor. The ability to install and use more than one electric motor introduces another degree of freedom in terms of vehicle handling. This over-actuation offers substantial opportunities for active yaw dynamics control, most notably torque vectoring – the distribution of wheel torques between multiple wheels. In the last ten years, the yaw rate control of electric vehicles with multiple electric motors and the development of optimal control strategies have been subject to intensive research with the goal of improving safety, performance, and overall driving experience. The main goal of this thesis is to propose and evaluate the performance of one such yaw rate control system. First, current state-of-the-art yaw rate reference generators are overviewed, and a method is proposed to generate yaw rate reference using AVL VSM™ to analyse the steady-state and transient behaviour of the vehicle. An alternative, time-optimal yaw reference generator is also proposed, as a basis for future work. The second approach uses the kinematic vehicle model with a non-linear tire model that is used throughout this work. Based on a detailed literature review, a few yaw moment controllers are compared, and a PD^3 controller is chosen as a promising and robust option. The proposed Daisy-chain torque allocation is worked out in detail, explaining the reasons for the application of such a design. The yaw rate control system is modelled in MathWorks MATLAB/Simulink$^®$ and run in co-simulation with AVL VSM™. Finally, the yaw rate control system is evaluated on several test manoeuvres.

Key words: electric vehicle, over-actuation, yaw rate control, reference generator, PD^3 yaw moment controller, daisy-chain torque allocation

PROŠIRENI SAŽETAK

Mnoga moderna električna vozila posjeduju više od jednog električnog motora. Posljedica toga je više stupnjeva slobode koji se mogu koristiti u aktivnim sustavima upravljanja dinamikom vozila. Jedan od ovakvih sustava je i sustav upravljanja brzinom skretanja vozila, poznat i kao sustav vektoriranja momentima (engl. *Torque vectoring*)

Cilj ovog diplomskog rada jest projektirati jedan ovakav sustav, modelirati ga, te provesti simulacijsku analizu unutar ko-simulacijskog okruženja AVL VSM™ – alata za simuliranje uzdužne i bočne dinamike vozila i programskog paketa MathWorks MATLAB/Simulink®.

Ovaj rad je organiziran u šest poglavlja, čiji je sadržaj sažet kako slijedi.

Poglavlje 1 – 'Uvod' – U uvodu je objašnjena motivacija koja stoji iza korištenja sustava upravljanja brzinom skretanja. Također su spomenute i različite strategije upravljanja brzinom skretanja.

Poglavlje 2 – 'Generator reference brzine skretanja' – Na početku ovoga poglavlja dana su dva primjera iz literature za generiranje reference brzine skretanja, gdje se jedan temelji na empirijskim zapažanjima ponašanja vozila, a drugi na upotrebi linearnog dinamičkog modela vozila za formiranje vremenski optimalne reference brzine skretanja. Upotrebom alata AVL VSM™ i analizom rezultata stacionarnog i tranzijentnog ponašanja vozila uz pomoć MathWorks MATLAB® programskog paketa, generirana je prirodna referenca brzine skretanja karakteristična za vozilo korišteno za analizu. Stacionarno ponašanje vozila analizirano je izvođenjem *ramp steer* manevra na više stacionarnih brzina vozila, dok se tranzijentno ponašanje analizira držanjem stacionarnog zakreta upravljača na više stacionarnih uzdužnih akceleracija. Prirodna referenca modificirana je kako bi povećala ostvarive bočne akceleracije. Na kraju poglavlja ugrubo je predstavljena struktura modela koji bi se mogao koristiti za generiranje vremenski optimalne reference slične onima korištenim u primjerima iz literature opisanim na početku poglavlja.

Poglavlje 3 – 'Regulator momenta skretanja' – U ovom poglavlju je prvo dan kratki pregled dosad već korištenih regulatora momenta skretanja. Uz pomoć informacija iz literature donesena je odluka o korištenju propocionalno-derivativnog regulatora s kubnom greškom PD^3. Predstavljeni su razlozi odabira i prednosti PD^3 regulatora u primjeni regulacije momenta skretanja. Također je objašnjen i razlog izostanka integralnog člana te je predstavljen primjer alternativnog regulatora koji bi uključivao i integralni član kao mogući smjer budućeg rada.

Poglavlje 4 – 'Raspodjela momenata' – U ovom poglavlju objašnjen je način raspodjele momenata na kotače primjenom *daisy-chain* metode kako bi se ostvario željeni, referentni moment skretanja dobiven iz regulatora momenta skretanja. Prije dodjeljivanja pozitivnih ili negativnih momenata kotačima, provjeravaju se raspoloživi potencijali svakoga kotača, na temelju raspoloživog momenta trenja na gumama, uz vrijednost koeficijenta prijanja 1, i maksimalnog momenta dobivenog iz mape motora te se na temelju toga odlučuje koliko momenta će se kojemu kotaču dodijeliti.

Poglavlje 5 – 'Ispitni manevri i rezultati simulacija' – U ovom poglavlju su opisani scenariji vožnje kojima će se ispitati rad sustava upravljanja brzinom skretanja predstavljenog u prijašnjim poglavljima. Rezultati i performanse dobivene simulacijom sustava upravljanja ispitane su po više kriterija uspoređujući upravljano vozila s vozilom bez sustava upravljanja.

Poglavlje 6 – 'Zaključak' – Unutar zaključka navedeni su glavni rezultati rada, istaknute su dobivene performanse dinamike vozila uz predloženi koncept regulatora i opisane mogućnosti nadogradnje i poboljšanja u razvoju predloženog sustava upravljanja dinamikom skretanja električnog vozila.

1. INTRODUCTION

This thesis is done in cooperation with the AVL-AST d.o.o. from Zagreb and AVL List GmbH from Graz with the purpose of developing a yaw rate control system for electric vehicles that consists of reference generator, yaw moment controller and torque allocation algorithm.

1.1. Motivation

Active yaw control systems for improved performance and safety have been commonplace in passenger vehicles for the past two decades, especially in electric vehicles (EVs). Modern all-wheel-drive EVs offer substantial opportunities for active control of yaw dynamics by over-actuation, namely torque vectoring (TV) – the distribution of wheel torques between multiple wheels. TV extends the maximum cornering force by the superior distribution of yaw moment, making better use of available friction. The ability to install an electric motor in every single wheel introduces another degree of freedom in terms of vehicle handling. Apart from this, the short response time of the electric motors provides a more effective transmission of the motor torque to the wheel.

In the last ten years, the yaw rate control of electric vehicles with multiple electric motors and the development of optimal control strategies have been subject to intensive research with the goal of improving safety, performance and overall driving experience. Many contributions have been proposed to the employment of different direct yaw moment control (DYC) methods, given the increased number of electric vehicles and torque distribution freedom of electric powertrains with independent motors. Also, in some cases, due to the advancements made in electronic differentials. Control methods such as PID (Proportional Integral Derivative), LPV (Linear Parameter-Varying), LQR (Linear Quadratic Regulator), LQG (Linear Quadratic Gaussian), H-infinity, Fuzzy Logic, SMC (Sliding Mode Control), and MPC (Model Predictive Control) have been investigated in recent years, some of them with a combination of feedforward techniques. Typical control variables in such controllers are yaw rate and sideslip angle. TV system (Figure 1) typically follows a yaw reference using a controller and subsequent control allocation for torque distribution between individual wheels. The sideslip angle controller is coupled with the yaw rate controller inside the yaw moment controller and generally acts as a safety measure.
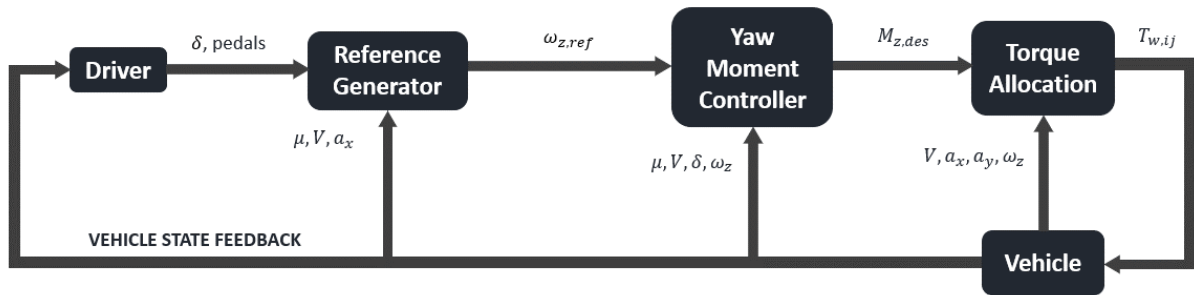
Figure 1. An example of a torque vectoring controller schematic

In more recent years, especially because autonomous system trend, a significant amount of research was done on the yaw rate reference generator, as it is the basis of the TV system. These yaw rate references are trying to alter the vehicle's behaviour, from the safety standpoint and the point of vehicle handling. Modern vehicles, especially high-performance, have different driving modes that represent different handling characteristics of the vehicle. These handling characteristics are usually analysed by comparing the understeer gradients of the vehicle that denotes if the vehicle is in neutral steer, understeer or oversteer, as shown in Figure 2, based on vehicle states like vehicle speed, yaw velocity/rate gain, steering wheel angle and lateral acceleration.
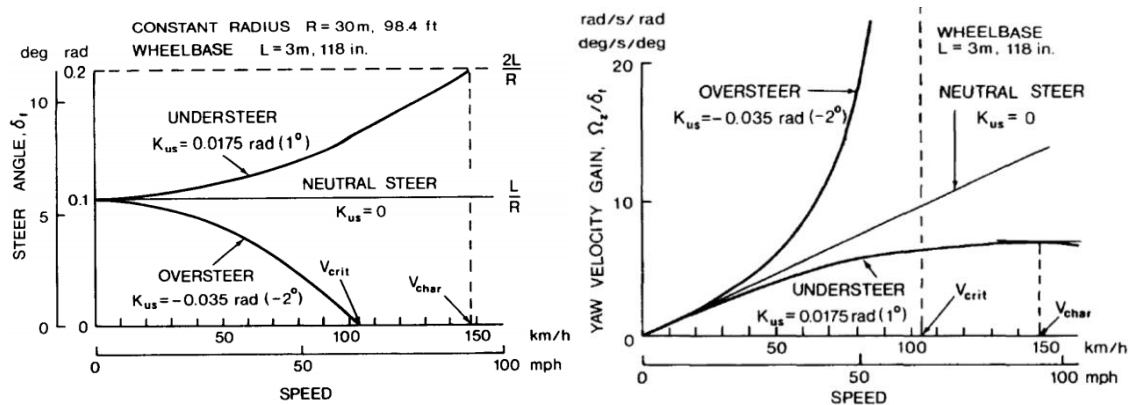
Figure 2. Relationship between steering angle (left) and speed, and yaw velocity gain (right) and speed − neutral steer, understeer and oversteer vehicles [1]

The vehicle handling behaviour can be altered in various ways, and one such approach that aims to increase the maximum lateral acceleration of a baseline vehicle is presented in this thesis.

1.2. Drivetrain and Demonstrator Vehicle Information

All the analysis carried out in this thesis is done on a single demonstrator vehicle. The demonstrator vehicle model parameters, such as vehicle geometry (e.g. wheel tracks and base lengths, CoG height, weight and its static distribution, etc.) and tire model parameters, used in this thesis are taken from a validated full-size BEV vehicle. These parameters are used for simulation, and the definition of the kinematic two-track vehicle model used throughout the

thesis. The default drivetrain configuration is changed to present the capabilities of a four-wheel-drive, over-actuated electric vehicle. For simplicity, the drivetrain configuration is chosen to have electric in-wheel motors (IWMs) with a single-speed gearbox (Figure 3). This configuration offers the needed flexibility and is a logical start for yaw motion control algorithms while avoiding the need to model eventual delays in the system (e.g. due to gear backlash or/and shaft elasticity). Even though it's still present in this configuration, it's negligible and thus ignored. Everything presented in the following chapters can later be extended to "less flexible" configurations (1+1, 1+2, etc., and either the in-wheel or conventionally chassis-mounted electric motors). Front-to-rear static weight distribution is approximately 50:50, and all wheels have the same tire radius.
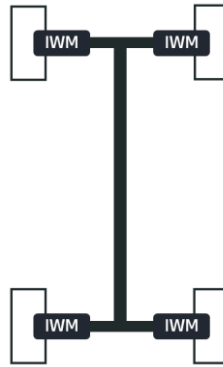
Figure 3.   Drivetrain configuration

The vehicle has Ackermann steering kinematics [2]. Because of it, wheel angle values of the inner and the outer wheel are different, as illustrated in Figure 4; thus, the following is true:

$$\delta_w = \begin{cases} \delta_{w,FL} = f(\delta_{swa}) \\ \delta_{w,FR} = f(\delta_{swa}) \end{cases}. \tag{1}$$
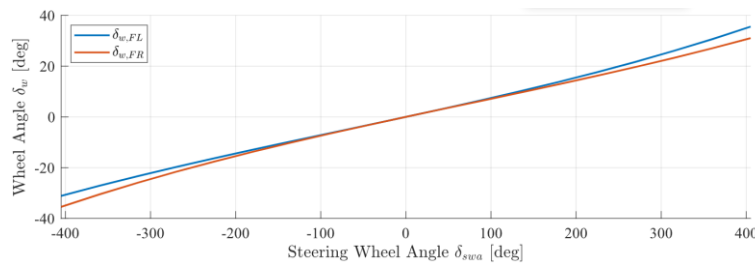
Figure 4.   Steering map – Ackermann geometry

The steering characteristic shown in Figure 4 was measured on an actual demonstrator vehicle and saved in the form of LUT. Throughout the thesis indexes i and j are used, i denoting the front (F) and rear (R) wheel, and j denoting the left (L) and right (R) wheel; thus, index $ij = [FL, FR, RL, RR]$.

2. YAW REFERENCE GENERATOR

In most cases, yaw references (e.g. [3] and [4]) are derived from the steady-state single-track vehicle models with a linear tire model and choosing an appropriate understeer gradient K, modifying the handling for stability or agility. In reality, lateral handling characteristics most clearly shown on $\delta - a_y$ (steering angle – lateral acceleration) plot exhibit a highly non-linear behaviour due to tire and vehicle dynamics model nonlinearities. Few papers (e.g. [5], [6] and [7]) implemented a reference derived from a piecewise expression for lateral acceleration given by Eq. (2).

$$\omega_{z,ref} = \frac{a_y}{V}, \quad a_y = \begin{cases} \dfrac{\delta_{dyn}}{K}, & \delta_{dyn} < a_y^* K \\ a_{y,max} + \left(a_y^* - a_{y,max}\right)e^{\frac{a_y^* K - \delta_{dyn}}{(a_y^* - a_{y,max})K}}, & \delta_{dyn} \geq a_y^* K \end{cases} . \tag{2}$$

The expression is inspired by empirical observation of vehicle behaviour. A linear relationship with dynamic steering wheel angle δ_{dyn} is specified for a given lateral acceleration threshold a_y^*. For lateral acceleration $a_y \geq a_y^*$, a non-linear exponent is implemented. The linear region is extended to higher lateral accelerations by changing the a_y^*. The maximum lateral acceleration is also increased up to the specified value $a_{y,max}$, which denotes the maximum achievable lateral acceleration and is a function of tire-road friction coefficient μ and longitudinal acceleration a_x. Using piecewise reference for lateral acceleration, realistic understeer characteristics may be designed. Typical (baseline) understeer characteristics and two potential characteristics are shown in Figure 5, and a yaw rate reference example produced by a piecewise reference is shown in Figure 6.
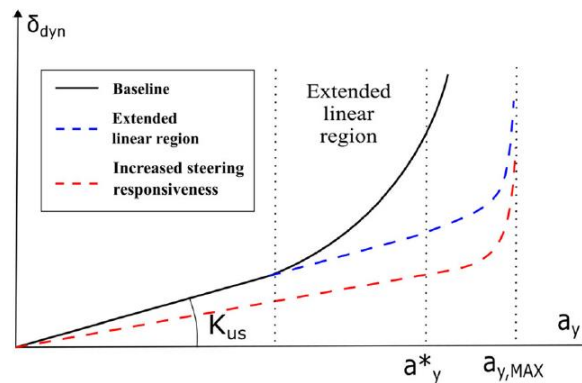
Figure 5. Visual representation of threshold and maximum lateral accelerations for potential understeering characteristics produced by a piecewise reference [7]
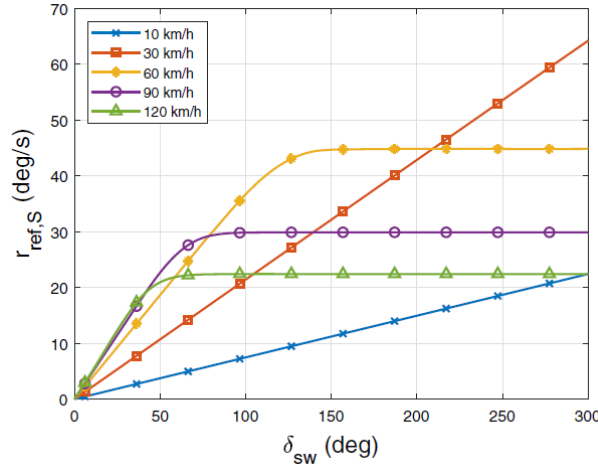
Figure 6.   Example of the reference yaw rate map at zero longitudinal acceleration [7]

Another interesting approach proposed in [8] uses a three DOF single-track model with a linear tire model and adds a direct yaw moment M_{zz} to emulate left-right TV for a four-wheel vehicle. This model is then used to determine the time-optimal yaw rate reference. Using a time-optimal control problem, an ideal driver is emulated, one that can drive the vehicle at its limits. The time-optimal reference was generated for an open-loop (uncontrolled) and a closed-loop (controlled) case. The optimisation results are shown in Figure 7.
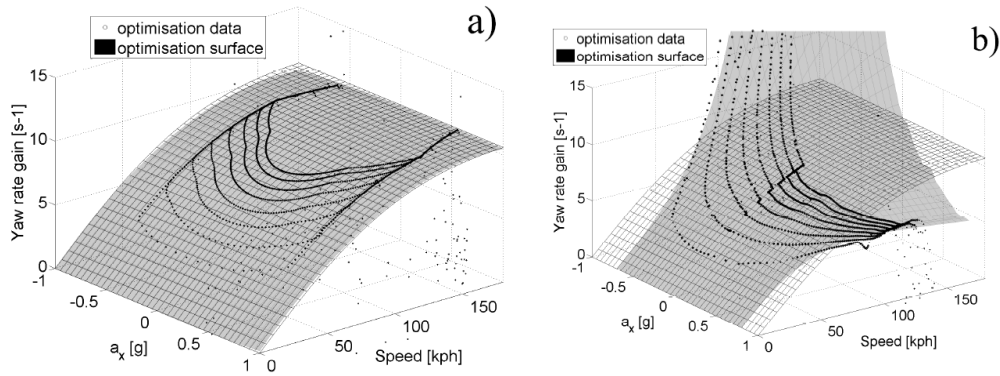
Figure 7.   Yaw rate gain surfaces of a controlled and uncontrolled vehicle [8]

Grey surfaces in Figure 7 represent the surface fit to the data obtained from the time-optimal control problem for a TV controlled (a) and an uncontrolled (b) vehicle. The white mesh surface in Figure 7 is the steady-state analytic result obtained from:

$$\frac{\omega_z}{\delta_{w,F}} = \frac{V}{l + K_{nat}^{SS} V^2},$$ (3)

where front wheel steering angle $\delta_{w,F}$ is equal to the average value of $\delta_{w,FL}$ and $\delta_{w,FR}$ obtained by Eq. (1). Natural steady-state understeer gradient K_{nat}^{SS} of the vehicle is defined as follows:

$$K_{nat}^{SS} = \left(\frac{1}{\eta_F} - \frac{1}{\eta_R}\right)\frac{1}{g}. \tag{4}$$

Eq. (4) is taken from [1] and [8] that define cornering coefficients η_F and η_R as a constant value calculated from the linear tyre model whose cornering stiffnesses C_F and C_R depend on vertical tire load F_z as follows:

$$C_{F/R} = \eta_{F/R} F_{z,F/R}. \tag{5}$$

Considering a single-track (bicycle) model [1] $F_{z,F/R}$ are calculated as follows:

$$F_{z,F} = \frac{m}{l}(gl_R - ha_x) \qquad\qquad F_{z,R} = \frac{m}{l}(gl_F + ha_x). \tag{6}$$

The first term in (6), for both vertical forces, corresponds to the vehicle static weight distribution, while the second one corresponds to the longitudinal weight transfer due to the longitudinal acceleration a_x of the vehicle. The conclusion that [8] came to was that the time-optimal yaw rate reference derived for a four-wheel independent TV matches with the analytical steady-state single-track expression for yaw rate gain (Eq. (3)). Considering Eq. (4)-(6), and that the vehicle used in this thesis has the same front and rear tyres and that the static weight distribution is approximately equal, K_{nat}^{SS} for the vehicle equals to zero; thus, yaw rate gain is proportional to the vehicle speed:

$$\frac{\omega_z}{\delta_{w,F}} = \frac{v}{l}. \tag{7}$$

Having in mind that a SS yaw rate $\omega_z = v/R$ and by rewriting equation (7) the following can be written:

$$\delta_{w,F} = \frac{l}{R}. \tag{8}$$

This means that the vehicle with $K_{nat}^{SS} = 0$ has a handling characteristic such that an increase in curve radius results in a decrease of a required wheel steer angle. Eq. (8) is characteristic for neutral steer as the wheel steer angle $\delta_{w,F}$ required to negotiate a given curve is independent of vehicle speed. This can be beneficial from the driver standpoint and what he can expect from the vehicle. For an increase or decrease of longitudinal acceleration corresponding to the acceleration and braking, driver just needs to maintain the same steering wheel angle, and the vehicle will behave as in a steady state with a constant vehicle speed, having the turning radius equal, as illustrated in Figure 8. Neutral steer is also characterised by

having equal front and rear tire slip ratios, meaning that an increase in one also leads to an increase in the other.
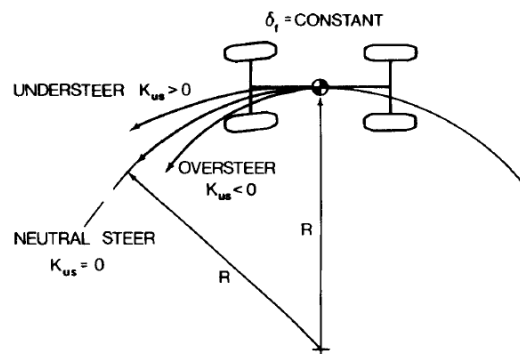
Figure 8. Curvature responses on neutral steer, understeer and oversteer vehicles at fixed steer angle [1]

Although the idea of having a neutral steer vehicle may seem interesting at first, one needs to evaluate the physical limits of the vehicle first, e.g. due to tire, electric motor or battery limits.

2.1.   Proposed Approach for Yaw Rate Reference Generation

To generate a yaw rate reference used in this thesis, the vehicle simulation tool AVL VSM™ was used. VSM uses a high-fidelity vehicle model to simulate longitudinal and lateral dynamic vehicle behaviour. To extract the appropriate data from the simulation results, MathWorks MATLAB® was used. Demonstrator vehicle and tire parameters are implemented in the VSM interface, and the baseline vehicle model is established. Two types of driver controller models are calibrated within the VSM – curvature and saturation-controlled driver. The curvature-controlled driver utilises a demand track curvature as an input and uses proportional and integral parameters for the steering and pedal/brake control. This driver is used for the yaw rate reference generation, while the saturation-controlled driver is used to evaluate the performance in the test manoeuvres in chapter 5, where it will be explained. The following SS and transient analysis are carried out for a constant tire-road friction coefficient $\mu = 1$ (dry road), but the same methodology can be applied for $\mu < 1$. Doing so would generate yaw rate references for other driving conditions.

2.1.1.   Steady-state Analysis

To evaluate the steady-state vehicle behaviour, ramp steer manoeuvre is constructed within the VSM. The ramp steer manoeuvre is conducted by linearly increasing the steering wheel angle, with a small gradient, at the constant vehicle speed; thus, $a_x = 0$. The test

generates useful information about the quasi-steady-state response of the vehicle. This information is used to extract the yaw reference but also to analyse the behaviour of the vehicle. Other useful information can also be pointed out, e.g. the transition between linear and non-linear regions of the vehicle and the maximum lateral acceleration that a car can withstand. A whole steering range is analysed, from 0 to 400 deg of steering wheel angle input, at vehicles speed ranging from 10 to 130 km/h with a steering wheel velocity of 5 deg/s (Figure 9) to keep the conditions as close to the SS but also to reduce the time of the simulation.
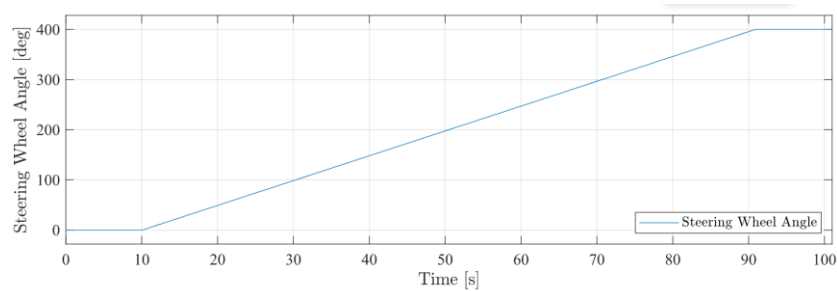
Figure 9.   Steering wheel angle input for ramp steer manoeuvre

After simulation data analysis, the yaw rate LUT shown in Figure 10 is obtained. It is also convenient to present the reference in the form of yaw rate gain, which indicates how much yaw rate is generated with respect to the average front wheel steering angle..
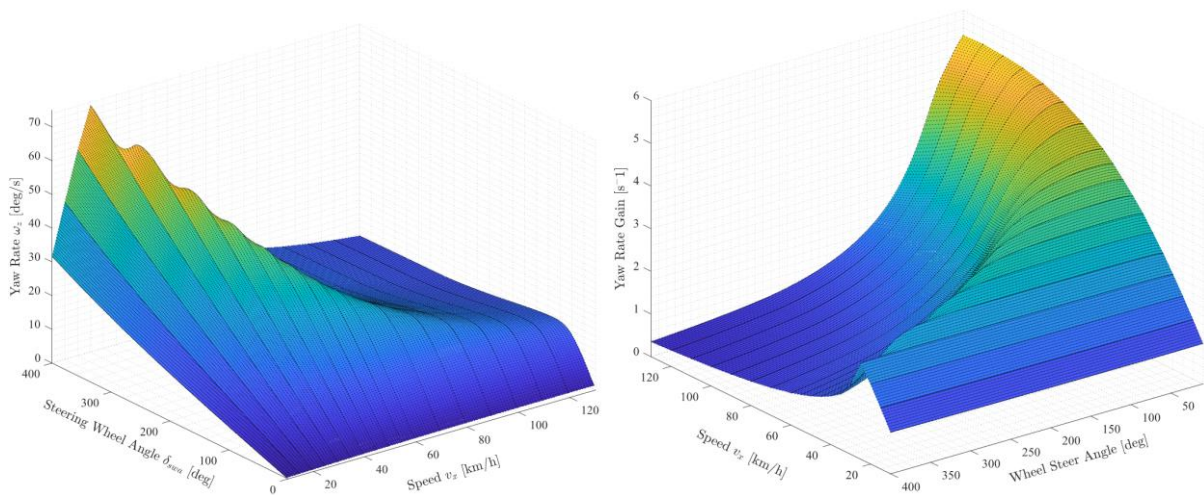
Figure 10. Yaw rate (left) and yaw rate gain (right) reference - baseline

Even by just analysing graphs in Figure 10, one can see the "neutral steer" at lower vehicle speeds up to 25 km/h over a whole steering range, while the behaviour changes at higher speeds and changes from quasi-neutral to understeer. This can be evaluated and confirmed by looking at the understeering gradient map in Figure 11. Understeering gradients over the whole steering range at various vehicle speeds are shown on the left. A comparison between yaw rate gain at low speeds with a yaw rate gain for neutral steer $K = K_{neutral} = 0$ is shown on the right.
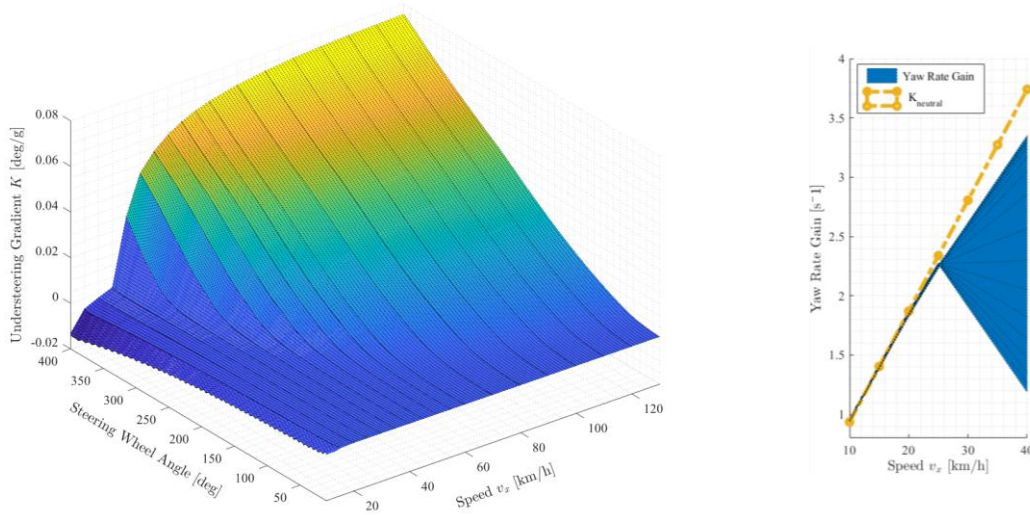
Figure 11. Understeering gradient reference (left) and yaw rate gain reference comparison to neutral steer at low speeds (right)

To evaluate how much tire potential is used to produce the yaw rate shown in Figure 10, the tire friction circle must be analysed. More information about the friction circle is given in chapter 4.1.1, but the basic idea is that there exists a resultant tire force that is calculated as follows:

$$F = \sqrt{F_x^2 + F_y^2} \leq \mu F_z \, , \qquad (9)$$

where F_x is longitudinal tire force, F_y is lateral tire force, F_z is vertical tire force, and μ is road-tire friction coefficient. By inverting Eq. (9), $F_{y,max}$ for each tire can be expressed as:

$$F_{y,max,ij} = \sqrt{\mu^2 F_{z,ij}^2 - F_{x,ij}^2}, \qquad (10)$$

And the following maximum lateral acceleration $a_{y,max}$ as a ratio of the sum of lateral forces and the vehicle mass m:

$$a_{y,max} = \frac{\sum F_{y,max,ij}}{m}. \qquad (11)$$

Lateral accelerations derived with the baseline yaw rate map and the maximum lateral accelerations for ramp steer manoeuvre are shown in Figure 12. It can be noticed that there is a potential performance being left out if the baseline yaw rate map is used. For this reason, a correction factor λ_{yaw} is introduced, which is calculated as a ratio of maximum and current lateral acceleration:

$$\lambda_{yaw} = \frac{a_{y,max}}{a_y}. \qquad (12)$$

The correction factor is calculated only for vehicle speeds above 25 km/h, and steering angles above 50 deg, saturated with the minimum value of 1 and then smoothed out with the Gaussian filter (Figure 13). The reason for this is to keep the vehicle close to the baseline while still extracting the maximum potential at higher demands. Using a SS expression $\omega_z = a_y/V$, the yaw rate map can be directly multiplied by λ_{yaw}.
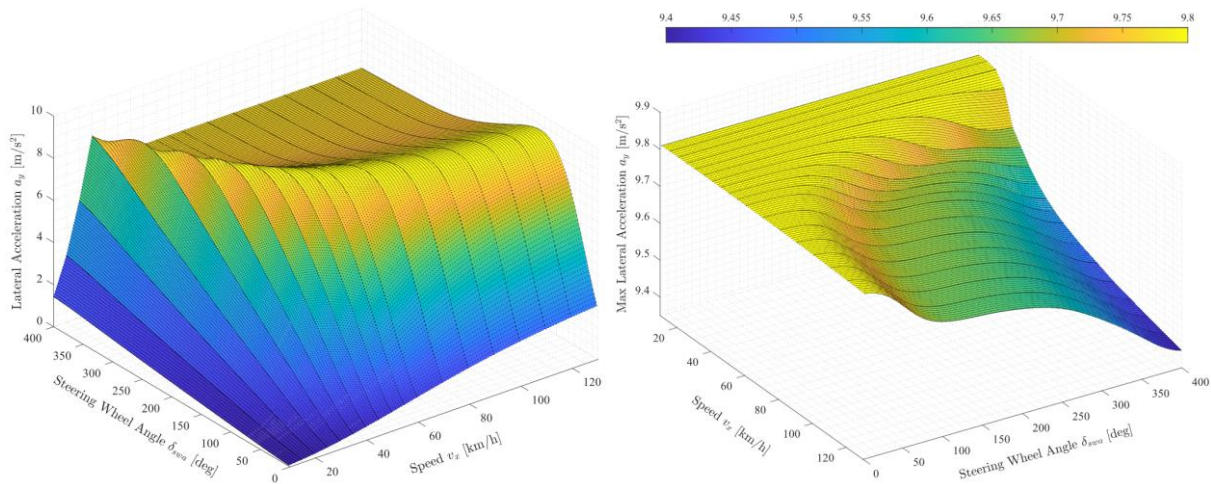
Figure 12. Lateral acceleration (left) and maximum potential lateral acceleration (right) at zero longitudinal acceleration - baseline
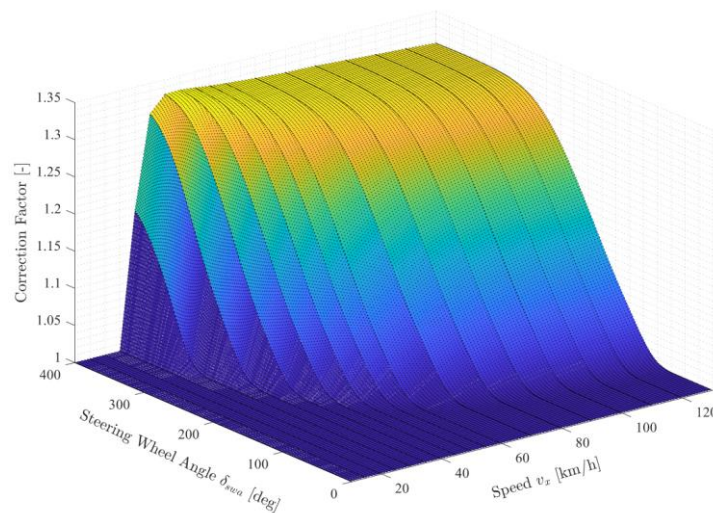
Figure 13. Yaw rate correction factor at zero longitudinal acceleration

The modified reference yaw rate at various speeds overlayed on top of the baseline reference is shown in Figure 14. It is interesting to notice the resemblance with Figure 6, where the author [7] used an empirical Piecewise expression for lateral calculation and yaw reference generation. The generated baseline and modified yaw references are saved in the LUT with vehicle speed and steering wheel angle as breakpoints. As the yaw rate reference changed,

understeering gradient (Figure 15) changed as well, changing the vehicle behaviour closer to a neutral steer and making the vehicle more reactive at speeds higher than 25 km/h.
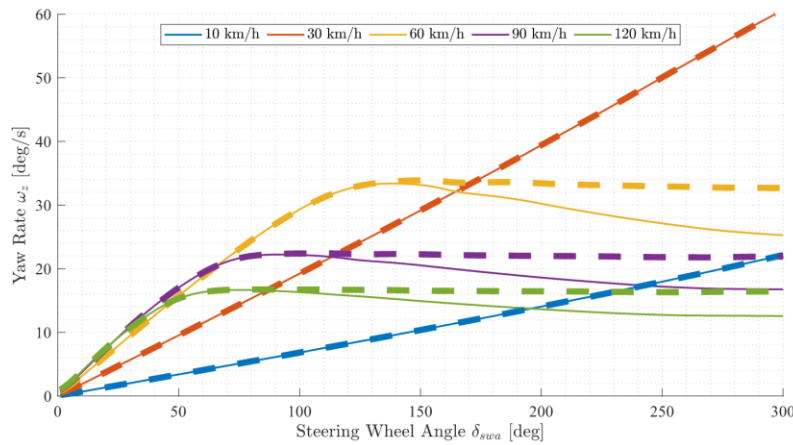
Figure 14. Baseline reference yaw rate (solid line) and modified reference yaw rate (dashed line) at zero longitudinal acceleration
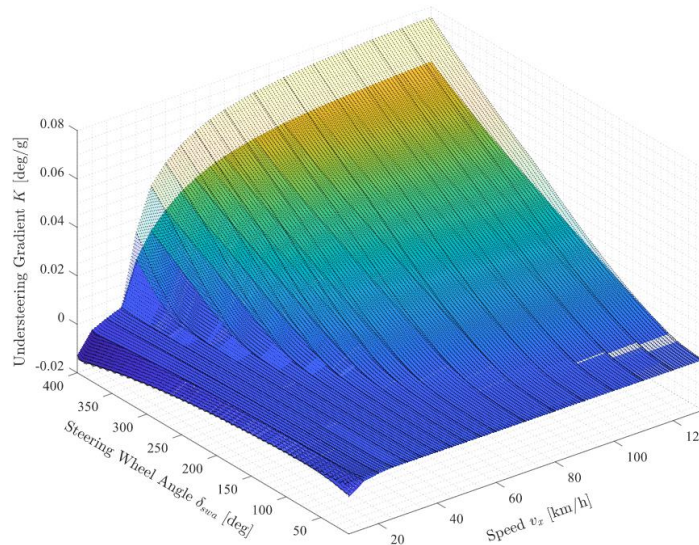
Figure 15. Baseline (mesh) and modified (surface) understeering gradient at zero longitudinal acceleration

       The influence of the correction factor λ_{yaw} on the understeering characteristics is shown in Figure 16, where the left graph shows the baseline characteristic, and the graph on the right shows the modified characteristic at various speeds from 20 to 130 km/h. Figure 17 shows the changes to the characteristic that a correction factor introduced more clearly. Maximum lateral accelerations are extended to approximately one gravity constant g, i.e. 9.81 m/s², which correlates well with expression $a_{y,max} \leq \mu g$ [9], but to confirm the expression, multiple tire-road friction coefficients μ would have to be evaluated.
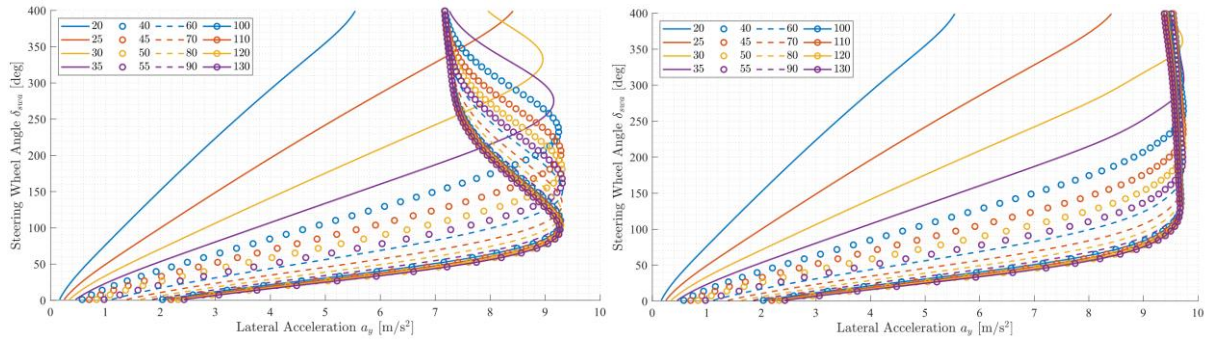
Figure 16. Understeering characteristics of a baseline (left) and modified yaw reference (right) at zero longitudinal acceleration
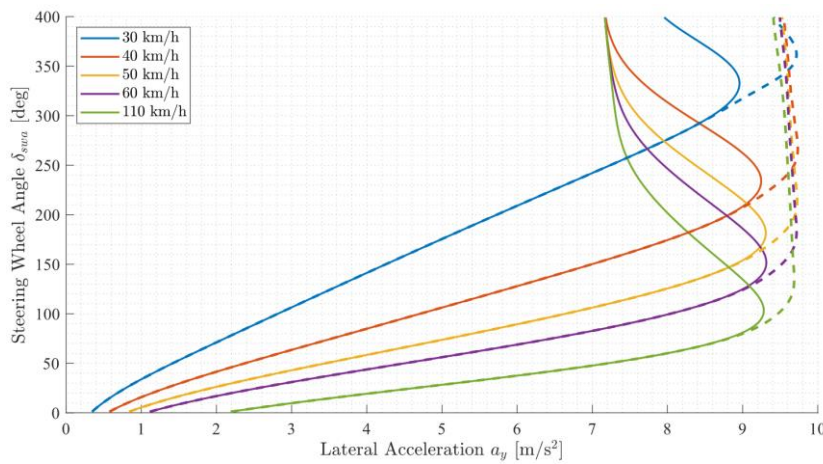
Figure 17. An increase of maximum lateral acceleration for a modified yaw reference (dashed line) at zero longitudinal acceleration

2.1.2. Transient Analysis

Presented analysis in the previous section was conducted for longitudinal acceleration $a_x = 0$, but no analysis was done on $a_x \neq 0$. This section will cover yaw rate reference for the transient vehicle behaviour. At SS conditions, there is no weight transfer due to longitudinal acceleration since it is equal to zero; thus, the vertical tire forces are influenced only by the lateral weight transfer. As was previously presented in Eq. (9), maximum lateral tire force is influenced by both the vertical tire force and the longitudinal tire force. This means that the maximum lateral value changes during the transient manoeuvre, i.e. acceleration and braking. This is also confirmed by analysing acceleration in turn for different starting turn radii (Figure 18 and Figure 19), where a constant steering wheel angle is kept after the initial portion of the manoeuvre that resembles the constant radius cornering (CRC). A higher steering angle corresponds to the manoeuvre with a smaller radius; thus, the reason for the different characteristics in Figure 18 and Figure 19. Both manoeuvres resulted in a decrease of produced yaw rate, as the longitudinal acceleration increases. The same results were obtained for the brake-in-turn manoeuvre, but the influence was more pronounced at lower vehicle speeds

because the steering wheel was fixed at a higher value (Figure 20). Nonetheless, the same behaviour can be noticed for positive and negative longitudinal acceleration. Because of this, the transient analysis is carried out only on positive accelerations, from 1 to 7 m/s^2, with steps of 1 m/s^2. It is assumed that the analysed vehicle has the same behaviour at negative accelerations, and the yaw reference generated from positive accelerations is also used for a negative portion.
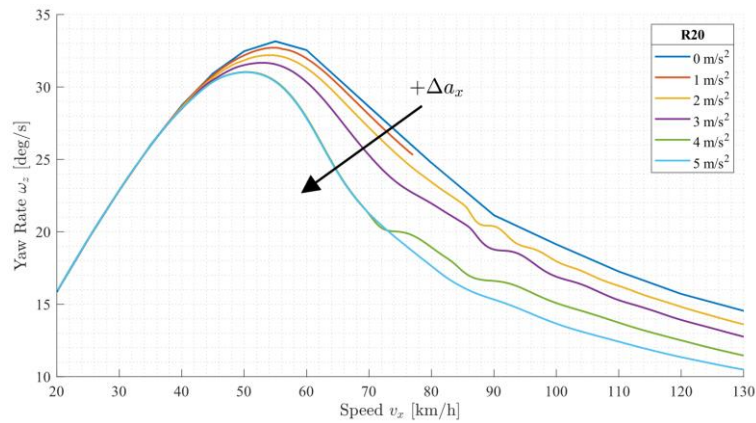
Figure 18. Positive longitudinal acceleration influence on yaw rate reference – constant steering angle at the begging of R20 acceleration in turn manoeuvre
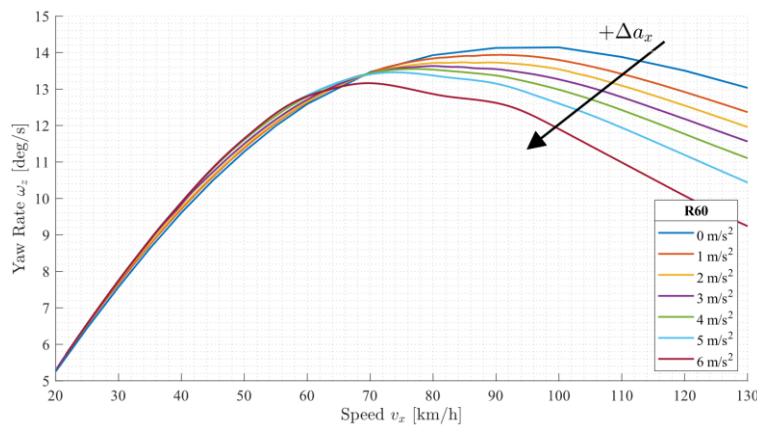
Figure 19. Positive longitudinal acceleration influence on yaw rate reference – constant steering angle at the begging of R60 acceleration in turn manoeuvre
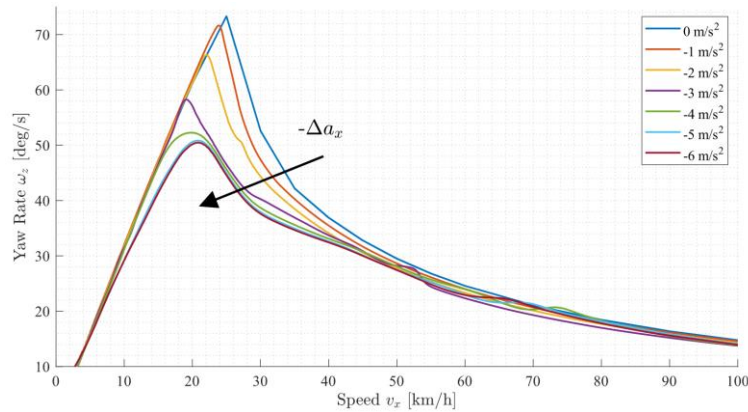
Figure 20. Negative longitudinal acceleration influence on yaw rate reference – constant steering angle at the begging of R10 brake in turn manoeuvre

As was seen previously, the yaw rate falls as the acceleration increases, and it becomes more pronounced as the speed increases. The same behaviour is observed as the steering wheel angle increases, as shown in Figure 21. It is interesting to notice that even the previously neutral steer vehicle speed of 30 km/h becomes slightly understeer at the higher steering wheel demands. Another thing to notice is that the highest decrease in the yaw rate happens just after the yaw rate 'peak'. This can also be observed in the previous figures.
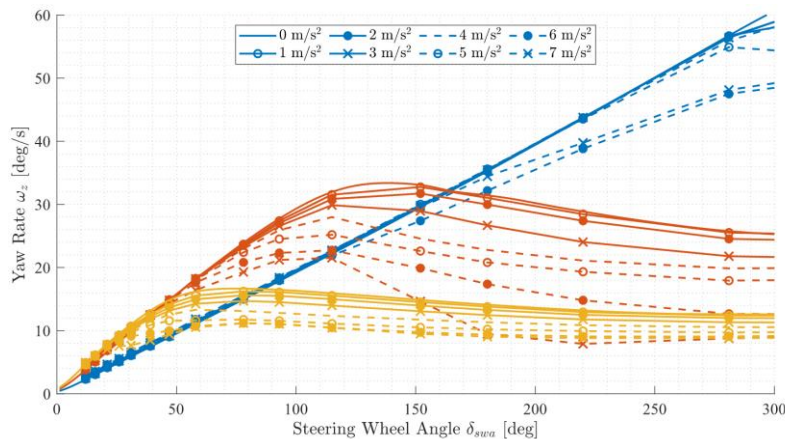
Figure 21. Longitudinal acceleration influence on baseline yaw rate reference at various speeds (blue – 30 km/h, orange – 60 km/h, yellow – 120 km/h)

To make sure full tire potential is used, the reference is once again multiplied by a correction factor λ_{yaw} which is calculated for each simulated longitudinal acceleration, even though SS conditions are not met in this part of the analysis. The modified yaw reference shown in Figure 22 resembles that shown in Figure 14. Yaw rate reference becomes flattened after passing the linear region, saturating the tire with the goal of extending the cornering performance. The generated baseline and modified yaw references during transient behaviour are saved in the LUT with vehicle speed, steering wheel angle and longitudinal acceleration as breakpoints.
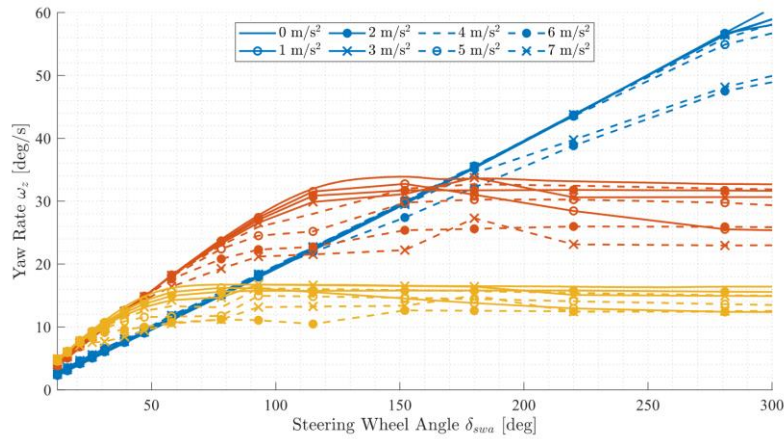
Figure 22. Longitudinal acceleration influence on modified yaw rate reference at various speeds (blue – 30 km/h, orange – 60 km/h, yellow – 120 km/h)

To analyse the influence of yaw rate drop for a vehicle speed of 60 km/h shown in Figure 21, the baseline understeering gradient is shown in Figure 23 for zero, lowest and highest evaluated lateral accelerations. The sudden drop in yaw rate resulted in an increase in vehicle understeer. On the other hand, as the longitudinal acceleration increases, the vehicle also becomes increasingly oversteer at speeds below 20 km/h, which is somewhat expected behaviour, i.e. that the vehicle tends to decrease the understeer under acceleration. The correction factor λ_{yaw} decreases both influences to a certain level, as can be seen in Figure 24, where the understeer behaviour has been significantly reduced when compared to the baseline reference, almost by a factor of two.
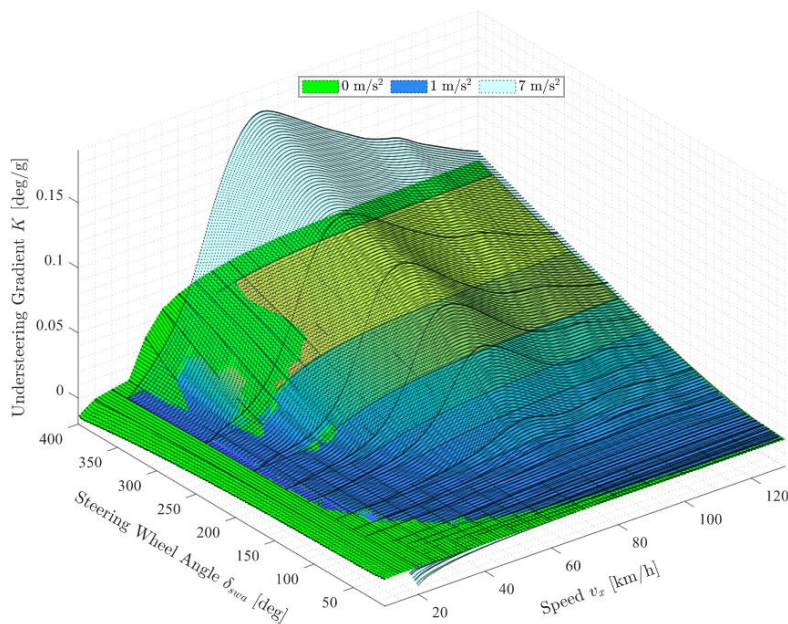
Figure 23. Baseline understeering gradient at various longitudinal accelerations
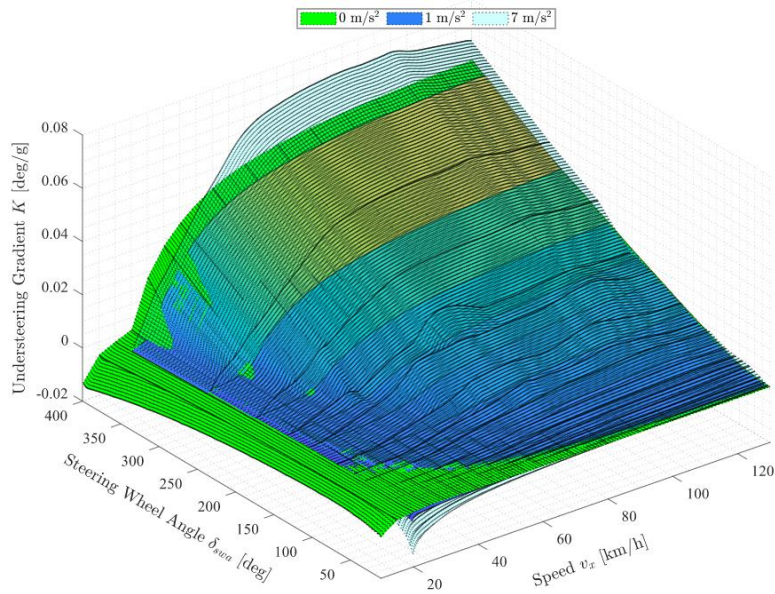
Figure 24. The modified understeering gradient at various longitudinal accelerations

As the influence of correction factor λ_{yaw} on understeering characteristic has been proved in the previous chapter (Figure 16 and Figure 17), its influence is also shown in Figure 25 for the transient case at two longitudinal accelerations. The resolution of the data is lower than the one presented in the SS analysis, and more manoeuvres would have to be performed to gain a higher resolution. When compared to Figure 17, a big difference is present on a baseline characteristic as the values of achievable lateral accelerations drop by approximately a factor of two for higher longitudinal accelerations. For lower longitudinal accelerations, i.e. $a_x = 1$ m/s^2, the difference is not that significant.
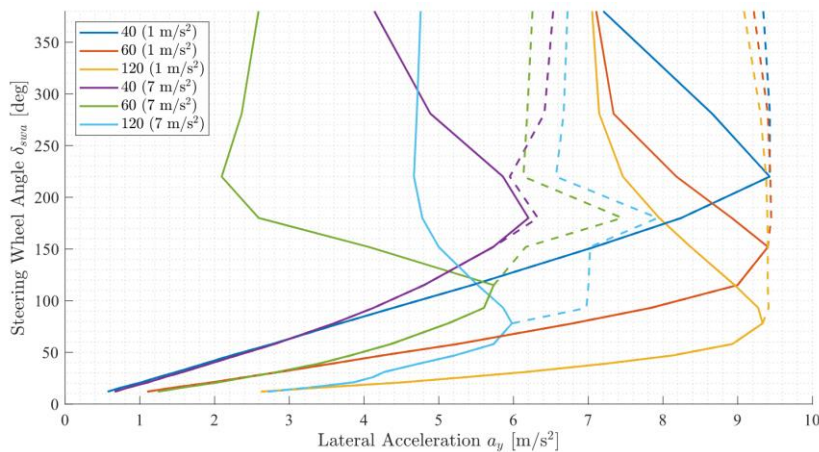
Figure 25. Understeering characteristics of a baseline (solid line) and modified yaw reference (dashed line) at the lowest and highest value of analysed the longitudinal acceleration

Finally, after analysing SS and transient vehicle behaviours, yaw reference is obtained and defined such that it maximises the lateral acceleration potentials. It is saved in the form of a LUT, as shown in Figure 26, where steering wheel angle, vehicle speed and longitudinal acceleration are the LUT breakpoints.

Figure 26. Proposed LUT-based yaw rate reference generator

2.2. Time-optimal Yaw Reference

Although a proposed approach of obtaining the yaw reference is optimal up to a certain degree from the standpoint of utilising the complete tire potential – making the vehicle more responsive at higher speeds, it might not be optimal from the lap time perspective. For that purpose, offline optimal control can be utilised, specifically time-optimal control as proposed in [7], [8] and [10] , where a simplified vehicle model was used. Single-track bicycle ([8]) and two-track vehicle models [10] are paired with the nonlinear tire model (e.g. MF tire model [13]). Due to thesis time constraints, this chapter will cover only the basic idea, motivated by [10], and present the setup for the time-optimal control problem as a base for future work, while the yaw rate reference shown in the previous section is used throughout the thesis.

The vehicle model to be used for an OCP setup will be presented first, and then the track definition, together with the basic OCP formulation and constraints being enforced by the physical limits of the vehicle and track width.

Vehicle Model

To define equations for the system, reference coordinate systems (frames) must be defined first. In order to determine the vehicle position on the track, two reference systems must be defined – global and vehicle-fixed reference frames. The global reference system (XYZ) is fixed to the track. It is assumed that the track is flat, which means that the origins of both reference systems lie on the same plane, i.e. vehicle reference system x-y plane lies on the same plane as the X-Y plane. Axes x and y can move and rotate around the fixed X and Y axes; thus, some p_X and p_Y exist and define the distances from the origin of XYZ to the xyz reference system. Since the vehicle reference system can rotate, an angle must also be defined. The x-axis marks the

vehicle's forward direction, while the y-axis denotes the lateral direction. The z-axis is perpendicular to the x-y plane, with a positive direction facing upward. Following the conventional practices as in [1] and [2], it is named yaw angle ψ. Also, each wheel must have its reference system to observe tire forces and other wheel states, as shown in Figure 27 on a two-track vehicle model used in this section. All reference systems are defined as right-handed.
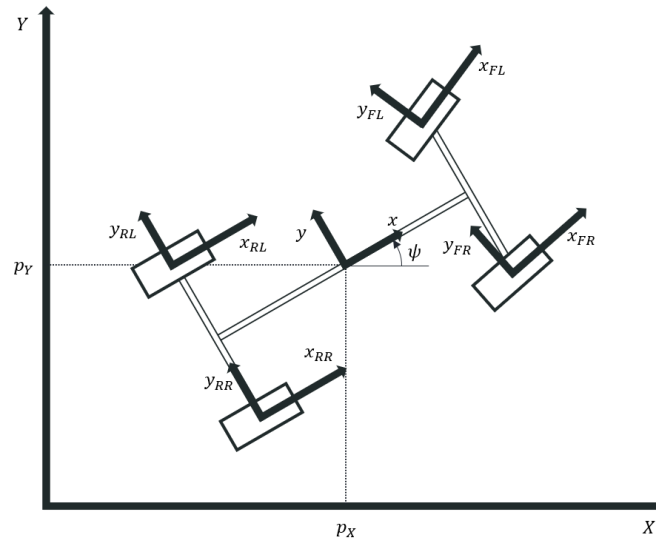
Figure 27. Reference systems
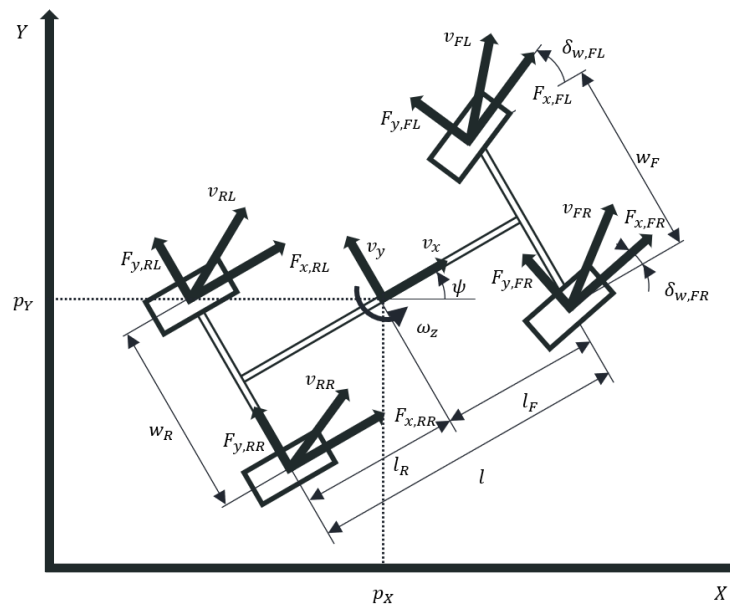
Figure 28. Vehicle states

Employing a two-track vehicle model with non-linear tires and vehicle position as defined (Figure 28), the system can be described with the following nonlinear ODE:

$$\dot{p_X} = v_x \cos \psi - v_y \sin \psi, \tag{13}$$

$$\dot{p_Y} = v_x \sin \psi + v_y \cos \psi, \tag{14}$$

$$\dot{v_x} = v_y \omega_z + \frac{F_{xx}}{m}, \tag{15}$$

$$\dot{v_y} = -v_x \omega_z + \frac{F_{yy}}{m}, \tag{16}$$

$$\dot{\psi} = \omega_z, \tag{17}$$

$$\dot{\omega_z} = \frac{M_{zz}}{I_{zz}}, \tag{18}$$

$$\dot{\delta}_{swa} = \omega_{\delta,} \tag{19}$$

$$\dot{\omega}_{ij} = \frac{1}{J_{i,\omega}} \left(T_{ij} - F_{x,ij} R_{i,e} \right), \tag{20}$$

where p_X and p_Y are the vehicle body CoG coordinates in a global inertial coordinate frame; v_x and v_y are the longitudinal and lateral vehicle speeds at the CoG; ψ is the yaw angle; ω_z is the vehicle yaw rate, and ω_{ij} are the wheel angular speeds; m is the vehicle mass; I_{zz} is the moment of inertia about the vertical axis; $J_{i,\omega}$ is the moment of inertia of each wheel about its axis of rotation; F_{xx} and F_{yy} are the total longitudinal and lateral tire forces; M_{zz} is the yaw moment; T_{ij} are the wheel torques; $F_{x,ij}$ are the longitudinal tire forces, and $R_{i,e}$ are the effective tire radii. Using Eq. (13)-(20), state and control vectors, $\boldsymbol{x}$ and $\boldsymbol{u}$ can be defined as follows:

$$\boldsymbol{x} = \begin{bmatrix} p_X \\ p_Y \\ v_x \\ v_y \\ \psi \\ \omega_z \\ \delta_{swa} \\ \omega_{FL} \\ \omega_{FR} \\ \omega_{RL} \\ \omega_{RR} \end{bmatrix} \quad \boldsymbol{u} = \begin{bmatrix} T_{FL} \\ T_{FR} \\ T_{RL} \\ T_{RR} \\ \dot{\delta}_{swa} \end{bmatrix} \tag{21}$$

where $\dot{\delta}_{swa}$ is the steering wheel angular velocity.

A number of states and controls could be reduced if the steering wheel rate $\dot{\delta}_{swa}$ was replaced with steering wheel angle directly, but in that case, additional constraints would have to be defined to tackle the rate of steering wheel angle change. Longitudinal and lateral vehicle

speeds, v_x and v_y, can also be substituted for vehicle speed V and sideslip angle β (Figure 29). The sideslip angle can be calculated after the optimisation as follows:

$$\beta = \mathrm{atan}\frac{v_y}{v_x} \tag{22}$$
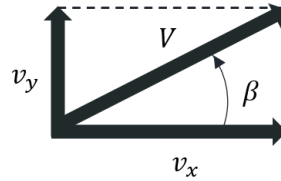
Figure 29. Vehicle sideslip angle

All longitudinal resistive forces (e.g. rolling and aerodynamic resistance) are coupled into a single resistive force expressed as a function of longitudinal vehicle speed:

$$F_{res} = A_0 + B_0 v_X + C_0 v_x^2. \tag{23}$$

For a concise notation, the following is defined:

$$S_{\delta_w} = \sin \delta_w, \qquad C_{\delta_w} = cos\, \delta_w, \tag{24}$$

$$S_\psi = \sin \psi, \qquad C_\psi = cos\, \psi. \tag{25}$$

Using Eq. (23)-(25), total longitudinal and lateral tire forces are calculated as follows:

$$F_{xx} = F_{x,FL}C_{\delta_{w,FL}} + F_{x,FR}C_{\delta_{w,FR}} - F_{y,FL}S_{\delta_{w,FL}} - F_{y,FR}S_{\delta_{w,FR}} + F_{x,RL} + F_{x,RR} - F_{res}, \tag{26}$$

$$F_{yy} = F_{x,FL}S_{\delta_{w,FL}} + F_{x,FR}S_{\delta_{w,FR}} + F_{y,FL}C_{\delta_{w,FL}} + F_{y,FR}C_{\delta_{w,FR}} + F_{y,RL} + F_{y,RR,} \tag{27}$$

where $F_{x,ij}$ and $F_{y,ij}$ are tire longitudinal and lateral forces extracted from the MF tire model [13]. Tire forces are also used to calculate yaw moment M_{zz}:

$$\begin{aligned} M_{zz} = \frac{w_F}{2}\left(F_{y,FL}S_{\delta_{w,FL}} - F_{y,FR}S_{\delta_{w,FR}} - F_{x,FL}C_{\delta_{w,FL}} + F_{x,FR}C_{\delta_{w,FR}}\right) + \\ l_F\left(F_{x,FL}S_{\delta_{w,FL}} + F_{x,FR}S_{\delta_{w,FR}} + F_{y,FL}C_{\delta_{w,FL}} + F_{y,FR}C_{\delta_{w,FR}}\right) - \\ \frac{w_R}{2}\left(F_{x,RL} - F_{x,RR}\right) - l_R\left(F_{y,RL} + F_{y,RR}\right), \end{aligned} \tag{28}$$

where $w_{F/R}$ represents the front and rear track widths and $l_{F/R}$ represents the front and rear wheelbase, i.e. horizontal distance from the centre of gravity to front and rear axle, respectively. Front wheel steering angles are extracted from the LUT, as are the maximum motor torques, which are used to define the maximum driver torque demands per wheel employing a TV distribution as proposed in [8] but decoupled into four wheel torques rather than as a

longitudinal acceleration a_x demand and an additional control yaw moment M_{zz}. For this reason, Eq. (29) and (30) are defined to express the connection from the motor to wheel torque.

$$\omega_{FL/FR} = \frac{\omega_{m,FL/FR}}{i_F}, \qquad\qquad \omega_{RL/RR} = \frac{\omega_{m,RL/RR}}{i_R}, \qquad (29)$$

$$T_{FL/FR} = i_F\, T_{m,FL/FR}, \qquad\qquad T_{RL/RR} = i_R T_{m,RL/RR}. \qquad (30)$$

Track definition

The track that an optimal control problem is being set up on is of a U shape (Figure 30), generally called a U-turn, that consists of two straights (SL) and a constant radius bend. The U-turn is chosen ([10] and [11]) because it offers a greater proportion of time spent in slowly-varying conditions compared to other manoeuvres, like a J-turn.
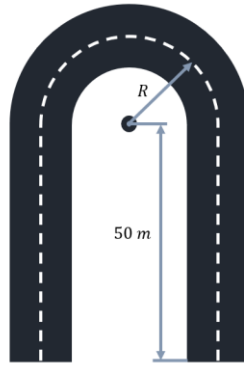
Figure 30. U-turn example

Unlike the [10], [11] and [12], vehicle position on the track is not formulated through the use of spatial coordinate s. Although there are disadvantages to this approach, which is out of the scope of this thesis, vehicle position on the track is defined by using a finite number of track centreline points defining the track. This means that there only can be a finite number of vehicle positions as well. By increasing the number of points, the problem becomes larger and will take more time to solve. The general idea of how a constraint for vehicle position on the track is formulated is using coordinates p_X and p_Y and X and Y coordinates defining the track centreline. At any given point of the track, there exists equal length to the right and to the left of the centreline; thus, the constraint for vehicle position can be expressed in a way that the vehicle must stay within a circle of a defined radius that corresponds to the half of track width. Mathematically this can be expressed as follows:

$$[p_X(t) - X(t)]^2 + [p_Y(t) - Y(t)]^2 \leq \left(\frac{w_{track}}{2}\right)^2 \qquad (31)$$

where w_{track} is the track width.

Optimal Control Problem

The solution of the benchmark optimal problem for the TV distribution would show how an ideal, i.e. optimal driver would drive, extracting the maximum performance of the vehicle and driving the vehicle at the limit of adhesion. To this aim, an optimal control problem is formulated. The OCP is intended to go from an initial to the final point of a track in a minimum time while considering vehicle and track limitations. The objective is to generate time or distance histories of the controls and the corresponding vehicle states. The OCP may be mathematically formulated as follows. Given a dynamic system in the form:

$$\dot{x} = f\big(x(t), u(t)\big),$$ (32)

Subject to initial and final conditions:

$$x(t_0) = x_0, \qquad\qquad x\big(t_f\big) = x_f,$$ (33)

where state and control vectors x and u are as defined in Eq. (21). The problem is to find the control vector u which seeks to minimise a certain cost function J, which is subjected to equality and inequality constraints p and g:

$$J = \phi\big[x\big(t_f\big)\big] + + \int_{t_0}^{t_f} L[x(t), u(t)],$$ (34)

$$p[x(t), u(t)] = 0, \qquad\qquad g[x(t), u(t)] \leq 0.$$ (35)

To minimise the time to complete the manoeuvre, a cost function can be represented by only the integral term:

$$J = \int_{t_0}^{t_f} dt = t_f.$$ (36)

Thus the OCP is stated as follows:

$$\min_{x,u} t_F = \int_{t_0}^{t_f} dt.$$ (37)

The steering wheel angle δ_{swa} is constrained to a maximum value for a given vehicle, and driver physical limits are accounted for by setting a constraint on a steering wheel angular velocity $\dot{\delta}_{swa}$. Motor torques $T_{m,ij}$ are limited by the aforementioned LUT map defining the maximum motor torque for a given wheel angular velocity $\omega_{m,ij}$. To solve the presented OCP, tools like an open-source CasADI [14] or a licensed GPOPS-II [15] can be used to transcribe the continuous-time OCP into a discrete nonlinear programming problem (NLP). Interior-point solver IPOPT [16] could be used to solve the constructed NLP.

3. YAW MOMENT CONTROLLER

3.1. Controller Overview

3.1.1. PID Controller

PID controllers (Figure 31) are used over a wide variety of applications in the industry. Most engineers are familiarised with them, which is why it is so widespread. PID controllers act upon the error, the derivative, and the integral of the error between a set reference and an actual state value. Ease of implementation and minimal computational requirements are considered to be the main advantage of a PID controller. This can result in easier tuning. Also, PID controllers are relatively robust, i.e. they can withstand changes in vehicle model without compromising the vehicle's stability.

On the other hand, because of its simplicity, a PID controller cannot by itself exploit a complete knowledge of the vehicle dynamics model (i.e. if the vehicle model is ideally identified, a PID controller is outperformed by other algorithms like SMC [19]). Due to PID advantages, they are quite spread as a yaw controller. They mostly appear as a classic PID controllers with feed-forward terms or as a PI controller, but more recently, there have been a few papers (e.g. [20] and [21]) that covered the PD^3 controller.
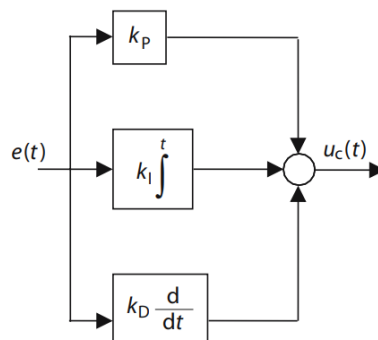
Figure 31. General time domain representation of a PID controller [17]

3.1.2. Sliding Mode Controller (SMC)

Sliding Mode Control (SMC) uses a large gain to force a dynamic system to follow a trajectory of a reduced-order system. The main advantage of SMC is its robustness against modelling uncertainties. On the other hand, its main disadvantage is that the controller is usually highly active, i.e. the actuators are continuously saturated, provoking chattering that may damage the electric motors. Dead-band, low-pass, or integral filters are used to reduce chattering issues. SMC has also been used in combination with PID and the first-order, second-order and integral sliding control.
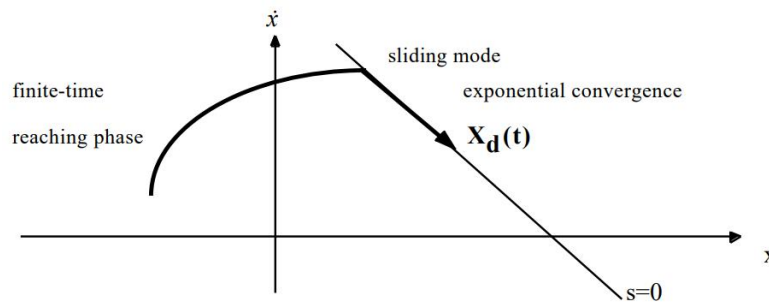
Figure 32. General graphical interpretation of SMC equations [18]

3.1.3. Linear Quadratic Regulator (LQR) and Linear Quadratic Gaussian (LQG)

Linear Quadratic Regulators (LQR) are optimal controllers that balance the tracking of the state variables (i.e. minimisation of the overall error of the yaw rate) with the actuation (i.e. commanded asymmetrical torque on the wheels). The simplest LQRs minimise the integral of a weighted sum of the squared error and the square of the actuation values. The proper selection of the cost (minimisation) function provides very effective results. As the gains for the LQR are obtained by solving the corresponding Riccati equation [22], LQR is very sensitive to vehicle mismodelling or different perturbations (e.g. disturbances, parameter uncertainties, etc.). They are also usually applied only to linear or close-to-linear systems. Linear Quadratic Gaussian (LQG) is a variant of LQR that includes disturbances (e.g. side winds) in form of Gaussian noise. The effect of disturbances can be minimised if tuned properly. The use of these controllers is limited since the application of these controllers requires the linearisation of the model around a working point because the vehicle dynamics is not linear, especially at handling limits. Another possible approach is using a gain scheduling method performed in linear parameter-varying controllers (LPV).

3.1.4. Fuzzy Logic Controller

Fuzzy logic controllers have also been applied to yaw control (e.g. [23]). They have three main parts: fuzzification, rule processor, and defuzzification. The control designer usually states the rules intuitively, e.g. "if the yaw rate error is large, apply a large wheel torque to diminish it". The fuzzification converts the input measurements into qualitative quantities (i.e. what is considered as a "large" or "huge" yaw error etc.). The regions between the quantities usually overlap. The defuzzification consists of generating the specific control action according to the output rules (e.g. "a huge wheel torque is at least 500 Nm"). These three parts of the controllers require an in-depth knowledge of the process under study. Nevertheless, fuzzy controllers have been successfully applied.

3.1.5.　Model Predictive Controller

Model Predictive Control (MPC) is similar to LQRs with some key differences. They are similar in that they both solve an optimisation problem that trades off tracking and the actuation. However, the approach is different since the optimisation problem is solved online. This primarily introduces additional computational costs. MPCs can also include non-linearities (such as actuator saturation) if the optimisation solver can deal with them. Moreover, the optimisation problem is solved for a finite-time horizon. MPCs can be applied to either linear or non-linear vehicle models. Their performance is better when used with the non-linear models, but this may introduce even more computational cost since the model is more complicated and introduces more states that need to be optimised. More recently, there has been a surge in MPC use in the automotive industry. Since the computation cost is high, they are mainly used with linear models, but many papers have shown that non-linear models improve performance (e.g. [29] and [30]).

3.1.6.　Performance Evaluation

The performance of several controllers mentioned above is evaluated in [24] by running the simulations on the Olaberria and Hockenheim racetrack. The data of Olaberria lap times are shown in Table 1, where the learning rate represents how the driver adapts his driving style lap to lap (0 – sensitive, 1.5 – aggressive) and "Driver Target" represents the target accelerations for the driver, i.e. the maximum accelerations he strives to achieve. Did not finish (DNF) means that the driver has spun out of the track or that any of the wheels have locked up (obviously happening only at the high G-G). It is also evident that the best lap time is achieved with higher G-G exponents and that the difference in lap times across different controllers is tiny.

Table 1.　Lap times at Olaberria [24]

Race Driver Parameters		Lap Times				
Learning Rate	**Driver Target (G-G Exponent)**	**PID**	**SMC**	**LQR**	**MPC**	**LPV-MPC**
0	1	36.92	36.94	36.73	36.78	36.80
0.5	1.2	36.13	36.26	35.97	35.99	36.07
0.7	1.4	35.68	35.78	35.50	35.55	35.62
1	1.6	35.33	35.48	35.14	35.28	35.32
1.5	1.8	35.12	35.42	34.98	35.16	35.11
1.5	2	35.10	35.27	34.88	35.13	35.00
1.5	2.2	**34.85**	**35.23**	**34.80**	**34.82**	**34.78**
1.5	2.3	DNF	DNF	DNF	DNF	DNF

The best lap times for different controllers are within the tenth of a second, which is interesting, but it doesn't say a lot about the overall performance of the controllers. To compare the performance or rather actuation of the controllers, [24] has proposed to use:

- Integral of the absolute yaw rate error (IAE):

$$IAE = \int_{0}^{t_{lap}} \left\| e(t) \right\| dt \quad \text{[rad]}, \tag{38}$$

- Integral of the absolute value of the control action ($IACA$):

$$IACA = \int_{0}^{t_{lap}} \left\| u(t) \right\| dt \quad \text{[Nms]}. \tag{39}$$

Table 2 evaluates the controller performance. Among the controllers, the LPV-MPC achieves the fastest lap time, but the PID intervenes less than the other controllers ($IACA$ value) by more than half. This means that it has lower energy consumption. It can be observed by IAE that the MPC keeps the error to the minimum but at the expense of an intense controller intervention. It's evident that a compromise between a busy controller and energy consumption must be made.

Table 2.   **Controller performance at Olaberria [24]**

Controller	Lap Time	Best Lap Olaberria	
		IACA	**IAE**
PID	34.85	**3103**	7.34
SMC	35.23	6660	7.70
LQR	34.80	6867	6.77
MPC	34.82	8105	**5.63**
LPV-MPC	**34.78**	5130	8.39

Interestingly, the yaw rate error is not critical for lap times, as shown in [24]. Both in Hockenheim and Olaberria, MPC and LPV-MPC have the smallest IAE and the largest $IACA$, and the lap times are within the same tenth of a second. As can be seen in Table 2, MPC is slower than LPV-MPV, even if IAE is smaller for the MPC. The difference is more notable on the Hockenheim circuit, where the difference is a tenth of a second. Another example is shown in Figure 33, where the PID controller has been tuned in two ways – by running simulations to get the best lap time and by running simulations to get a low yaw rate error. At first glance, one would say that the first tune is not good or that the controller cannot follow the reference, but it is evident that the yaw rate error is not strictly connected to the best lap time on the track, as

stated before. The reference is generated using the bicycle vehicle model [24], which could also be the reason for slower lap time with the PID controller tuned for better reference following, i.e. overall lower yaw rate error.
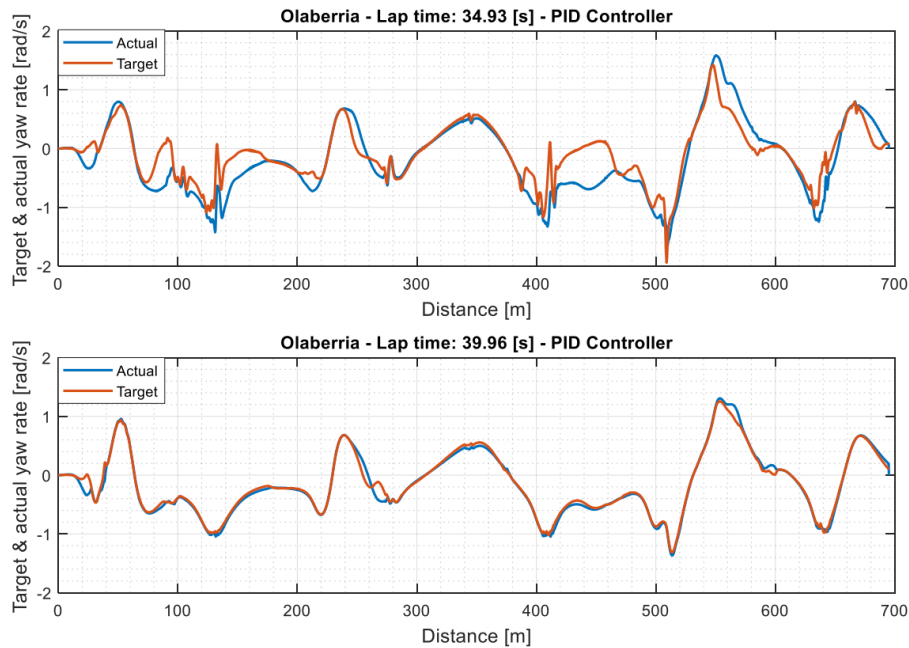
Figure 33. Target and actual yaw rate in a "fast" and a "slow" lap - PID controller [24]

3.2. Selection of Controller Design

When choosing the controller, the obvious choice would be to compromise between complexity (time dedication) and the response quality of the controller. MPC is not considered due to the time constraint (research and model setup). LQR and fuzzy controllers have shown average results in some ISO manoeuvres (e.g. [23]). Still, outside of those, their performance was not satisfactory, although it was shown that they could improve the performance of PID controllers by cascading them ([25], [26]). Sliding mode controller is interesting for yaw control, but as it produces chattering, it's not an optimal choice because it can damage the motors over a more extended period and may result in higher energy consumption, even though it's not the focus of this thesis. The only logical choice remains to use a combination of a PID controller. Many papers and articles have shown that the performance of a PID controller can, in most cases, match the performance of the MPCs, and that's why it's also interesting to investigate the possibility of using a simple and common PID controller. Now the only decision left is to choose what combination would be used.

The results from [20], where they compared a PD^3 controller, to a traction control-only system and a system using NMPC for yaw moment control, are shown in Figure 34 and Figure

35. The results represent a real-world implementation, where a real driver drove the car, so the time misalignment is present. Table 3 indicates that the vehicle speed is higher when using the PD^3 controller. Still, the brake pedal demand is higher, which might be okay if we ignore brake disc wear and overheating potential. Figure 35 displays the additional control yaw moment, control error and the gap time with the PD^3 controller as a baseline. It can be observed that the PD^3 controller has a faster lap time when compared to the NMPC and traction control-only system. This faster lap time is a result of the higher vehicle speed when using the PD^3 controller. The interesting thing is that the PD^3 controller has a higher yaw rate error and does not follow the reference as well as the other controllers. It is also characterised by a higher control yaw moment, meaning that a higher control input is required from the motors.

Nevertheless, it is interesting that a control yaw moment is about 55% higher when using the NMPC compared to the PD^3 controller. This means that energy consumption and heat generation are increased as well. Since the focus for the yaw reference is the fastest manoeuvring time, the focus of the yaw moment controller is set to be the same; thus, these disadvantages are ignored. Control yaw moment is about ten times lower when only using the traction control system, so it makes no sense to compare it to the yaw control system.
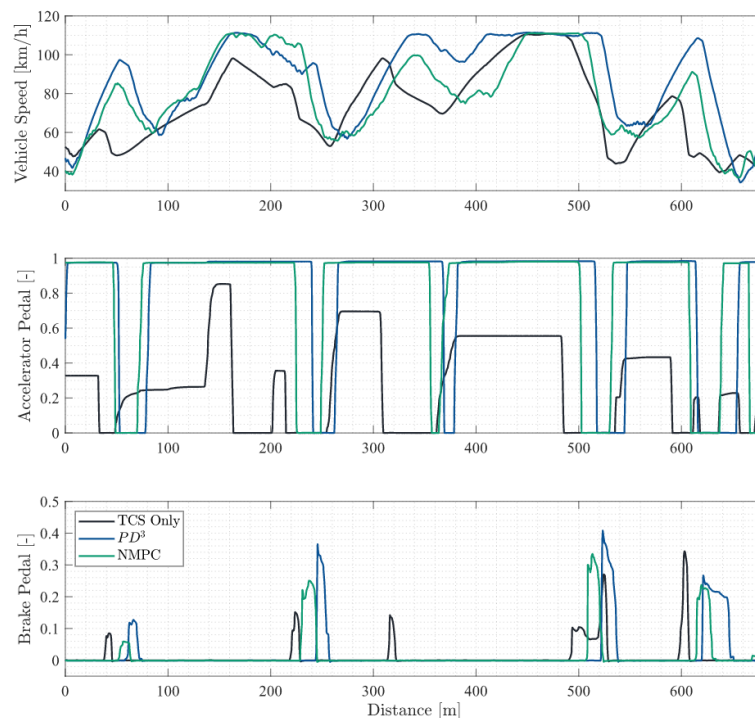
Figure 34. Vehicle speed, accelerator, and brake pedal signals – comparison of TCS only, PD^3 and NMPC system [20]
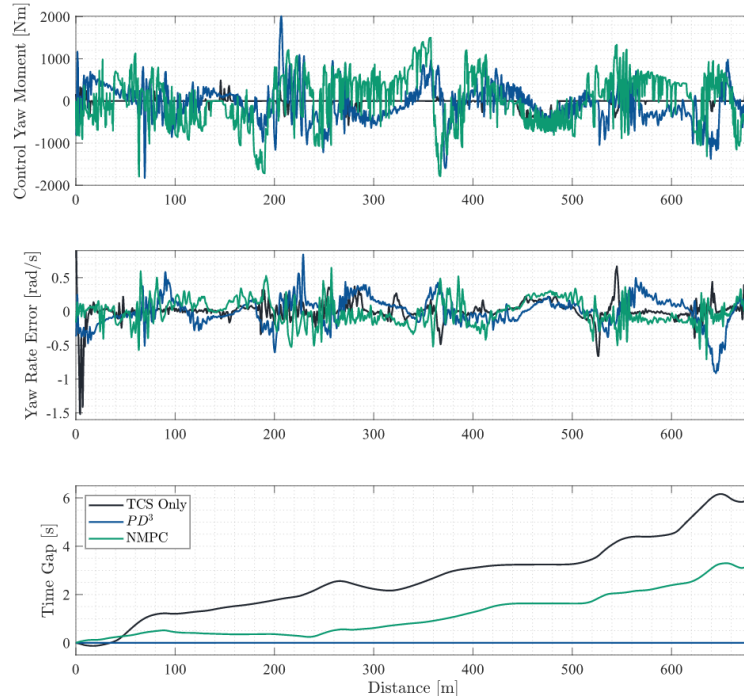
Figure 35. Control yaw moment, yaw rate error and time gap signals - comparison of TCS only, PD³ and NMPC system [20]

3.2.1. *PD³ Controller*

Based upon the general simplicity and performance metrics regarding lap time covered in [20], [21] and [24], a PD^3 controller is selected and slightly modified. In general, the tracking yaw rate error e_{ω_z} can be expressed as:

$$e = e_{\omega_z} = \omega_{z,ref} - \omega_z,$$
(40)

where $\omega_{z,ref}$ is the yaw rate reference extracted from the LUT (Figure 26). The basic expression for a classic PID controller for a SISO system [17] (Figure 31):

$$u(t) = Pe(t) + I \int e(t)d\tau + D\dot{e}(t),$$
(41)

where $u(t)$ is the controller output; P, I and D are the proportional, integral, and derivative controller gains; $e(t)$ and $\dot{e}(t)$ are the tracking error and its derivative. The output from the controller in this section is the vehicle yaw moment $M_{z,des}$; thus, the Eq. (**41**) expressed for a yaw moment PD^3 controller reads as follows:

$$M_{z,des} = P\left(e_{\omega_z}^*\right)^3 + D\left(\dot{e}_{\omega_z}^*\right)^3,$$
(42)

where $e_{\omega_z}^*$ and $\dot{e}_{\omega_z}^*$ are the scaled values yaw rate error and derivative of the error:

$$e_{\omega_z}^* = \frac{e_{\omega_z}}{\lambda_{err}}.$$
(43)

The yaw rate scaling factor λ_{err} is introduced as a LUT to define a threshold for what is considered a minor yaw error. This way, adaptive yaw error rescaling is introduced as different driving conditions may require a different amount of controller intervention. Since the scaling factor has been introduced, proportional and derivative gain values, P and D, are set as a constant. The initial value for P is determined from the aforementioned ramp steer manoeuvre as a ratio of the yaw moment produced by an uncontrolled baseline vehicle and the yaw rate over a range of velocities and steering wheel angles. The final values of controller gains (proportional, derivative) are set by running batch simulations and evaluating best lap times, which was shown to be the best approach by [24].

At first, it seems weird not to have any integral influence and to pair proportional error with only the derivative of error, which can introduce a lot of chatter if the controller is not tuned well. The absence of an integral term in the proposed control is justified for several reasons. First, it was shown in Figure 33 ([24]) that a low yaw rate error does not necessarily equate to a better-performing controller, if looking at the minimum lap time. Second, the largest errors in Figure 33 are present only when SS or quasi-SS behaviour is present, which the proposed PD^3 controller cannot deal with as well. The overall PID performance during transient behaviours follows the reference well, as is expected from the proposed PD^3 controller. Although the PID parameters of a PID controller presented in [24] are not available, the aforementioned behaviour points toward the preference of proportional and derivative terms.

Also, although the use of cubic error might seem unnecessary, there are several advantages over a standard yaw rate error given in Eq. (40). First, by introducing a cubic error, we neglect minor deviations, defined as values $e^*_{\omega_z} \leq 1$, while reacting to significant errors, which can predict loss of stability in case of oversteering. Neglecting minor yaw errors may provide information to the driver about the road conditions, i.e. allow the driver to "feel the road" and test the vehicle's handling.

Second, due to the error cube features, the controller exhibits high robustness against modelling uncertainties compared to other controllers (if MPC is neglected). It also might deal better with the nonlinear region than the linear error controller. Also, PD^3 is suitable in situations where a significant delay is present, mainly because of communication delays and gear backlash. In general, anything above 10 ms may be considered a significant delay.

Furthermore, controller intervention in unnecessary situations where small deviations are present is avoided, something that would be the case if a classic PID controller was used.

The main disadvantage of a PD^3 controller is that it usually must be run in parallel with the side slip angle controller to stay within the yaw moment limits, especially if a significant delay is present. An additional side slip angle controller could be avoided to some extent if the output of the PD^3 controller is saturated, but it is recommended that it is nevertheless used.

Even while taking all of this into account, several papers (e.g. [20] and [24]) have shown that the PD^3 controller can have slightly better to significantly better lap times when compared to other conventional controllers that are believed to be state-of-the-art (e.g. NMPC), as was shown in Figure 34 and Figure 35.

A proposed PD^3 controller is shown in Figure 36. The controller first rescales the yaw rate error and then takes a cube function of it and passes it further. Controller gains could also be implemented as a LUT, but that is something for future work. This would enable even more control over the controller output, but that would also mean that there are four values that need to be calibrated. The output of the controller is saturated. The output saturation function will be covered in 4.2 in more detail, but in short, this saturation acts as a desired yaw moment security measure to avoid excessive side slip angle.
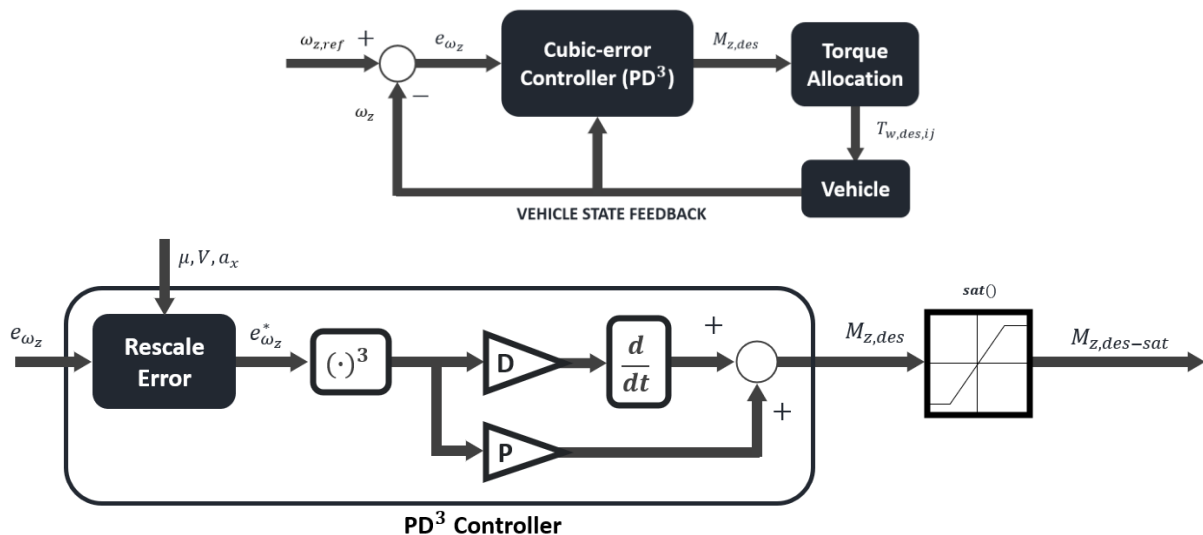
Figure 36. Proposed yaw moment PD^3 controller

As a basis for future work and eventual improvements if deemed necessary, the integral term could also be included by taking the non-scaled linear yaw rate error e_{ω_z}, making the controller PD^3- I. The basic idea is shown on Figure 37. Using this controller, the SS reference tracking problem could be tackled, although it would need to be tested out to be sure.
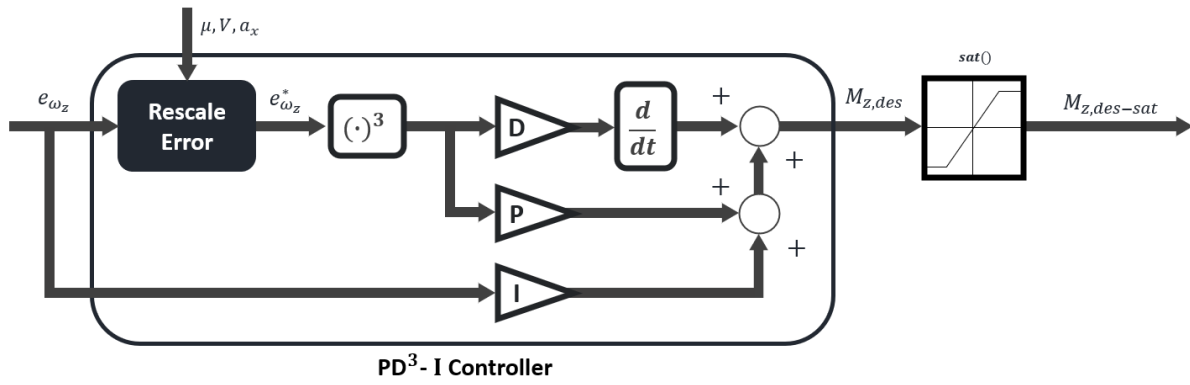
Figure 37. An alternative yaw moment PD^3- I controller

4. TORQUE ALLOCATION

4.1. Maximum Wheel Torques

The maximum wheel torques are determined from the tire friction circle and motor torque-rotational speed curve as illustrated in Figure 38.
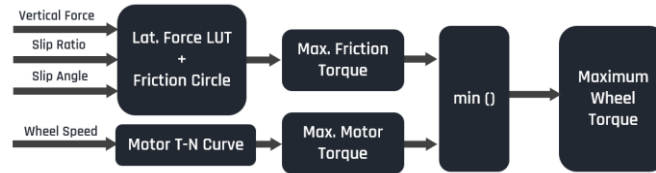
Figure 38. Maximum wheel torque definition

It's important to point out that the proposed approach of determining the maximum wheel torques does not consider many factors, like the state of charge of the high-voltage battery and its thermal properties. It also ignores the thermal states of the motors and their controllers and motor controller DC link voltages which could also affect the maximum values.

4.1.1. Maximum Positive Wheel Torque

Before defining maximum positive torques, vertical tire forces, longitudinal wheel slip ratios, and wheel slip angles need to be defined. These three wheel/tire states will be used for the tire model and later for torque calculations.

Vertical Tire Forces

Vertical tire forces are calculated as a sum of static and dynamic weight distribution while also considering the aerodynamic forces. The general algorithm idea is shown in Figure 39.
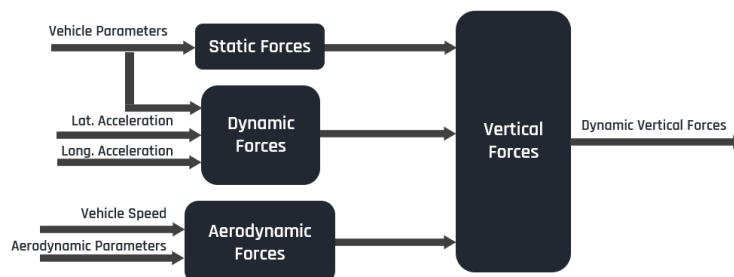
Figure 39. Vertical tire force estimation

Vehicle parameters are represented by a two-track vehicle model shown in Figure 40, where parameters h_{CoG} and h_{CoP} represent the height of the centre of gravity and the centre of pressure.
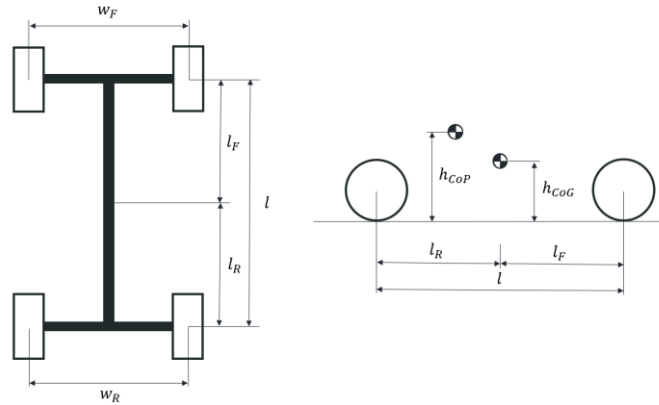
Figure 40. Two-track vehicle model - vehicle parameters

Static forces are calculated using a basic weight distribution over the four wheels:

$$F_{z,stat} = \frac{l_{F/R}}{2l} mg.$$ (44)

Dynamic forces are calculated as follows:

$$F_{z,dyn} = \mp \frac{h_{CoG}}{2l} ma_x \mp \frac{l_{F/R}}{l} \frac{h_{CoG}}{w_{F/R}} ma_y.$$ (45)

Aerodynamic drag is represented only by the longitudinal portion:

$$F_{x,drag} = \frac{1}{2} v_x^2 C_d A_{aero} \rho_{air},$$ (46)

While the aerodynamic downforce is calculated as:

$$F_{z,downforce} = \frac{1}{2} v_x^2 C_{l\frac{F}{R}} A_{aero} \rho_{air}.$$ (47)

Air density ρ_{air} is set to a constant value as are the aerodynamic coefficients C_d and $C_{lF/R}$.

Vehicle projected frontal area A_{aero} is represented in Figure 41, and it's a constant as well.
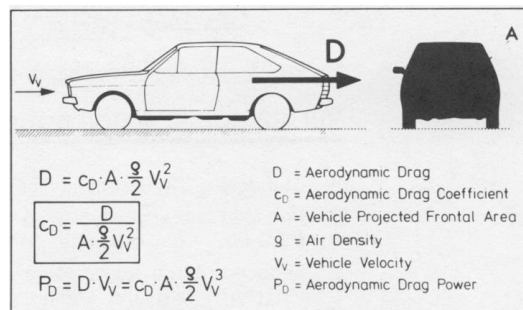
Figure 41. Definition of aerodynamic drag coefficient [27]

After summing up the above equations, vertical tire forces $F_z = f(a_x, a_y, v_x)$ are calculated as follows:

$$F_{z,FL} = \frac{m}{l}\left(\frac{l_R}{2}g - \frac{h_{CoG}}{2}a_x - l_R\frac{h_{CoG}}{w_F}a_y\right) + \frac{1}{2}v_x^2 A_{aero}\rho_{air}\left(\frac{C_{lF}}{l} - h_{CoP}C_d\right),$$

$$F_{z,FR} = \frac{m}{l}\left(\frac{l_R}{2}g - \frac{h_{CoG}}{2}a_x + l_R\frac{h_{CoG}}{w_F}a_y\right) + \frac{1}{2}v_x^2 A_{aero}\rho_{air}\left(\frac{C_{lF}}{l} - h_{CoP}C_d\right),$$

$$(48)$$

$$F_{z,RL} = \frac{m}{l}\left(\frac{l_F}{2}g + \frac{h_{CoG}}{2}a_x - l_F\frac{h_{CoG}}{w_R}a_y\right) + \frac{1}{2}v_x^2 A_{aero}\rho_{air}\left(\frac{C_{lR}}{l} + h_{CoP}C_d\right),$$

$$F_{z,RR} = \frac{m}{l}\left(\frac{l_F}{2}g + \frac{h_{CoG}}{2}a_x + l_F\frac{h_{CoG}}{w_R}a_y\right) + \frac{1}{2}v_x^2 A_{aero}\rho_{air}\left(\frac{C_{lR}}{l} + h_{CoP}C_d\right).$$

Longitudinal Wheel Slip Ratio

The longitudinal wheel slip ratio is calculated using the difference between wheel speed ($v_{r,ij}$) and the longitudinal vehicle speed translated to the wheel reference system ($v_{x,ij-whl}$), as specified by expressions (49), and dividing it by $v_{x,ij-whl}$.

$$v_{x,FL/FR-veh} = v_x \mp \frac{w_F}{2}\omega_z \quad v_{y,FL/FR-veh} = v_y + l_F\omega_z,$$

$$v_{x,FL/FR-whl} = v_{x,FL/FR-veh}\cos\delta_{w_{FL/FR}} + v_{y,FL/FR-veh}\sin\delta_{w_{FL/FR}},$$

$$(49)$$

$$v_{x,RL/RR-whl} = v_{x,RL/RR} = v_x \mp \frac{w_R}{2}\omega_z$$

$$\sigma_{x,FL/FR} = \frac{v_{r,FL/FR} - v_{x,FL/FR-whl}}{v_{x,FL/FR-whl}},$$

$$(50)$$

$$\sigma_{x,RL/RR} = \frac{v_{r,RL/RR} - v_{x,RL/RR}}{v_{x,RL/RR}},$$

Wheel Slip Angle

Wheel slip angle α is defined as shown in Figure 42, i.e as defined in Eq. (52).
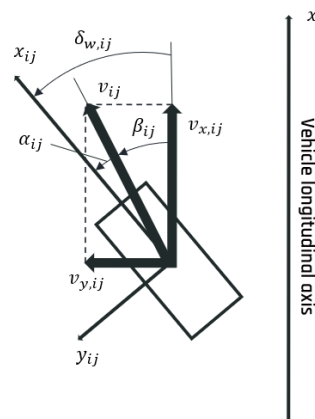
Figure 42. Wheel slip angle definition

$$v_{y,FL/FR-whl} = v_{y,FL/FR-veh} C_{\delta_{w_{FL/FR}}} - v_{x,FL/FR-veh} S_{\delta_{w_{FL/FR}}},$$

$$\tag{51}$$

$$v_{y,RL/RR-whl} = v_{y,RL/RR} = v_y - l_R \omega_z$$

$$\alpha_{FL/FR} = \text{atan} \frac{v_{y,FL/FR-whl}}{v_{x,FL/FR-whl}}$$

$$\tag{52}$$

$$\alpha_{RL/RR} = \text{atan} \frac{v_{y,RL/RR}}{v_{x,RL/RR}}$$

Tire Model

Tire characteristics, i.e tire forces are calculated using the Magic Formula (MF) tire model, a widely used semi-empirical tire model used to calculate steady-state values. The general form of the formula is:

$$y = D \sin[C \, \text{atan}^{-1}\{Bx - E(Bx - atan(Bx))\}],\tag{53}$$

$$Y(X) = y(x) + S_V,$$

$$x = X + S_H,$$

where Y is the output variable (tire force/moment) and X the input variable, and parameters B, C, D, E, S_V and S_H are calculated from MF parameters as given in [13]. The model is derived for pure slip (54) as follows:

$$F_{x_0} = f(F_z, \sigma_x) = D_x \sin[C_x \, atan\{B_x\sigma_x - E_x(B_x\sigma_x - atan(B_x\sigma_x))\}] + S_{V_x}.$$

$$\tag{54}$$

$$F_{y_0} = f(F_z, \alpha) = D_y \sin[C_y \, atan\{B_y\alpha - E_y(B_y\alpha - atan(B_y\alpha))\}] + S_{V_y}.$$

Eq. (53) and (54) are illustrated on Figure 43 and Figure 44 for the tire parameters used in this thesis.
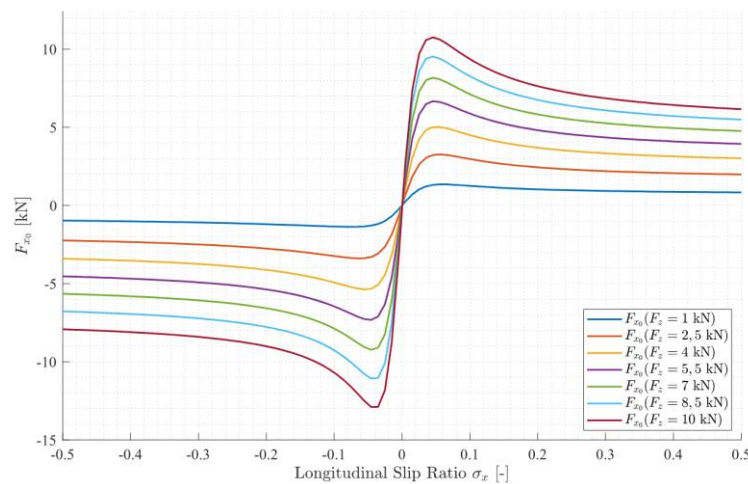
Figure 43. Longitudinal tire force at several vertical loads – pure longitudinal slip
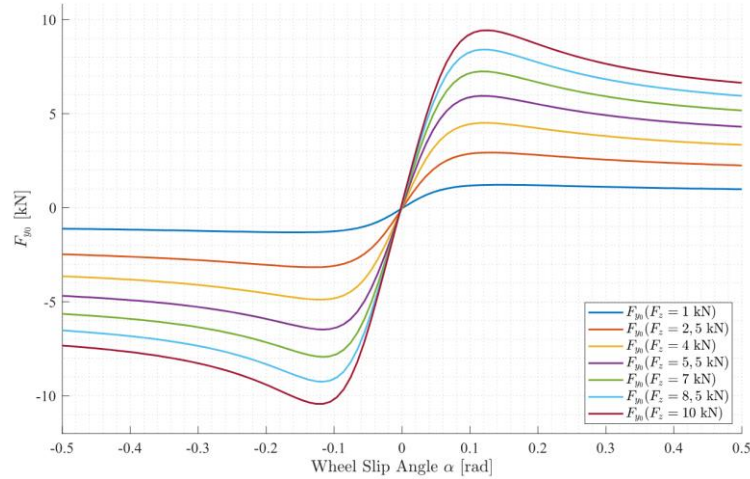
Figure 44. Lateral tire force at several vertical loads – pure lateral slip

Although the typical approach (e.g. [10]) is to use the simple MF tire model with pure longitudinal and lateral slips as defined by expression (54), this thesis will make use of the MF tire model with combined slip. The main reason for this approach is shown in Figure 45, where the influence of combined slip is present. Lateral slip σ_y is closely connected to the wheel slip angle α and can be considered equal for the purpose of this thesis. Longitudinal slip is defined differently by [13], thus the negative value for positive force in Figure 45. For the combined slip, the model is derived as follows:

$$
\begin{aligned}
F_x &= f(F_z, \sigma_x, \alpha) = G_{x\alpha} F_{x_o}, \\
F_y &= f(F_z, \sigma_x, \alpha) = G_{y\sigma_x} F_{y_o} + S_{V_{y\sigma_x}},
\end{aligned}
\tag{55}
$$

where $G_{x\alpha}$ and $G_{y\sigma_x}$ are the weighting functions calculated from MF parameters as given in [13]. To better represent the combined slip influence, longitudinal and lateral forces are also shown in 3D in Figure 46 for a constant vertical load, with the colourmap representing the tire force value. Since the tire force is also dependent on the vertical load, a 4D tire model is needed, which can be represented by a 3D plot with a heatmap, as shown in Figure 47.
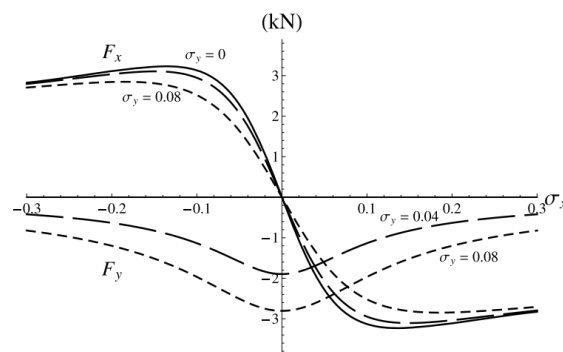
Figure 45. Longitudinal and lateral force due to combined slip, for a constant vertical load [13] – 2D
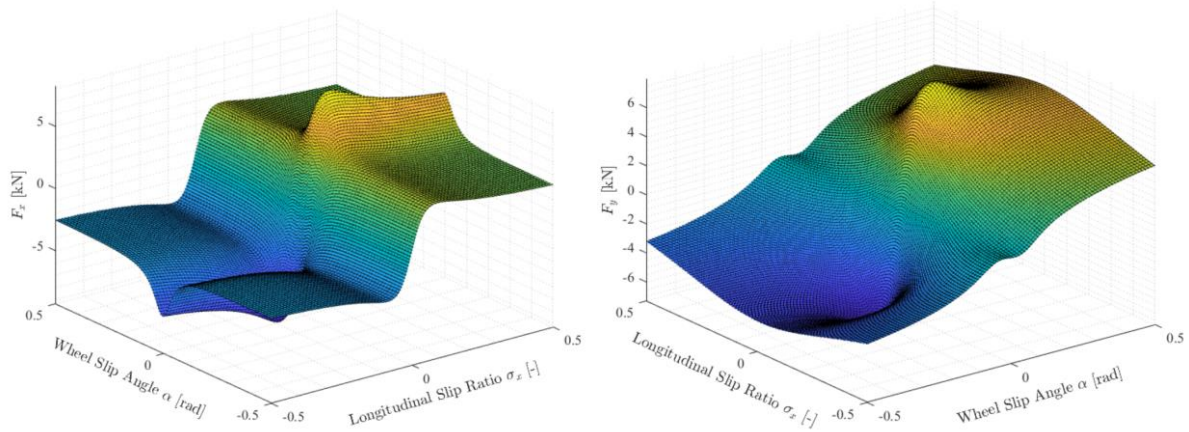
Figure 46. Longitudinal and lateral force due to combined slip, for a constant vertical load – 3D
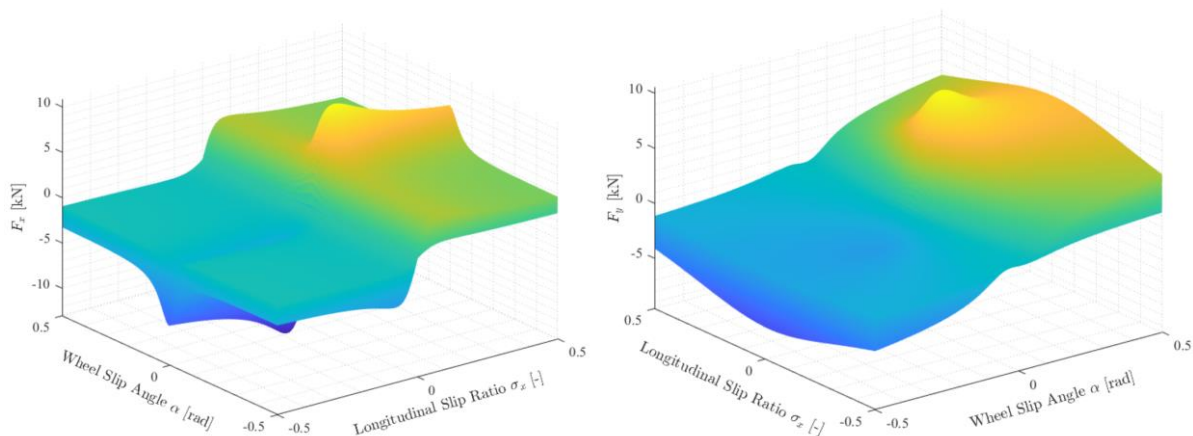
Figure 47. Longitudinal and lateral tire force at several vertical loads – combined slip

Wheel Torque

After obtaining the vertical and lateral tire forces, the only thing left to define is the maximum friction torque. The proposed approach uses the tire friction circle ($F_x - F_y$ graph, also called $\mu_x - \mu_y$) where the lateral force is extracted from the right LUT shown in Figure 47. The friction circle ensures that the tire never enters the unstable area considered as an "out of control" area shown in Figure 48. The physical values defining the friction circle are represented in Figure 49, where the x and y axes represent longitudinal and lateral friction coefficients, respectively. Both coefficients are calculated as a ratio between the current longitudinal and lateral tire force with respect to the vertical tire force.
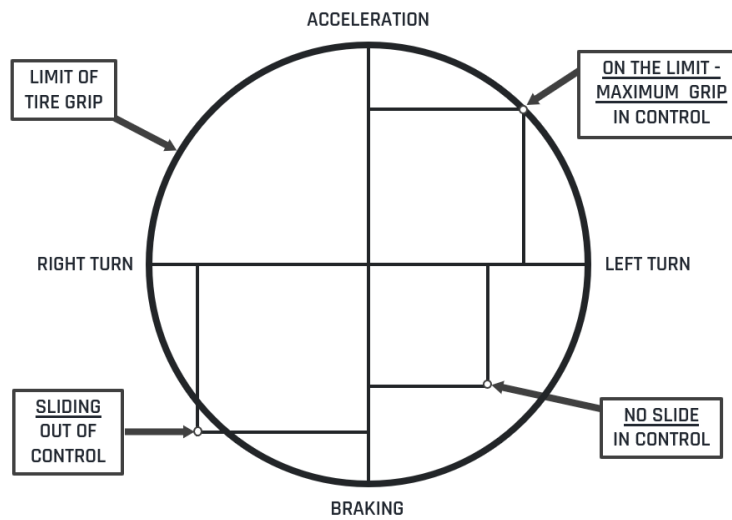
Figure 48. Friction circle – possible tire states
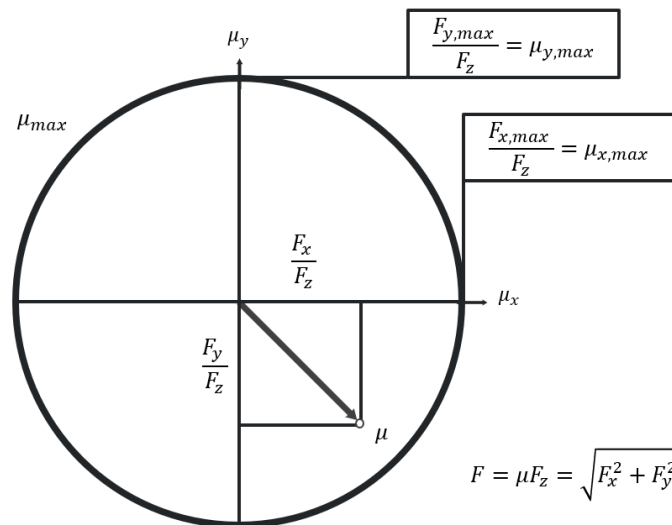
Figure 49. Friction circle – physical representation

Under the assumption that the tire friction force is linearly dependent on the vertical tire force and the friction circle definition given in Figure 49, the following is true:

$$F = \mu F_z = \sqrt{F_x^2 + F_y^2}. \tag{56}$$

To account for any tire model uncertainties, a scaling factor $\lambda_{F/R,const} \in [0,1]$ is implemented. This scaling factor is also supposed to be a tuning parameter and is just another safety measure not to exceed the tire grip limit. Having this in mind, the maximum friction torque can be defined as:

$$T_{w,max-fric} = \lambda_{F/R,const} R_e \sqrt{\mu^2 F_z^2 + F_y^2}. \tag{57}$$

Maximum positive motor torque is determined from the motor map of each motor, according to its current rotational speed, and then multiplied by the gear ratios to obtain wheel torques:

$$T_{w,TN} = i_{F/R} T_{m,TN}. \tag{58}$$

By choosing the minimum value between the calculated wheel torque from the friction circle, and the maximum torque from the motor curve, the maximum positive wheel torque is determined as follows:

$$T_{w,max} = \min(T_{w,max-fric}, T_{w,TN}), \tag{59}$$

This way, the maximum torque considers both the electrical characteristics $(T_{w,TN})$ of IWM and the physical tire characteristics $(T_{w,max-fric})$. The general algorithm idea is shown on Figure 38. Since the motor torque depends on the available voltage, the T-N curve could also be extended to account for the motor controller DC link voltage.

4.1.2. Maximum negative wheel torque

Maximum negative wheel torque is determined just like the maximum positive wheel torque, as a minimum value of motor curve and maximum friction torque, but with some modifications. Also, the following equations are derived as the negative wheel torques are positive values. Maximum regenerative motor torque is determined from the generator map of each motor, according to its current rotational speed, and then multiplied by the gear ratios to obtain wheel torques:

$$T_{w,TN-reg} = i_{F/R} T_{m,TN-reg}. \tag{60}$$

That wheel torque is then used to obtain a correction factor $\lambda_{F/R,reg}$ that is calculated as follows:

$$\lambda_{F/R,reg} = \min\left(\lambda_{F/R,const-reg}, \frac{T_{w,max}}{T_{w,TN-reg}}\right),$$

$$\lambda_{F/R,const-reg} \in [0,1], \tag{61}$$

where $\lambda_{F/R,const-reg}$ is a correction value set by the user. The correction factor ensures that we are consistently below the friction limit, either by using the user pre-set constant or by looking at the friction to generator map torque ratio, whichever is lowest. Finally, the maximum regenerative wheel torque is chosen as follows:

$$T_{w,max-reg} = \min(T_{w,lim-reg}, \lambda_{F/R,reg} T_{w,TN-reg}), \tag{62}$$

where $T_{w,lim-reg} > 0$ is a limit value set by the user.

4.2. Maximum Yaw Moment

After obtaining the maximum wheel torques, positive and negative, their values can be used to calculate the maximum yaw moments they produce. For readability, the yaw moments are calculated as follows:

$$M_{z,t-front} = \frac{w_F}{2R_e} \begin{cases} \left(C_{\delta_{w,FR}} T_{w,max,FR} - C_{\delta_{w,FL}} T_{w,max-reg,FL}\right) & if\ M_{z,des} \geq 0 \\ \left(C_{\delta_{w,FL}} T_{w,max,FL} - C_{\delta_{w,FR}} T_{w,max-reg,FR}\right) & otherwise \end{cases}, \tag{63}$$

$$M_{z,t-rear} = \frac{w_R}{2R_e} \begin{cases} \left(T_{w,max,RR} - T_{w,max-reg,RL}\right) & if\ M_{z,des} \geq 0 \\ \left(T_{w,max,RL} - T_{w,max-reg,RR}\right) & otherwise \end{cases}, \tag{64}$$

$$M_{z,wb-front} = \frac{l_F}{R_e} \begin{cases} \left(S_{\delta_{w,FR}} T_{w,max,FR} + S_{\delta_{w,FL}} T_{w,max-reg,FL}\right) & if\ M_{z,des} \geq 0 \\ \left(-S_{\delta_{w,FL}} T_{w,max,FL} - S_{\delta_{w,FR}} T_{w,max-reg,FR}\right) & otherwise \end{cases}, \tag{65}$$

where $M_{z,t-front}$ and $M_{z,t-rear}$ are the yaw moments produced on the front and rear tracks respectively, and $M_{z,wb-front}$ is the yaw moment produced on the front wheelbase. Eq. (63)-(65) are derived with negative values for negative wheel torques. Using the expressions from these equations, the maximum yaw moment can be calculated as follows:

$$M_{z,max} = M_{z,t-front} + M_{z,t-rear} + M_{z,wb-front}. \tag{66}$$

Three things are to be noticed. First, the maximum yaw moment (66) is not calculated as in (28) because the lateral forces are not controlled directly, even though they are to change due to changes in wheel torques. Eq. (66) is thus the maximum yaw moment that can be produced directly by changing the wheel torques. Second, to understand signs next to the corresponding torques in Eq. (65), it's essential to analyse the contribution of front wheel force components, that the front wheel torques produce, to the maximum yaw moment. By analysing Figure 50, which represents the different steering situations with expected yaw demands, one can notice that one force component continuously decreases the maximum potential yaw moment, specifically the negative lateral component that the negative wheel torque produces. The same behaviour can be seen in Figure 51, but with positive wheel torques. The behaviour shown in Figure 51 may be intuitively less likely, but it can happen, especially after passing the corner apex and turning out of the corner, or when applying countersteering.
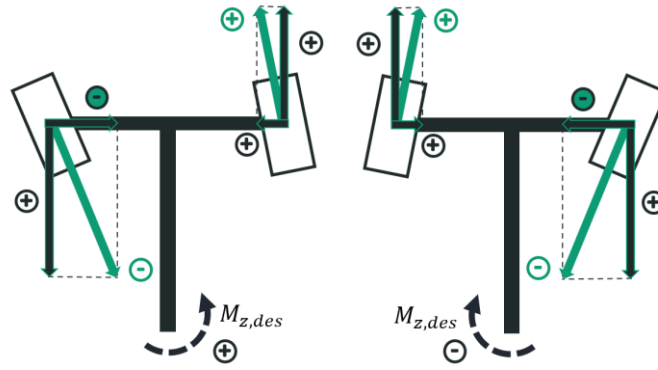
Figure 50. Front wheel force component contribution to the yaw moment – intuitive cases
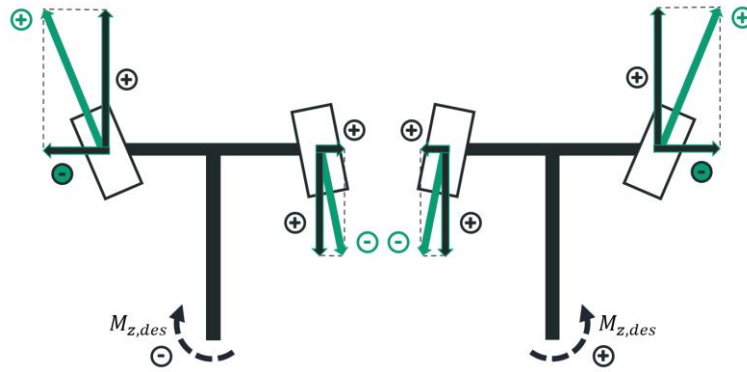
Figure 51. Front wheel force component contribution to the yaw moment – unintuitive cases

Lastly, for $\delta_w \to 0$, Eq. (66) can be expressed as:

$$M_{z,max} = \begin{cases} \dfrac{w_F}{2R_e}\left(T_{w,max,FR} - T_{w,max-reg,FL}\right) + \dfrac{w_R}{2R_e}\left(T_{w,max,RR} - T_{w,max-reg,FL}\right) if\ M_{z,des} \geq 0 \\ \dfrac{w_F}{2R_e}\left(T_{w,max,FL} - T_{w,max-reg,FR}\right) + \dfrac{w_R}{2R_e}\left(T_{w,max,RL} - T_{w,max-reg,FR}\right)\ \ otherwise \end{cases}, \quad (67)$$

Which resembles the equation for the calculation of the maximum yaw moment for rear two-wheel drivetrain configuration:

$$M_{z,max-2RWD} = \begin{cases} \dfrac{w_R}{2R_e}\left(T_{w,max,RR} - T_{w,max-reg,RL}\right) & if\ M_{z,des} \geq 0 \\ \dfrac{w_R}{2R_e}\left(T_{w,max,RL} - T_{w,max-reg,RR}\right) & otherwise \end{cases}. \quad (68)$$

As mentioned before in subchapter 3.2.1, for safety reasons, the desired yaw moment $M_{z,des}$, produced by the yaw moment controller, is limited to the range $[-M_{z,max}, M_{z,max}]$.

4.3. Torque distribution

To produce the desired yaw moment, wheel torques must be distributed. It is desirable to operate only positive motor torques since a large negative motor torque at high wheel speed may cause both the deterioration of motor durability and mechanical parts connected to it. It could also bring the wheel to an unstable state, i.e. wheel locking or extensive slipping. Also,

prioritising the positive torques makes the vehicle more likely to keep its speed or accelerate. However, in situations when a large amount of yaw moment is required, both the positive and negative torques within the torque operation area are to be allowed, i.e. $[-abs(T_{w,\max-\mathrm{reg}}),$ $T_{w,max}]$ for each wheel.

The torque distribution could be performed either by online or offline allocation. Online allocation implies using cost function (e.g. energy consumption minimisation). It usually demands more work to set up but brings an optimal result for a given cost function. The online allocation also depends on the model's accuracy and is very sensitive to nonlinearities, disturbances, etc. On the other hand, offline allocation is easier to set up and may bring a result close to the optimal one, depending on the goal and implementation.

4.3.1. *Daisy-chain control allocation – conventional and modified*

Daisy-chaining method ([28]) for redundant actuators is quite an effective allocation method that meets the requirement that the positive torque is preferred over the negative torque. It is both a simple and intuitive way of offline allocation. Its fundamental idea is that the relationship between the virtual input v and actuator inputs u_N is given as follows:

$$v = B_1 u_1 + B_2 u_2 + \cdots + B_N u_N, \tag{69}$$

where B is a control vector/matrix. If v is not satisfied by the first input u_1, the second input u_2 is generated to satisfy the remainder. In the same way, more than two inputs can be allocated to satisfy the virtual input, so this method could even be used on drivetrain configuration with more than two electric motors. The expressions of the conventional Daisy-chaining allocation actuator inputs are as follows:

$$u_1 = sat_{u_1}(B_1^{-1}v),$$

$$u_2 = sat_{u_2}(B_2^{-1}(v - B_1 u_1),$$

$$\vdots \tag{70}$$

$$u_N = sat_{u_N}\left(B_N^{-1}\left(v - \sum_{k=1}^{N-1} B_k u_k\right)\right).$$

To better understand the method, virtual input v will be first derived for a 2RW drivetrain configuration, as in [19]. Then a proposed allocation will be derived for a four-wheel configuration in the next chapter. The v is derived as shown in Figure 52 where v is $M_{z,des}$, u_1 is $T_{w,des,RR}$, and u_2 is $T_{w,des,RL}$, while $B_{1/2}$ corresponds to $w_R/2R_e$. This figure also shows the

conventional algorithm structure, while Figure 53 represents the conventional torque distribution, where $i = RL, RR$.
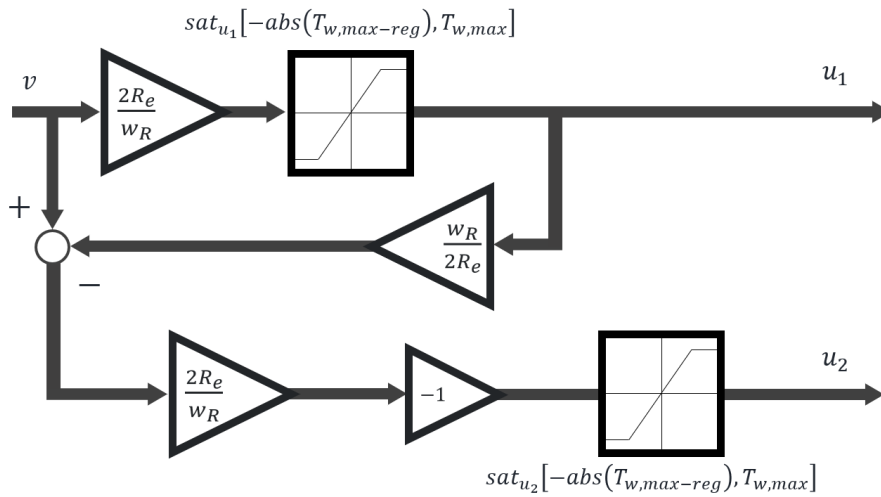
Figure 52. Conventional control allocation algorithm structure
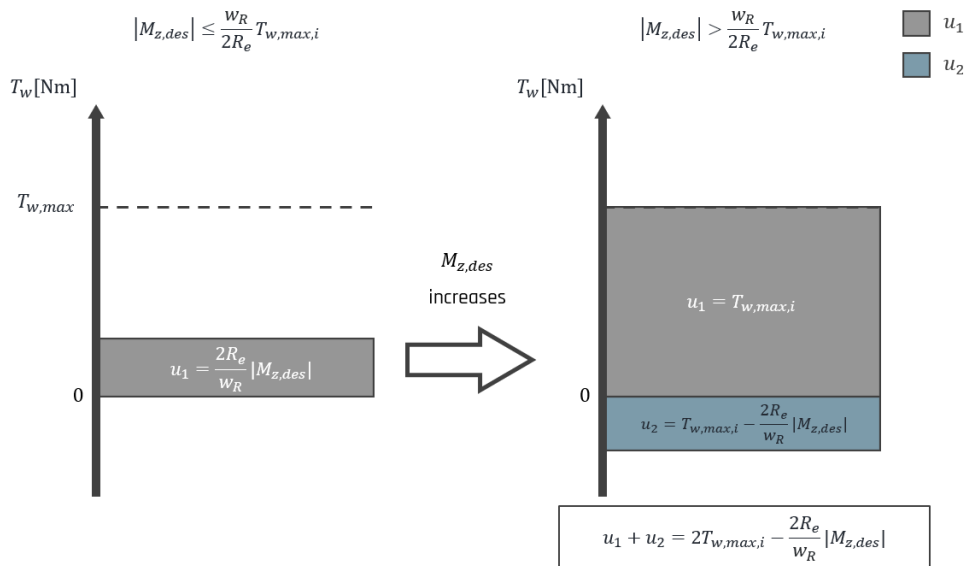
Figure 53. Torque distribution – conventional structure

Based on the presented information, the torque distribution for the conventional approach is derived as follows:

$$T_{w,des,RL} = \begin{cases} T_{w,max,RL} & if\ M_{z,des} < -\dfrac{w_R}{2R_e}T_{w,max,RL} \\[2ex] -\dfrac{2R_e}{w_R}\left|M_{z,des}\right| & if\ -\dfrac{w_R}{2R_e}T_{w,max,RL} \le M_{z,des} < 0 \\[2ex] 0 & if\ 0 \le M_{z,des} \le \dfrac{w_R}{2R_e}T_{w,max,RR} \\[2ex] T_{w,max,RR} - \dfrac{2R_e}{w_R}\left|M_{z,des}\right| & if\ \dfrac{w_R}{2R_e}T_{m,max,RR} < M_{z,des} \end{cases} ,$$

$$(71)$$

$$T_{w,des,RR} = \begin{cases} T_{w,max,RR} - \dfrac{2R_e}{w_R}\left|M_{z,des}\right| & if\ M_{z,des} < -\dfrac{w_R}{2R_e}T_{w,max,RL} \\[2ex] 0 & if\ -\dfrac{w_R}{2R_e}T_{w,max,RL} \le M_{z,des} < 0 \\[2ex] \dfrac{2R_e}{w_R}\left|M_{z,des}\right| & if\ 0 \le M_{z,des} \le \dfrac{w_R}{2R_e}T_{w,max,RR} \\[2ex] T_{w,max,RR} & if\ \dfrac{w_R}{2R_e}T_{m,max,RR} < M_{z,des} \end{cases} .$$

To have an adaptable timing of the negative motor torque intervention, a constant tuning parameter $\alpha \in [0,1]$, set by the user, is introduced. Figure 54 and Figure 55 show the modified algorithm structure, proposed in [19], and torque distribution, with the tuning parameter α. It is important to point out that the tuning parameter does not limit the maximum motor torque but acts as a virtual limit to the positive torque in a way that the positive torque is applied up to the threshold that is defined by α and maximum yaw moment $M_{z,max}$ as shown in Figure 55 and defined by Eq. (72). After that threshold is reached, the negative torque starts being applied up to its limit, as defined in Eq. (72).
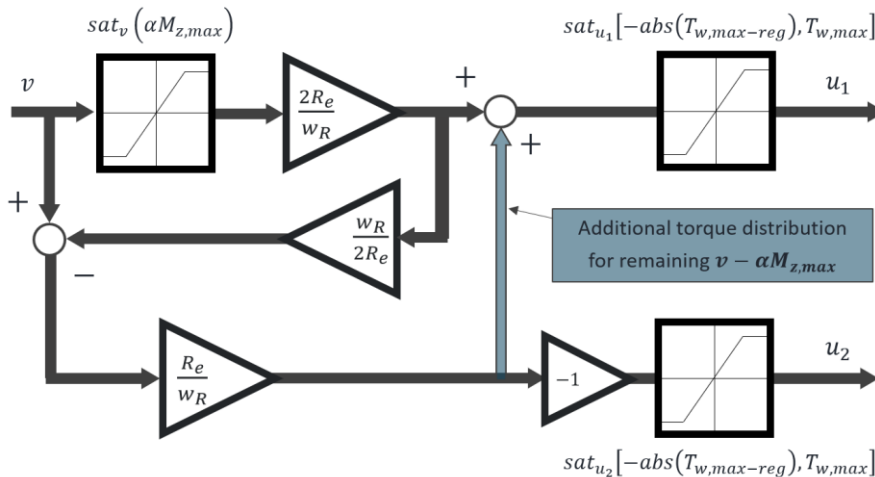
Figure 54. Modified control allocation algorithm structure
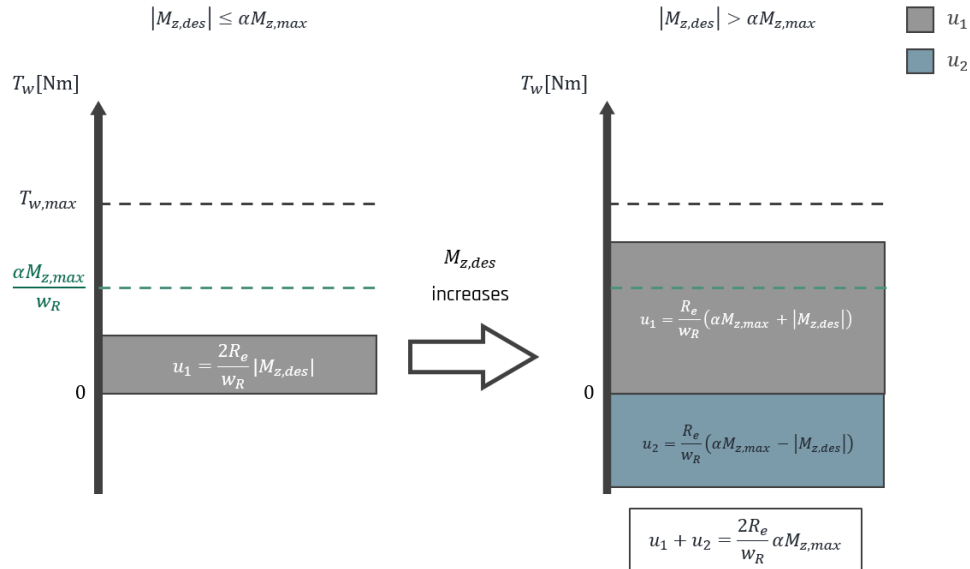
Figure 55. Torque distribution – modified structure

Figure 55 indicates that the intervention of the second input u_2 is determined by the tuning parameter α, which moves the threshold $\alpha M_{z,max}/w_R$. If it was not used, or set to 1, then the u_2 would intervene at the same time as in the conventional torque distribution.

To examine the behaviour of this method more closely, let's consider the situation when $M_{z,des} \geq 0$. If $M_{z,des} \leq \alpha M_{z,max}$, only the first input u_1 is allocated. Conversely, if $M_{z,des} > \alpha M_{z,max}$, torque corresponding to $\alpha M_{z,max}$ is allocated to u_1 in advance. Then, to generate the additional required yaw moment, $T_{w,des}$ corresponding to the remaining $v - \alpha M_{z,max}$ are divided into left and right wheels with the same magnitude and different sign. These statements are true for $(v, u_1, u_2) = \left(M_{z,des}, T_{w,des,RL}, T_{w,des,RR}\right)$. In the case that $M_{z,des} < 0$, (v, u_1, u_2) is equal to $\left(-M_{z,des}, T_{w,des,RR}, T_{w,des,RL}\right)$ and the same procedure as above is performed. Based on this, the torque distribution with the modified daisy-chaining allocation is derived in a similar way as the conventional approach:

$$T_{w,des,RL} = \begin{cases} \dfrac{R_e}{w_R}\left(\alpha M_{z,max} - M_{z,des}\right) & if\ M_{z,des} < -\alpha M_{z,max} \\\\ -\dfrac{2R_e}{w_R}M_{z,des} & if - \alpha M_{z,max} \le M_{z,des} < 0 \\\\ 0 & if\ 0 \le M_{z,des} \le \alpha M_{z,max} \\\\ \dfrac{R_e}{w_R}\left(\alpha M_{z,max} - M_{z,des}\right) & if\ \alpha M_{z,max} < M_{z,des} \end{cases},$$

$$\text{(72)}$$

$$T_{w,des,RR} = \begin{cases} \dfrac{R_e}{w_R}\left(\alpha M_{z,max} + M_{z,des}\right) & if\ M_{z,des} < -\alpha M_{z,max} \\\\ 0 & if - \alpha M_{z,max} \le M_{z,des} < 0 \\\\ \dfrac{2R_e}{w_R}M_{z,des} & if\ 0 \le M_{z,des} \le \alpha M_{z,max} \\\\ \dfrac{R_e}{w_R}\left(\alpha M_{z,max} + M_{z,des}\right) & if\ \alpha M_{z,max} < M_{z,des} \end{cases}.$$

Eq. (72) is also illustrated in Figure 56 to present the idea more closely. The top left represents the $0 \le M_{z,des} \le \alpha M_{z,max}$, while the top right represents $-\alpha M_{z,max} \le M_{z,des} < 0$. The bottom left represents $\alpha M_{z,max} < M_{z,des}$, while $M_{z,des} < -\alpha M_{z,max}$ is represented on the bottom right.
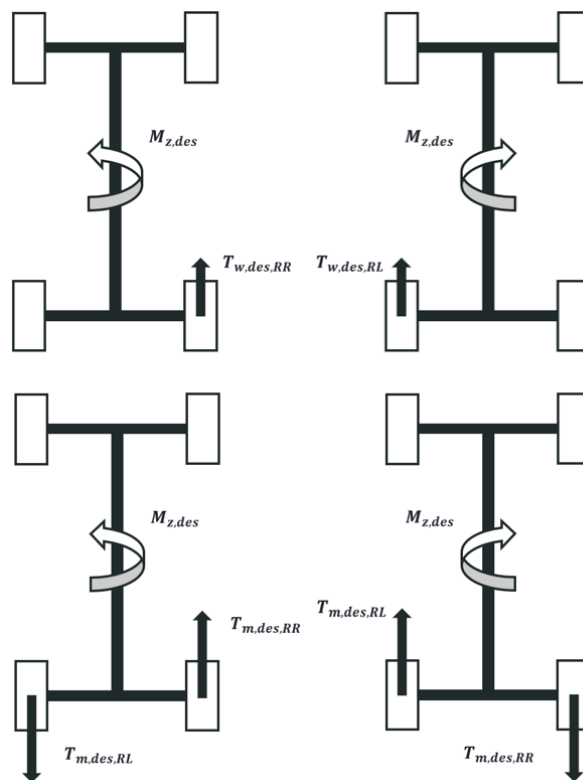
Figure 56. Illustrated torque distribution cases – modified structure

To summarise, the advantages of the modified daisy-chaining allocation method in comparison with the conventional one are as follows:

- By adding the tuning parameter α, it is possible to tune the timing of the negative motor torque distribution freely and thus choose between lower energy consumption and faster lap times

- The more significant the magnitude of the sum of torque inputs, the greater the intervention in the change of longitudinal vehicle velocity, regardless of the driver's pedal command.

As shown in Figure 53 and Figure 55, the magnitude of the sum of torque inputs in each daisy-chaining allocation is as follows [19]:

$$\underline{\text{Conventional}} \rightarrow |u_1 + u_2| = 2\left|T_{w,max,i} - \frac{2R_e}{w_R}|M_{z,des}|\right|, \tag{73}$$

$$\underline{\text{Modified}} \rightarrow |u_1 + u_2| = \frac{2R_e}{w_R}\alpha M_{z,max}. \tag{74}$$

In case of $\alpha \leq \left|\frac{w_R}{R_e}\frac{T_{w,max,i}}{M_{z,max}} - \frac{|M_{z,des}|}{M_{z,max}}\right|$, the modified sum of torques becomes smaller than the conventional sum. This is an advantage of the modified allocation, i.e., it is less involved in the longitudinal velocity command of the driver since the desired torques derived in Eq. (71) and (72) are required changes to the already present torque demands from the driver.

4.3.2. *Proposed control allocation*

Motivated by the simplicity and intuitiveness of the daisy-chain allocation and the advantages of the proposed modified structure given by [19], the following control allocation is proposed. The general idea stays the same, but some modifications are made, which make this allocation quasi-online (e.g. adaptive α).

Adaptive tuning parameter α

While the modified daisy-chain allocation structure in [19] used only one constant tuning parameter, the method proposed in this work uses four independent values, one for each wheel. These values are calculated online based on the current maximum yaw moment that the wheels can produce. To determine the α for each wheel, maximum yaw moments producible by positive and negative wheel torques must be calculated while considering contributions mentioned in Figure 50 and Figure 51. The positive and negative yaw moment potentials are calculated as follows:

$$M_{z,max-pos,FL} = \left(C_{\delta_{w,FL}}\frac{w_F}{2R_e} - \frac{l_F}{R_e}\right)T_{w,max,FL},$$

$$M_{z,max-pos,FR} = \left(C_{\delta_{w,FR}}\frac{w_F}{2R_e} + \frac{l_F}{R_e}\right)T_{w,max,FR},$$

$$M_{z,max-pos,RL} = \frac{w_R}{2R_e}T_{w,max,RL}, \qquad (75)$$

$$M_{z,max-pos,RR} = \frac{w_R}{2R_e}T_{w,max,RR},$$

$$M_{z,max-reg,FL} = \left|\left(-C_{\delta_{w,FL}}\frac{w_F}{2R_e} + \frac{l_F}{R_e}\right)T_{w,max-reg,FL}\right|,$$

$$M_{z,max-reg,FR} = \left|\left(-C_{\delta_{w,FR}}\frac{w_F}{2R_e} - \frac{l_F}{R_e}\right)T_{w,max-reg,FR}\right|,$$

$$M_{z,max-reg,RL} = \frac{w_R}{2R_e}\left|T_{w,max-reg,RL}\right|, \qquad (76)$$

$$M_{z,max-reg,RR} = \frac{w_R}{2R_e}\left|T_{w,max-reg,RR}\right|.$$

Once the yaw moment potentials are calculated, potential ratio factors are to be calculated in a daisy-chain manner by comparing the next control potential to the previous, except the last potential ratio factor, where the final control potential is divided by the sum of the second and final potential. This approach ensures that each tire is saturated to a certain degree, avoiding the oversaturation of a single tire, as would be the case if the conventional daisy-chain allocation structure was used. The potential ratio factors are determined as follows:

$$\lambda_{F-pos} = \begin{cases} \dfrac{M_{z,max-reg,RL}}{M_{z,max-pos,FR}} & if\ M_{z,des} \geq 0 \\[2mm] \dfrac{M_{z,max-reg,RR}}{M_{z,max-pos,FL}} & otherwise \end{cases},$$

$$\lambda_{R-pos} = \begin{cases} \dfrac{M_{z,max-pos,FR}}{M_{z,max-pos,RR}} & if\ M_{z,des} \geq 0 \\[2mm] \dfrac{M_{z,max-pos,FL}}{M_{z,max-pos,RL}} & otherwise \end{cases},$$

$$\lambda_{F-neg} = \begin{cases} \dfrac{M_{z,max-reg,FL}}{M_{z,max-reg,FL}+M_{z,max-pos,FR}} & if\ M_{z,des} \geq 0 \\[2mm] \dfrac{M_{z,max-reg,FR}}{M_{z,max-pos,FL}+M_{z,max-reg,FR}} & otherwise \end{cases}, \qquad (77)$$

$$\lambda_{R-neg} = \begin{cases} \dfrac{M_{z,max-reg,FL}}{M_{z,max-reg,RL}} & if\ M_{z,des} \geq 0 \\[2mm] \dfrac{M_{z,max-reg,FR}}{M_{z,max-reg,RR}} & otherwise \end{cases}.$$

These potential ratio factors adapt the tuning parameter α through a LUT. Rear wheels have their α chosen by looking at the front to rear potentials, while the front wheels' α are

selected with a different approach. The front wheel with a positive torque has an inverse approach to the rear wheels since it compares rear to front potential. In general, it's expected that the outer wheel will have more potential than the inner wheel, thus the reason for the inverse approach. On the other hand, the front wheel that has a negative torque chooses a minimum value. Based on these findings, the tuning parameter for each wheel is determined as follows:

$$
\alpha_{F-pos} = \begin{cases} \alpha_{F,const-pos} & if \ \lambda_{F-pos} \le 1 \\ \alpha_{F,LUT-pos} & otherwise \end{cases},
$$

$$
\alpha_{R-pos} = \begin{cases} \alpha_{R,const-pos} & if \ \lambda_{R-pos} > 1 \\ \alpha_{R,LUT-pos} & otherwise \end{cases},
$$

$$
\alpha_{F-neg} = \min\big(\alpha_{F,const-neg}, \alpha_{F,LUT-neg}\big),
$$

$$
\alpha_{R-neg} = \begin{cases} \alpha_{R,const-neg} & if \ \lambda_{R-neg} > 1 \\ \alpha_{R,LUT-neg} & otherwise \end{cases},
$$

$$(78)$$

where $\alpha_{F/R,const-pos/neg}$ is a constant value set by the user and resembles the tuning parameter behaviour presented in [19]. Value $\alpha_{F/R,LUT-pos/neg} = f\big(\lambda_{F/R-pos/neg}\big)$ is determined from a LUT. An example of a basic tuning parameter LUT for $\alpha_{R,LUT-pos}$ is shown in Figure 57, where the minimum value at $\lambda_{R-pos} = 1$ is equal to $\alpha_{R,const-pos} = 0.5$. The values of the LUT and a constant value are set with respect to the $\alpha \in [0,1]$.
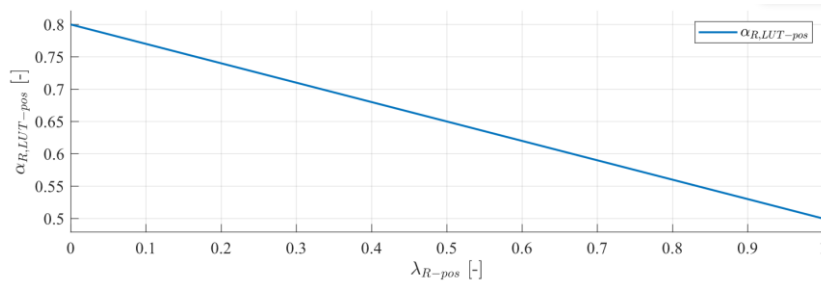
Figure 57. Tuning parameter lookup table example

In general, it's preferable to set the $\alpha_{F,const-pos/neg}$ to lower values because the yaw moment potentials can change rapidly, depending on the saturation on the tire, i.e. the rise/fall of lateral force produced by a change in wheel angle which influences the wheel slip angle and thus changes the maximum wheel torque.

Allocation stage definition

Before defining the values of distributed torques, each allocation stage must be specified. This section will cover stages for positive yaw demands defined by the yaw moment controller first, marked as the P stage, and the remaining stages for the negative demands (N stage) will be covered afterwards, although the same idea is applied. The stages are defined to ensure that

each tire is saturated to a certain degree before passing on to the next stage. Lower and upper thresholds for each stage are shown in Table 3, where $\alpha_{F/R,max-pos/neg}$ are the maximum values of each corresponding LUT. As can be seen in Table 3, there are three broad stages P1-P4, P5-P8 and P9. Stages P1-P4 are generally equal to a structure proposed in [19], while stages P5-P8 repeat the structure of the first four stages once again but with the tuning parameter value equal to $(\alpha_{F/R,max-pos/neg} - \alpha_{F/R-pos/neg})$. Stage P9 is covered later on. The same methodology is true for Table 4.

Table 3.   **Allocation stage thresholds – positive yaw demand**

Stage	Lower Threshold (L)	Upper Threshold (U)	
P1	$0 \leq$	$\leq \alpha_{R-pos}M_{z,max-pos,RR} = $ U P1	
P2	L P2 = U P1 $<$	$\leq$ U P1 $+ \alpha_{F-pos}M_{z,max-pos,FR} = $ U P2	
P3	L P3 = U P2 $<$	$\leq$ U P2 $+ \alpha_{R-neg}M_{z,max-reg,RL} = $ U P3	
P4	L P4 = U P3 $<$	$\leq$ U P3 $+ \alpha_{F-neg}M_{z,max-reg,FL} = $ U P4	(79)
P5	L P5 = U P4 $<$	$\leq$ U P4 $+ \left(\alpha_{R,max-pos} - \alpha_{R-pos}\right)M_{z,max-pos,RR} = $ U P5	
P6	L P6 = U P5 $<$	$\leq$ U P5 $+ \left(\alpha_{F,max-pos} - \alpha_{F-pos}\right)M_{z,max-pos,FR} = $ U P6	
P7	L P7 = U P6 $<$	$\leq$ U P6 $+ \left(\alpha_{R,max-neg} - \alpha_{R-neg}\right)M_{z,max-reg,RL} = $ U P7	
P8	L P8 = U P7 $<$	$\leq$ U P7 $+ \left(\alpha_{F,max-neg} - \alpha_{F-neg}\right)M_{z,max-reg,FL} = $ U P8	
P9	L P9 = U P8 $<$	$\leq M_{z,max} = $ U P9	

Table 4.   **Allocation stage thresholds – negative yaw demand**

Stage	Upper Threshold (U)	Lower Threshold (L)	
N1	$0 <$	L N1 $= -\alpha_{R-pos}M_{z,max-pos,RL} \leq$	
N2	$<$ L N1 = U N2	L N2 = L N1 $- \alpha_{F-pos}M_{z,max-pos,FL} \leq$	
N3	$<$ L N2 = U N3	L N3 = L N2 $- \alpha_{R-neg}M_{z,max-reg,RR} \leq$	
N4	$<$ L N3 = U N4	L N4 = L N3 $- \alpha_{F-neg}M_{z,max-reg,FR} \leq$	
N5	$<$ L N4 = U N5	L N5 = L N4 $- \left(\alpha_{R,max-pos} - \alpha_{R-pos}\right)M_{z,max-pos,RL} \leq$	(80)
N6	$<$ L N5 = U N6	L N6 = L N5 $- \left(\alpha_{F,max-pos} - \alpha_{F-pos}\right)M_{z,max-pos,FL} \leq$	
N7	$<$ L N6 = U N7	L N7 = L N6 $- \left(\alpha_{R,max-neg} - \alpha_{R-neg}\right)M_{z,max-reg,RR} \leq$	
N8	$<$ L N7 = U N8	L N8 = L N7 $- \left(\alpha_{F,max-neg} - \alpha_{F-neg}\right)M_{z,max-reg,FR} \leq$	
N9	$<$ L N8 = U N9	L N8 $= -M_{z,max} \leq$	

Torque distribution

With the thresholds defined, torque distribution is straightforward for both the positive and negative demands for the first eight stages. Wheel torque distribution for the ninth stage is determined by the potential wheel yaw moment distribution that is calculated as follows:

$$\lambda_{FL} = \begin{cases} \dfrac{M_{z,max-reg,FL}}{M_{z,max}} & if \ M_{z,des} \geq 0 \\ \dfrac{M_{z,max-pos,FL}}{M_{z,max}} & otherwise \end{cases},$$

$$\lambda_{FR} = \begin{cases} \dfrac{M_{z,max-pos,FR}}{M_{z,max}} & if \ M_{z,des} \geq 0 \\ \dfrac{M_{z,max-reg,FR}}{M_{z,max}} & otherwise \end{cases},$$

$$\lambda_{RL} = \begin{cases} \dfrac{M_{z,max-reg,RL}}{M_{z,max}} & if \ M_{z,des} \geq 0 \\ \dfrac{M_{z,max-pos,RL}}{M_{z,max}} & otherwise \end{cases}, \tag{81}$$

$$\lambda_{RR} = \begin{cases} \dfrac{M_{z,max-pos,RR}}{M_{z,max}} & if \ M_{z,des} \geq 0 \\ \dfrac{M_{z,max-reg,RR}}{M_{z,max}} & otherwise \end{cases}.$$

$$\sum_{\substack{i=F,R \\ j=L,R}} \lambda_{ij} = 1 \tag{82}$$

Finally, using the upper (U) and lower (L) thresholds given by Eq. (79) and (80) in Table 3 and Table 4, and potential wheel distribution given by Eq. (81), online torque distribution is defined as follows:

$$
T_{w,des,FL} = \begin{cases}
T_{w,des,FL-N8} + \lambda_{FL} M_{z,diff-N9}, & -M_{z,max} \le M_{z,des} < U\,N9 & \leftarrow N9 \\
T_{w,des,FL-N7}, & L\,N8 \le M_{z,des} < U\,N8 & \leftarrow N8 \\
T_{w,des,FL-N6}, & L\,N7 \le M_{z,des} < U\,N7 & \leftarrow N7 \\
T_{w,des,FL-N5} + \frac{2R_e}{w_F} M_{z,diff-N6}, & L\,N6 \le M_{z,des} < U\,N6 & \leftarrow N6 \\
T_{w,des,FL-N4}, & L\,N5 \le M_{z,des} < U\,N5 & \leftarrow N5 \\
T_{w,des,FL-N3}, & L\,N4 \le M_{z,des} < U\,N4 & \leftarrow N4 \\
T_{w,des,FL-N2}, & L\,N3 \le M_{z,des} < U\,N3 & \leftarrow N3 \\
\frac{2R_e}{w_F} M_{z,diff-N2}, & L\,N2 \le M_{z,des} < U\,N2 & \leftarrow N2 \\
0, & L\,N1 \le M_{z,des} < 0 & \leftarrow N1 \\
0, & 0 \le M_{z,des} \le U\,P1 & \leftarrow P1 \\
0, & L\,P2 < M_{z,des} \le U\,P2 & \leftarrow P2 \\
0, & L\,P3 < M_{z,des} \le U\,P3 & \leftarrow P3 \\
\frac{2R_e}{w_F} M_{z,diff-P4}, & L\,P4 < M_{z,des} \le U\,P4 & \leftarrow P4 \\
T_{w,des,FL-P4}, & L\,P5 < M_{z,des} \le U\,P5 & \leftarrow P5 \\
T_{w,des,FL-P5}, & L\,P6 < M_{z,des} \le U\,P6 & \leftarrow P6 \\
T_{w,des,FL-P6}, & L\,P7 < M_{z,des} \le U\,P7 & \leftarrow P7 \\
T_{w,des,FL-P7} + \frac{2R_e}{w_F} M_{z,diff-P8}, & L\,P8 < M_{z,des} \le U\,P8 & \leftarrow P8 \\
T_{w,des,FL-P8} + \lambda_{FL} M_{z,diff-P9}, & L\,P9 < M_{z,des} \le M_{z,max} & \leftarrow P9
\end{cases} \tag{83}
$$

$$
T_{w,des,FR} = \begin{cases}
T_{w,des,FR-N8} + \lambda_{FR} M_{z,diff-N9}, & -M_{z,max} \le M_{z,des} < U\,N9 & \leftarrow N9 \\
T_{w,des,FR-N7} + \frac{2R_e}{w_F} M_{z,diff-N8}, & L\,N8 \le M_{z,des} < U\,N8 & \leftarrow N8 \\
T_{w,des,FR-N6}, & L\,N7 \le M_{z,des} < U\,N7 & \leftarrow N7 \\
T_{w,des,FR-N5}, & L\,N6 \le M_{z,des} < U\,N6 & \leftarrow N6 \\
T_{w,des,FR-N4}, & L\,N5 \le M_{z,des} < U\,N5 & \leftarrow N5 \\
\frac{2R_e}{w_F} M_{z,diff-N4}, & L\,N4 \le M_{z,des} < U\,N4 & \leftarrow N4 \\
0, & L\,N3 \le M_{z,des} < U\,N3 & \leftarrow N3 \\
0, & L\,N2 \le M_{z,des} < U\,N2 & \leftarrow N2 \\
0, & L\,N1 \le M_{z,des} < 0 & \leftarrow N1 \\
0, & 0 \le M_{z,des} \le U\,P1 & \leftarrow P1 \\
\frac{2R_e}{w_F} M_{z,diff-P2}, & L\,P2 < M_{z,des} \le U\,P2 & \leftarrow P2 \\
T_{w,des,FR-P2}, & L\,P3 < M_{z,des} \le U\,P3 & \leftarrow P3 \\
T_{w,des,FR-P3}, & L\,P4 < M_{z,des} \le U\,P4 & \leftarrow P4 \\
T_{w,des,FR-P4}, & L\,P5 < M_{z,des} \le U\,P5 & \leftarrow P5 \\
T_{w,des,FR-P5} + \frac{2R_e}{w_F} M_{z,diff-P6}, & L\,P6 < M_{z,des} \le U\,P6 & \leftarrow P6 \\
T_{w,des,FR-P6}, & L\,P7 < M_{z,des} \le U\,P7 & \leftarrow P7 \\
T_{w,des,FR-P7}, & L\,P8 < M_{z,des} \le U\,P8 & \leftarrow P8 \\
T_{w,des,FR-P8} + \lambda_{FR} M_{z,diff-P9}, & L\,P9 < M_{z,des} \le M_{z,max} & \leftarrow P9
\end{cases} \tag{84}
$$

$$T_{w,des,RL} = \begin{cases} T_{w,des,RL-N8} + \lambda_{RL} M_{z,diff-N9}, & -M_{z,max} \le M_{z,des} < U\,N9 & \leftarrow N9 \\ T_{w,des,RL-N7}, & L\,N8 \le M_{z,des} < U\,N8 & \leftarrow N8 \\ T_{w,des,RL-N6}, & L\,N7 \le M_{z,des} < U\,N7 & \leftarrow N7 \\ T_{w,des,RL-N5}, & L\,N6 \le M_{z,des} < U\,N6 & \leftarrow N6 \\ T_{w,des,RL-N4} + \frac{2R_e}{w_R} M_{z,diff-N5}, & L\,N5 \le M_{z,des} < U\,N5 & \leftarrow N5 \\ T_{w,des,RL-N3}, & L\,N4 \le M_{z,des} < U\,N4 & \leftarrow N4 \\ T_{w,des,RL-N2}, & L\,N3 \le M_{z,des} < U\,N3 & \leftarrow N3 \\ T_{w,des,RL-N1}, & L\,N2 \le M_{z,des} < U\,N2 & \leftarrow N2 \\ \frac{2R_e}{w_R} M_{z,des}, & L\,N1 \le M_{z,des} < 0 & \leftarrow N1 \\ 0, & 0 \le M_{z,des} \le U\,P1 & \leftarrow P1 \\ 0, & L\,P2 < M_{z,des} \le U\,P2 & \leftarrow P2 \\ \frac{2R_e}{w_R} M_{z,diff-P3}, & L\,P3 < M_{z,des} \le U\,P3 & \leftarrow P3 \\ T_{w,des,RL-P3}, & L\,P4 < M_{z,des} \le U\,P4 & \leftarrow P4 \\ T_{w,des,RL-P4}, & L\,P5 < M_{z,des} \le U\,P5 & \leftarrow P5 \\ T_{w,des,RL-P5}, & L\,P6 < M_{z,des} \le U\,P6 & \leftarrow P6 \\ T_{w,des,RL-P6} + \frac{2R_e}{w_R} M_{z,diff-P7}, & L\,P7 < M_{z,des} \le U\,P7 & \leftarrow P7 \\ T_{w,des,RL-P7}, & L\,P8 < M_{z,des} \le U\,P8 & \leftarrow P8 \\ T_{w,des,RL-P8} + \lambda_{RL} M_{z,diff-P9}, & L\,P9 < M_{z,des} \le M_{z,max} & \leftarrow P9 \end{cases} \tag{85}$$

$$T_{w,des,RR} = \begin{cases} T_{w,des,RR-N8} + \lambda_{RR} M_{z,diff-N9}, & -M_{z,max} \le M_{z,des} < U\,N9 & \leftarrow N9 \\ T_{w,des,RR-N7}, & L\,N8 \le M_{z,des} < U\,N8 & \leftarrow N8 \\ T_{w,des,RR-N6} + \frac{2R_e}{w_R} M_{z,diff-N7}, & L\,N7 \le M_{z,des} < U\,N7 & \leftarrow N7 \\ T_{w,des,RR-N5}, & L\,N6 \le M_{z,des} < U\,N6 & \leftarrow N6 \\ T_{w,des,RR-N4}, & L\,N5 \le M_{z,des} < U\,N5 & \leftarrow N5 \\ T_{w,des,RR-N3}, & L\,N4 \le M_{z,des} < U\,N4 & \leftarrow N4 \\ \frac{2R_e}{w_R} M_{z,diff-N3}, & L\,N3 \le M_{z,des} < U\,N3 & \leftarrow N3 \\ 0, & L\,N2 \le M_{z,des} < U\,N2 & \leftarrow N2 \\ 0, & L\,N1 \le M_{z,des} < 0 & \leftarrow N1 \\ \frac{2R_e}{w_R} M_{z,des}, & 0 \le M_{z,des} \le U\,P1 & \leftarrow P1 \\ T_{w,des,RR-P1}, & L\,P2 < M_{z,des} \le U\,P2 & \leftarrow P2 \\ T_{w,des,RR-P2}, & L\,P3 < M_{z,des} \le U\,P3 & \leftarrow P3 \\ T_{w,des,RR-P3}, & L\,P4 < M_{z,des} \le U\,P4 & \leftarrow P4 \\ T_{w,des,RR-P4} + \frac{2R_e}{w_R} M_{z,diff-P5}, & L\,P5 < M_{z,des} \le U\,P5 & \leftarrow P4 \\ T_{w,des,RR-P5}, & L\,P6 < M_{z,des} \le U\,P6 & \leftarrow P6 \\ T_{w,des,RR-P6}, & L\,P7 < M_{z,des} \le U\,P7 & \leftarrow P7 \\ T_{w,des,RR-P7}, & L\,P8 < M_{z,des} \le U\,P8 & \leftarrow P8 \\ T_{w,des,RR-P8} + \lambda_{RR} M_{z,diff-P9}, & L\,P9 < M_{z,des} \le M_{z,max} & \leftarrow P9 \end{cases} \tag{86}$$

where $M_{z,diff}$ values are calculated as a difference of the current and previous stage upper limits for positive allocation stages (e.g. $M_{z,diff-P4} = U\,P4 - U\,P3 \ge 0$), and lower limit for negative allocation stages (e.g. $M_{z,diff-N4} = L\,P4 - L\,P3 \le 0$). Expressions (83) - (86) may seem a bit overwhelming at first but are intuitive when shown in graphical form, as in Figure 58 which

represents the torque distribution, for a 4WD configuration, following thresholds defined in Table 3 with equal yaw moment potentials, equal $\alpha_{F,const-pos/neg}$ and $\alpha_{R,const-pos/neg}$, and with equal $\alpha_{F,max-pos/neg}$ and $\alpha_{R,max-pos/neg}$.
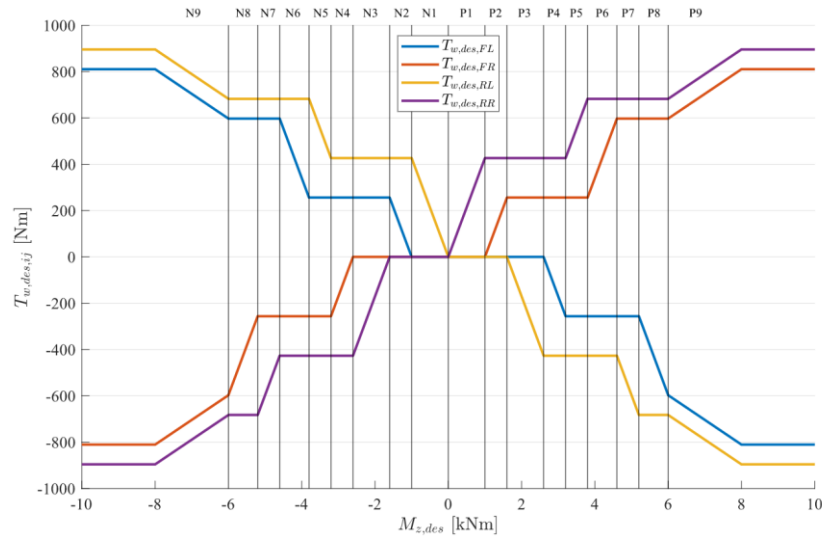
Figure 58. Wheel torque distribution example – equal yaw moments

Figure 58 also shows all allocation stages. Negative and positive stage nine is interesting because the torques are increased until they become saturated. This means the maximum yaw moment $M_{z,max}$ is reached. Another example is shown in Figure 59, where outer wheels have more yaw potential, which is more likely to happen. Stages P/N3,4 and P/N7,8 in the presented case are very short due to the lower yaw potentials. These stages could also be coupled into a single stage, making the allocation simpler, and is something left for future work.

Figure 59. Wheel torque distribution example – unequal yaw moments

5. TEST MANEUVERS AND SIMULATION RESULTS

To evaluate the performance of the proposed yaw rate control, several manoeuvres are carried out using VSM with the saturation-controlled driver model. Saturation-controlled driver compares his current position and heading with the track driving line. Additionally, his position and heading are analysed at the look-ahead points. Using this 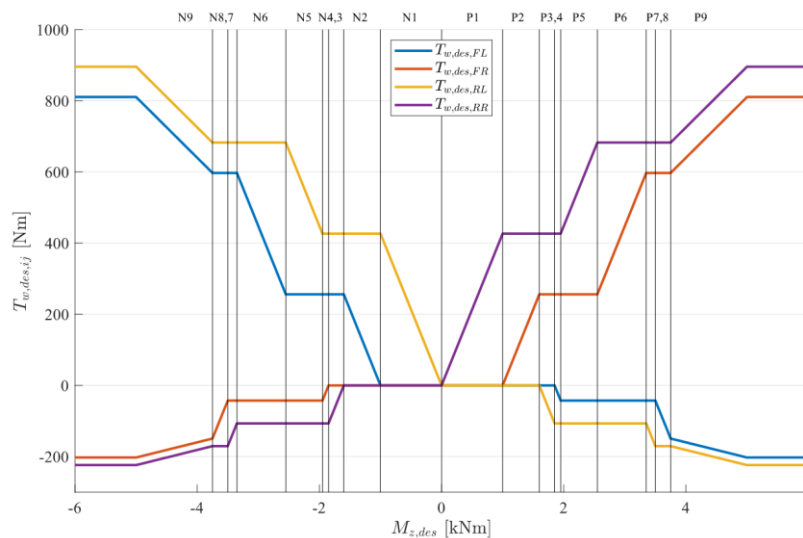analysis, steering, accelerator pedal, and brake actions are applied accordingly. Besides the target speed, the saturation-controlled driver uses tire saturation information from VSM to further modify the pedal and brake positions. Tire saturation denotes the ratio between the tire force potential and the actual tire force at a current timestep. This means that the tire potential is fully exploited if the tire saturation is equal to 1. The driver is tuned to exploit a baseline vehicle to the limit, i.e. to obtain the best performance on the test manoeuvre. Driver demand for each motor is set to be equal, and linearly dependent on the motor torque-speed map, meaning that 50% accelerator pedal demand would correspond to 50% torque demand from the motor. The proposed controller is modelled in MATLAB/Simulink® software package which is then used in a co-simulation environment with VSM. Signals from the VSM (Table 5) are passed through to the controller, where all other states required to obtain the controller outputs are calculate.

Table 5.   **Signals from VSM used in Simulink**

Symbol	Signal name
V	Vehicle speed
a_x	Longitudinal acceleration
a_y	Lateral acceleration
β	Vehicle sideslip angle
$\omega_{w,ij}$	Wheel angular speeds
$\omega_{m,ij}$	Motor angular speeds
ω_z	Yaw rate
δ	Steering wheel angle

Finally, the controller outputs being the desired torque distribution is passed back to the VSM environment. Also, because no slip control was implemented in the proposed control strategy, VSMs internal PI traction controller was tuned to avoid excessive wheel slip

situations. The same yaw rate controller and driver model parameters are used in all manoeuvres. The following results are shown for the baseline and controlled vehicle.

Friction utilisation on the front and rear axles, μ_F and μ_R will be one of the performance indicators that will be used. They were not directly defined by Figure 49 but arise from the friction circle defined previously. By rewriting the Eq. (56) that states $\mu F_z = \sqrt{F_x^2 + F_y^2}$, longitudinal and lateral friction utilisations for each tire, μ_x and μ_y, can be defined as:

$$\mu^2 = \left(\frac{F_x}{F_z}\right)^2 + \left(\frac{F_y}{F_z}\right)^2 = \mu_x^2 + \mu_y^2, \tag{87}$$

which are then used to calculate the front and rear axle friction utilisations as:

$$\mu_{xF} = \frac{\mu_{xFL} + \mu_{xFR}}{2},$$

$$\mu_{xR} = \frac{\mu_{xRL} + \mu_{xRR}}{2},$$

$$\mu_{yF} = \frac{\mu_{yFL} + \mu_{yFR}}{2}, \tag{88}$$

$$\mu_{yF} = \frac{\mu_{yrL} + \mu_{yrR}}{2},$$

$$\mu_F = \sqrt{\mu_{xF}^2 + \mu_{yF,}^2}$$

$$\mu_R = \sqrt{\mu_{xR}^2 + \mu_{yR}^2}. \tag{89}$$

5.1. Double-Lane Change (ISO 8331-1)

The first test manoeuvre is the double-lane change (DLC), which is considered the benchmark in the automotive field, because it is useful to evaluate fast transient responses, although the evaluations are subjective. The standard DLC must be with no accelerator pedal change during the manoeuvre. The test is considered successful when the vehicle completes the path within the area determined by delimitation cones. The manoeuvre track dimensions are standardised by [31].

The results for a test with an entry speed of 90 km/h are shown in Figure 60 and Figure 61. The first obvious thing to notice is the difference in vehicle speeds. While the controlled vehicle can maintain the reference speed of 90 km/h just by using yaw rate control, the baseline (BL) vehicle cannot. The yaw rate follows the reference more closely than the baseline vehicle, but the error is always present since no integral term is present in the controller. This error could

be reduced if a modified controller that includes an integral term was used, as proposed in subsection 3.2.1 (Figure 37). The controlled vehicle has also reduced the sideslip angle by a small margin. The steering wheel angle input is smoothed out. When the driver gap from the centreline is compared, there is not a lot of difference, up to the very end of the manoeuvre, meaning that the trajectory was almost the same, while being able to maintain the entry speed. Higher friction utilisation is present throughout the manoeuvre, especially lateral utilisation, which brings lateral acceleration. This increase is most noticeable between 160 and 190 m. This is a result of fully exploiting the available tire grip, as shown by the control yaw moment produced by the torque distribution. The control yaw moment reaches the maximum yaw moments the tires can handle. The graph showing the control yaw moment can also be used to notice a change in the sign of yaw rate error. The change of sign is represented by the step change of maximum yaw moment, because different yaw moment potentials are present on each tire. For example, a change in maximum yam moment can be noticed at 185 m, where the yaw moment demand changes from negative to positive due to a change in yaw rate error. The outer, right wheels have more vertical tire force due to lateral dynamic weight distribution. Because the positive control yaw moment is applied, the maximum yaw moment limit rises as the vertical tire force is transferred from the right to left wheels. Another thing to notice is that the front tires are utilised better on a controlled vehicle. A slight drop in rear utilisation is present, but the overall total utilisation stays at the same level. This drop is caused by the positive torque demands, which shift the utilisation from lateral to longitudinal.
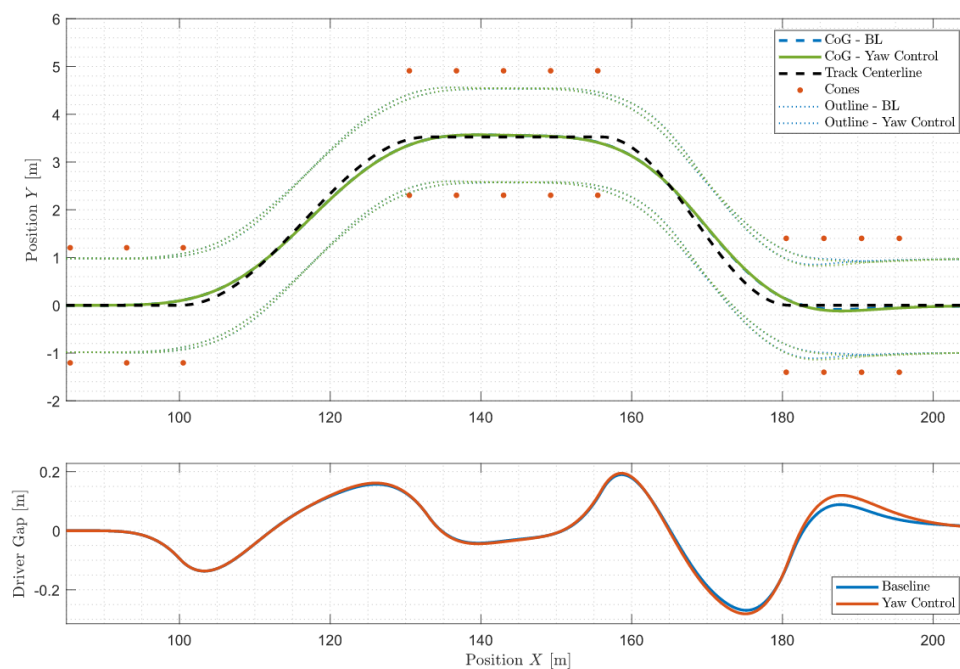

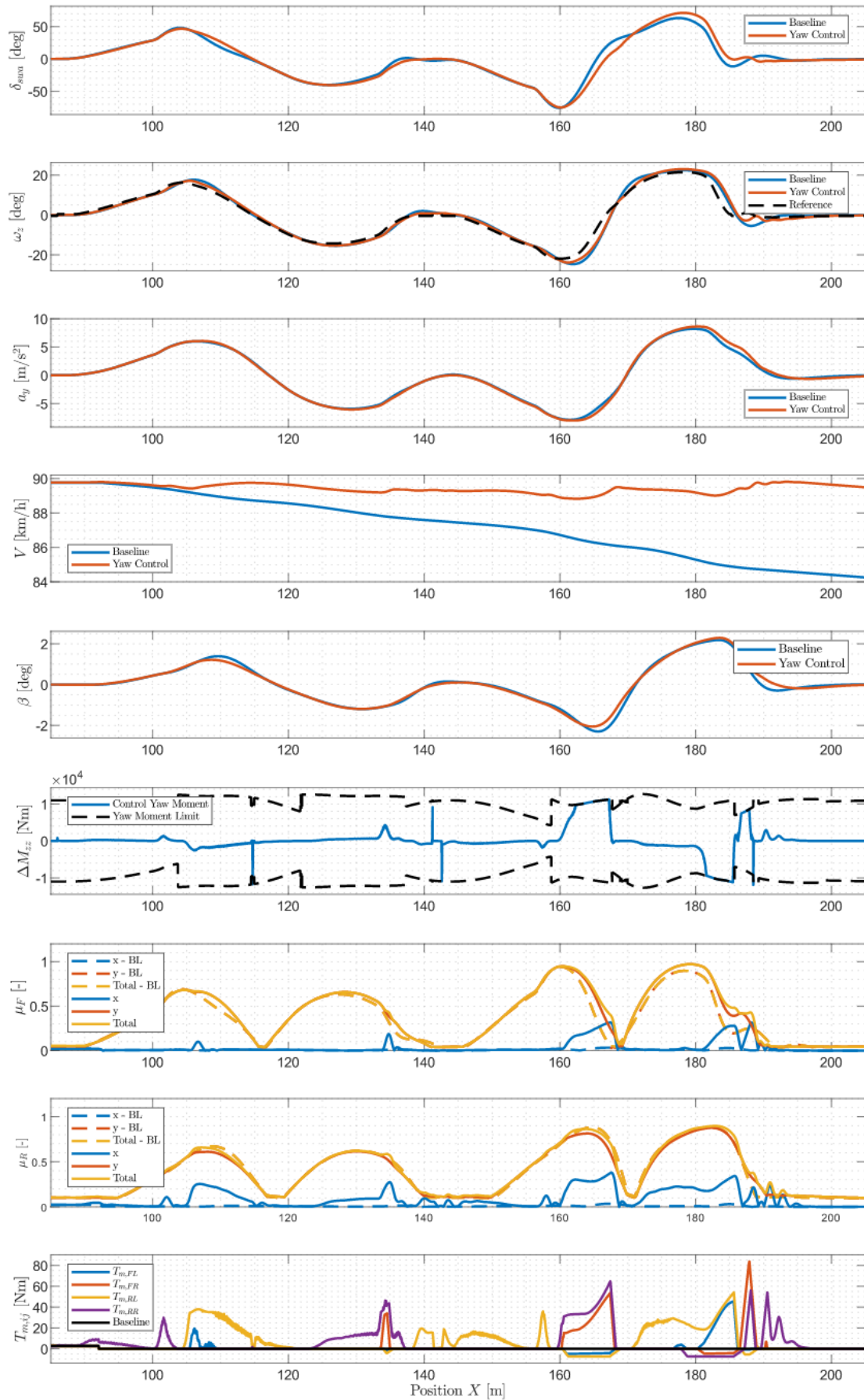**Figure 60. Double lane change – 90 km/h**

Figure 61. Double lane change – 90 km/h – states

Even though the baseline vehicle cannot finish the manoeuvre with an entry speed higher than 90 km/h, a controlled vehicle is evaluated at the vehicle speed of 100 km/h. The results are shown in Figure 62 and overlayed on top of the results for the 90 km/h baseline vehicle. The vehicle, once again, accomplishes to maintain its entry speed while still keeping the vehicle under control. A busier controller action can be noticed when compared to the case with an entry speed of 90 km/h, but nothing major. The most noticeable controller influence can be seen between 160 and 190 m, just like in the previous case, but this time the vehicle is at its peak control yaw moment for most of the time, meaning that no further increase in the performance can be extracted with the proposed control strategy. Even though the vehicle speed is higher, the vehicle sideslip angle stayed below the baseline vehicle, just like in the previous case, except between 180 and 190 m, where the vehicle enters the last section of the test manoeuvre and is already driving at its limits. Higher vehicle speed is accompanied by the total drop of rear lateral utilisation due to the needed increase in longitudinal utilisation needed to keep the vehicle speed at the same level. This drop is compensated on the front wheels, where an increase in lateral utilisation is more pronounced than in the last case.
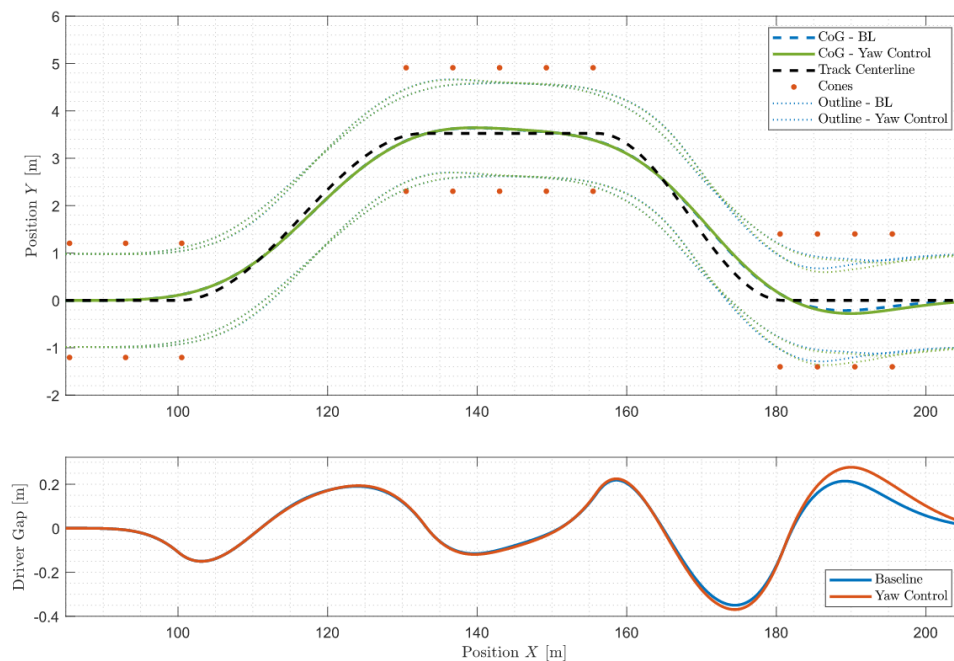
Figure 62. Double lane change – 100 km/h – performance increase
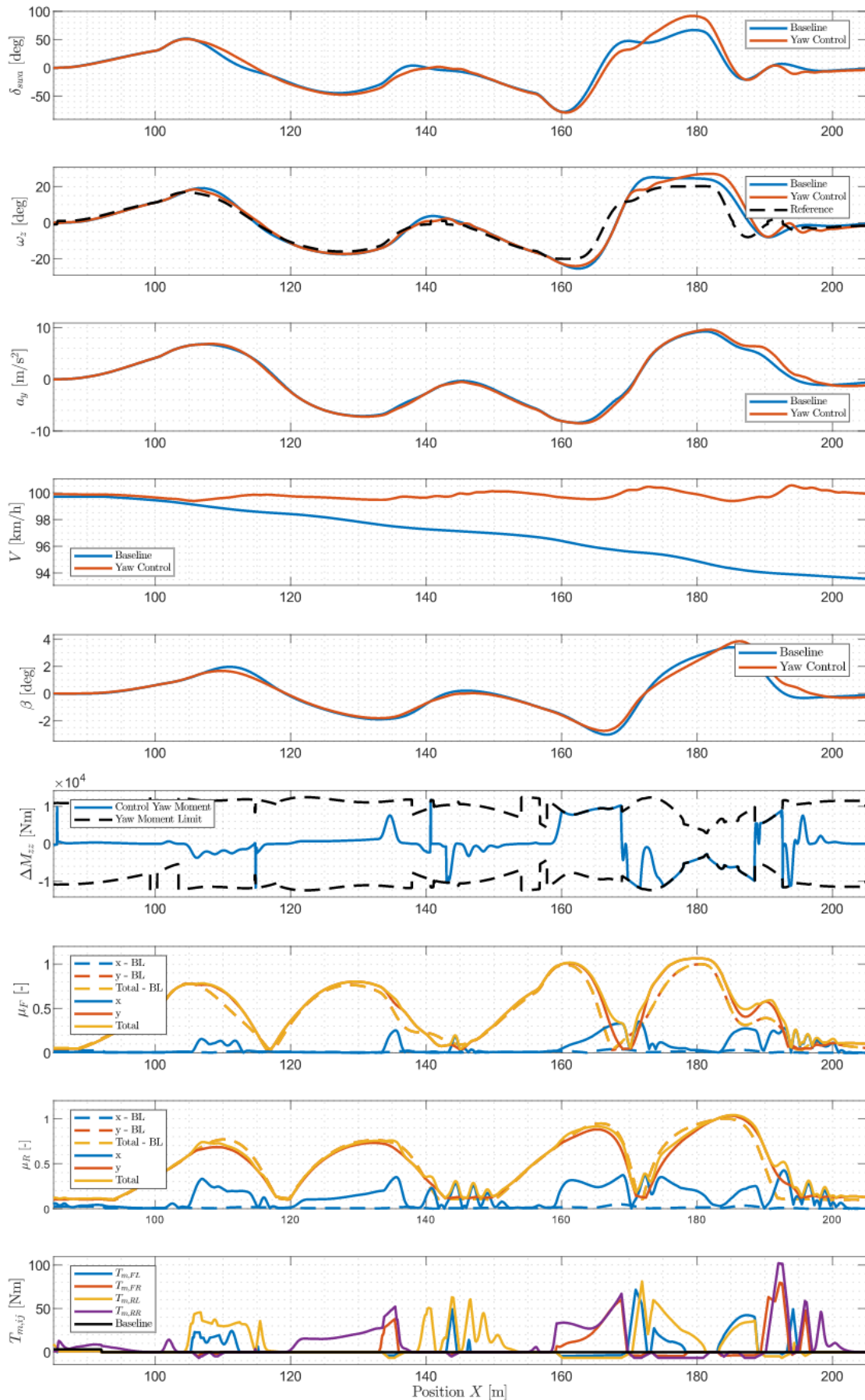
Figure 63. Double lane change – 100 km/h – performance increase – states

An example of a poorly tuned controller is also shown in Figure 64, where the performance from the vehicle states is almost the same across a board, but the difference is very noticeable in motor torques in the last graph, where a lot of "chattering" can be seen. This can damage the motors over time, and appropriate tuning can prevent it.

Figure 64. Double lane change – 90 km/h – an example of a poorly tuned controller

5.2. Obstacle-avoidance (ISO 8331-2)

The second test manoeuvre is the obstacle-avoidance, which is very similar to the DLC, but with different track dimensions ([32]) and with no pedal actuation during the test.

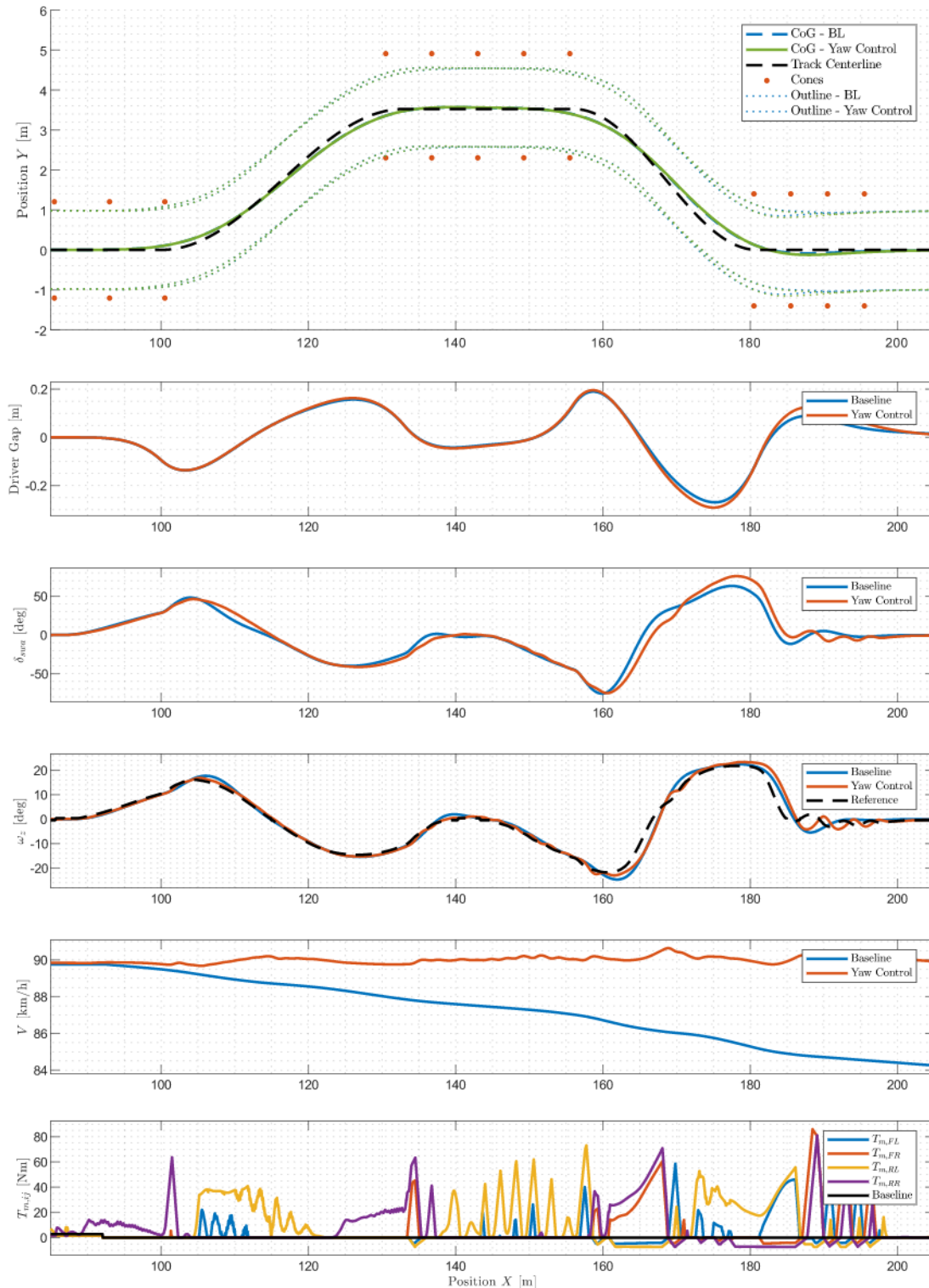The results for a test with an entry speed of 68 km/h are shown in Figure 65, where the grey symbolises the obstacle. Similar conclusions can be made as in the DLC manoeuvre. The vehicle speed is maintained at a higher level than on the baseline vehicle. Steering wheel angle inputs are smoother and retain a steadier value after the second turn-in, after 110 m into the test. The driver gap of a controlled vehicle is similar to the baseline, just like during the DLC test. Vehicle sideslip angle is close to constant during the second straight in the manoeuvre, which is more favourable because it makes the vehicle more predictable and easier to control. A bit of chatter is present in the motor torques, which could be solved to a certain degree with a better tune or an introduction of additional LUT for parameters, such as the yaw threshold λ_{err}. This chatter is also represented on the steering wheel, as can be seen at around 112, 128 and 135 m. It is also important to look at the maximum yaw moments, which are oscillating due to oscillations in the steering wheel angle input that can be noticed even on a baseline vehicle at around 118 m. The reason for these oscillations is that the baseline vehicle is already at its limits, on both the front and rear axle, and is just a calibration of a driver that tries to maintain the same trajectory. This could be solved to a certain degree with different driver parameters. Overall, friction utilisation is more stable, making the steering wheel angle, sideslip angle and lateral acceleration smoother and close to constant during the second section of the manoeuvre between 110 and 130 m.

Although the entrance speed improvement was noticed in DLC, the obstacle-avoidance test showed no improvement while evaluated at higher speeds (e.g. 70 km/h) and could not complete the test just like the baseline vehicle. This is due to already fully utilised friction potential.
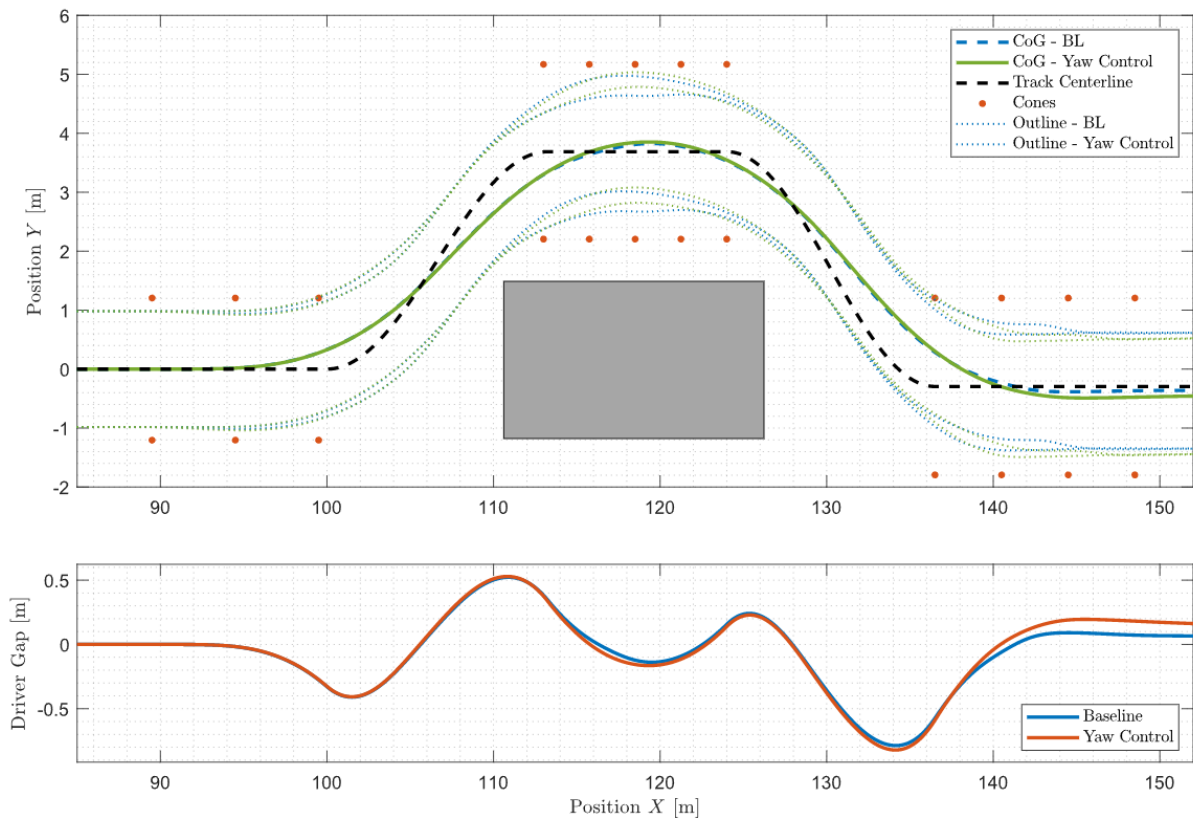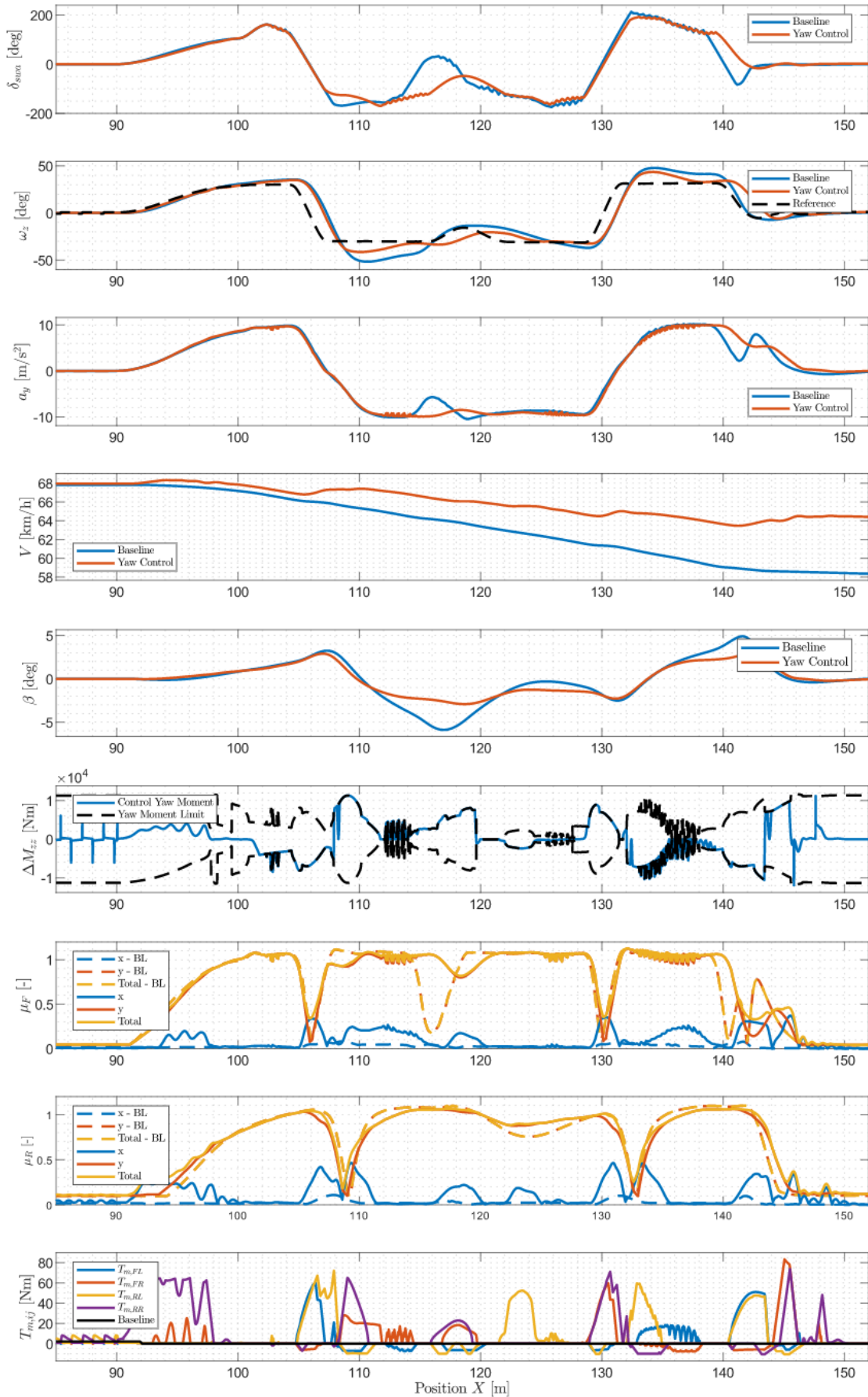
Figure 65. Obstacle-avoidance – 68 km/h

Figure 66. Obstacle-avoidance – 68 km/h

6. CONCLUSION

The goal of this thesis was to develop a yaw rate control system. Yaw reference generator, yaw moment controller and torque allocation have been proposed. The proposed method of generating yaw rate reference using AVL VSM™ to analyse the steady-state and transient behaviour of the vehicle showed a close resemblance to the current state-of-the-art yaw rate reference generator that uses piecewise expressions. PD^3 yaw moment controller is chosen as a promising and robust option whose main goal was responsiveness and not exact reference tracking. The proposed Daisy-chain torque allocation is worked out in detail to ensure equal distribution of tire saturation in order to avoid over-saturation of a single tire. The yaw rate control system is modelled in MathWorks MATLAB/Simulink$^®$ and run in co-simulation with AVL VSM™. Finally, the yaw rate control system is evaluated on several test manoeuvres. After the co-simulation environment has been set up, two typical test manoeuvres, double-lane change and obstacle-avoidance, have been defined in AVL VSM™ for dry road conditions. Mentioned manoeuvres have been simulated with the proposed yaw rate control system. Before the simulation, the friction utilisation factor was defined as an additional performance indicator. Simulation analysis was conducted on a four-wheel-drive drivetrain configuration for a baseline and yaw rate-controlled vehicle. Results have been examined. Vehicle speed was kept close to constant during the DLC test manoeuvre and had a higher value on obstacle-avoidance when compared to the baseline vehicle. The DLC manoeuvre could be performed even at 100 km/h, showing the performance increase of a controlled vehicle. The sideslip angle on both tests was reduced, and friction utilisation was increased. The yaw rate of the vehicle followed the reference more closely when compared to the baseline vehicle, making it more responsive.

To summarise, the yaw rate control system was implemented, and its performance was compared to the baseline vehicle. The controlled vehicle showed persistent improvements throughout the simulated scenarios, indicating the effectiveness of the proposed control system. The proposed improvements and further research are as follows:

- Implementation of control system tuning parameter lookup tables to improve robustness in different driving scenarios.
- Investigation of friction influence on yaw rate reference generation approach.
- Investigation of extension of the linear region of understeer characteristic and arbitrary understeering gradient modification, based on the proposed yaw rate generation approach.

- Investigation and implementation of time-optimal yaw rate reference.

- Addition of integral term to the yaw moment controller

- Replacing the MF tire model with different online estimation approaches

LITERATURE

[1]   Wong JY. Theory of ground vehicles. 3rd ed. John Wiley & Sons; 2001

[2]   Guiggiani M. The Science of Vehicle Dynamics: Handling, Braking, and Ride of Road and Race Cars. 3rd ed. Springer; 2022

[3]   Pinto L, Aldworth S, Watkinson M, Jeary P, Franco-Jorge M. Advanced Yaw Motion Control of a Hybrid Vehicle using Twin Rear Electric Motors. Advanced Vehicle Control. Loughborough, AVEC; 2010, p. 640-645.

[4]   Kaiser G, Liu Q, Hoffman C, Korte M, Werner H. Torque vectoring for an electric vehicle using an LPV drive controller and a torque and slip limiter. IEEE Conference on Decision and Control. 2012; p. 5016-5021. DOI: 0.1109/CDC.2012.6426553.

[5]   De Novellis L et al. Direct yaw moment control actuated through electric drivetrains and friction brakes: Theoretical design and experimental assessment. Mechatronics. 2015; 26: 1–15. New York: Elsevier.

[6]   De Novellis L, Sorniotti A, Gruber P. Driver modes for designing the cornering response of fully electric vehicles with multiple motors. Mech. Syst. Signal Processing; 2015; 64:1

[7]   Mangia A, Lenzo B, Sabbioni E. An integrated torque-vectoring control framework for electric vehicles featuring multiple handling and energy-efficiency modes selectable by the driver. Meccanica. 2021; 56:991-1010. DOI: 10.1007/s11012-021-01317-3.

[8]   Smith E, Velenis E, Cao D, Tavernini D. Evaluation of Optimal Yaw Rate Reference for Electric Vehicle Torque Vectoring. Proceedings of the 13th International Symposium on Advanced Vehicle Control (AVEC'16). London: CRC Press; 2016

[9]   Rajamani R. Vehicle Dynamics and Control. 2nd ed. Springer; 2012

[10]   Smith E, Tavernini D, Claret C, Velenis E, Cao D. Optimal yaw-rate target for electric vehicle torque vectoring system. IAVSD. Graz: CRC Press; 2016., p. 107. DOI: 10.1201/b21185-13.

[11]   de Castro R, Tanelli M, Arajo RE, Savaresi SM. Minimum-time manoeuvring in electric vehicles with four wheel-individual-motors. Vehicle System Dynamics. 2014; 52:824-846. London: Taylor & Francis.

[12]   Gabiccini M, Bartali L, Guiggiani M. Analysis of driving styles of a GP2 car via minimum lap-time direct trajectory optimization. Multibody System Dynamics. 2021; 53:85–113. DOI: 10.1007/s11044-021-09789-7.

[13]   Pacejka HB. Tire and Vehicle Dynamics. 3rd ed. Butterworth-Heinemann; 2012.

[14] Andersson JAE, Gillis J, Horn G, Rawlings JB, Diehl M. CasADI: a software framework for nonlinear optimization and optimal control. Mathematical Programming Computation. 2019; 11:1-36

[15] Patterson MA, Rao AV. GPOPS-II: A MATLAB Software for Solving Multiple-Phase Optimal Control Problems Using hp-Adaptive Gaussian Quadrature Collocation Methods and Sparse Nonlinear Programming. ACM Transactions on Mathematical Software. 2014 October; 41(1):1-37

[16] Wächter A, Biegler LT. On the Implementation of a Primal-Dual Interior Point Filter Line Search Algorithm for Large-Scale Nonlinear Programming. Mathematical Programming. 2006; 106(1):25-57

[17] Johnson MA, Moradi MH, editors. PID Control: New Identification and Design Methods. London: Springer; 2006

[18] Slotine JJ, Weiping L. Applied Nonlinear Control. Pearson; 1991.

[19] Park G, Han K, Nam K, Kim H, Choi SB. Torque Vectoring Algorithm of Electronic-Four-Wheel Drive Vehicles for Enhancement of Cornering Performance. IEEE Transactions on Vehicular Technology. 2020 April; 69(4):3668-3679. DOI: 10.1109/TVT.2020.2978099.

[20] Medina A. Comparison of a fast-nonlinear model predictive vs an error-cubic proportional derivative torque vectoring controller by a hexapod driving simulator. Mendeley Data. 2022; V1. DOI: 10.17632/td8tgrrh6b.1.

[21] Medina A, Bistué G, Rubio A, Prada J. A Direct Yaw-Moment Control Logic for an Electric 2WD Formula SAE Using an Error-Cube Proportional Derivative Controller. SAE International Journal of Connected and Automated Vehicles; 2020; 3(2):139-148. DOI: 10.4271/12-03-02-0012.

[22] Fadali MS, Visioli A. Optimal Control. In: Digital Control Engineering. Amsterdam: Elsevier BV; 2013, p. 399-438.

[23] Jäger B, Neugebauer P, Kriesten R, Parspour N, Gutenkunst C. Torque-vectoring stability control of a four wheel drive electric vehicle. Proceedings of the 2015 IEEE Intelligent Vehicles Symposium (IV). 2015, p. 1018-1023. DOI: 10.1109/IVS.2015.7225818.

[24] Medina A, Bistue G, Rubio A. Comparison of Typical Controllers for Direct Yaw Moment Control Applied on an Electric Race Car. Vehicles. 2021 February; 3(1):127-144. DOI: 10.3390/vehicles3010008.

[25] Ghosh J, Tonoli A, Amati N. Improvement of Lap-Time of a Rear Wheel Drive Electric Racing Vehicle by a Novel Motor Torque Control Strategy. SAE Technical Paper. 2017. DOI: 10.4271/2017-01-0509.

[26] De Novellis L, Sorniotti A, Gruber P, Pennycott A. Comparison of Feedback Control Techniques for Torque-Vectoring Control of Fully Electric Vehicles. IEEE Transactions on Vehicular Technology. 2014 October; 63(8):3612-3623. DOI: 10.1109/TVT.2014.2305475.

[27] Janssen LJ, Emmelmann HJ. Aerodynamic Improvements - A Great Potential for Better Fuel Economy. SAE Transactions. 1978; 87:1261-1269

[28] Buffington JM, Enns DF. Lyapunov Stability Analysis of Daisy Chain Control Allocation. Journal of Guidance, Control and Dynamics; 1996; 19(6):1226-1230. DOI: 10.2514/3.21776.

[29] Han K, Park G, Sankar S, Nam K, Choi SB. Model Predictive Control Framework for Improving Vehicle Cornering Performance Using Handling Characteristics. IEEE Transactions on Intelligent Transportation Systems; 2021 May; 22(5):3014-3024. DOI: 10.1109/TITS.2020.2978948.

[30] Wang B, Lin C, Liang S, Gong X, Tao Z. Hierarchical Model Predictive Control for Autonomous Collision Avoidance of Distributed Electric Drive Vehicle with Lateral Stability Analysis in Extreme Scenarios. World Electric Vehicle Journal. 2021, 12(4):192. DOI: 10.3390/wevj12040192.

[31] ISO 3888-1:2018 Passenger cars – Test track for a severe lane-change manoeuvre – Part 1: Double Lane Change

[32] ISO 3888-2:2011 Passenger cars – Test track for a severe lane-change manoeuvre – Part 2: Obstacle avoidance